STUDY OF THE PROPERTIES OF TURBULENT FLOW THROUGH A VENTURI USING LDA TECHNIQUES

Linda Deutz

Delft University of Technology
Faculty of Applied Sciences
Department of Multi Scale Physics

Delft, December 2003

Kramers Laboratorium voor Fysische Technologie
Prins Bernhardlaan 6
2628 BW Delft

Advisors: prof. dr. R.F. Mudde
dr. H.R.E. van Maanen

Abstract

Venturi flow meters are originally applied in single phase flows. Currently, Shell investigates their application in so-called 'wet gas' production measurement. Wet gas consists of a mixture of gas, condensate (light oil) and water. The liquids have been condensed from the gas, due to the pressure and temperature drop while producing. The flow rate of such a three phase mixture is not easy to measure, though necessary for e.g. allocation of the fuel and reservoir management. The determination of the gas and liquid flow rates requires understanding of the multi phase flow in a venturi, including the phenomena downstream of the throat of a venturi in order to apply such a device in wet gas metering.

The project is a continuation of the work of Nievaart [Nievaart, 2000], who has been investigating the applied measurement technique, Laser Doppler Anemometry (LDA). This research is focussed on the effects of a venturi in turbulent flow. Therefore, measurements have been performed at eight locations, distributed upstream, in and downstream of a venturi in a single phase flow, in order to obtain more information about the velocity and turbulence intensity profiles, as well as the production and dissipation of turbulent kinetic energy.

Performing LDA measurements is not that easy. First, all parameters of the LDA set-up have to be adjust carefully and the laser beams have to be aligned very accurate, as the measuring volume has to be positioned very precisely. In order to reduce the effects of the wall, these have been replaced by thin foils in the throat and diffuser of the venturi. This has led to several adjustments to the set-up. At the other measuring locations, glass 'screws' have been applied. Furthermore, the LDA data had to be corrected for velocity bias. The time between data correction method proved to be the best out of five different methods for the performed measurements. All data sets have been tested using diagnostic techniques in order to verify their validity.

The sudden contraction of the venturi influences all flow properties in and downstream of this device. It creates a 'plug'flow in the throat with a flat axial velocity profile and a turbulence intensity of almost zero, except very close to the wall. In the throat, the flow is no longer in equilibrium according to the local power spectra. Here, dissipation dominates the flow. This 'plug'flow manifests itself as a jet-like flow in the divergent section of the venturi, leading to a strong increase in the production of turbulent kinetic energy near the wall. The significant change in turbulent flow properties is persistent, as 5 diameters downstream of the venturi the turbulence intensity is three times the value of that in turbulent pipe flow. Only, production has shifted towards the centerline and the flow is in equilibrium all along the traverse. Dissipation occurs mainly close to the wall. This downstream behavior is in contrast with turbulent pipe flow, where dissipation occurs in the core region, the only region where the flow is in equilibrium.

Acknowledgements

Fortunately, performing measurements and writing a thesis is not something you have to do completely on your own. Much support has been given by several persons, who I would like to thank in particular.

First, Rob Mudde and Hans van Maanen, thanks for your supervision, critical opinions, knowledge and pleasant co-operation! Jaap Beekman, your practical knowledge about LDA and your technical assistance helped me a lot while performing and analyzing the measurements.

Much gratitude goes to the support staff: besides the fun we had, you were of great value. I'll promise that the sheet will not release due to *my* experiments anymore! And than... all the inhabitants and visitors of the student room for the sensible and not so sensible discussions we had. Besides this, thanks for borrowing your 'hond', Social Pages buddy Remy! Marian, your cleaning skills are wonderful, as you have proven with your help during the floods in the 'labhal', due to my experiments. 'Een schonere labhal begint bij jezelf', isn't it...?

Finally, I would like to thank my parents, for they always supported me and let me free to do what I wanted to do.

List of symbols

Roman Symbols

Symbol	Description	S.I. units
A	noise contribution in ACF	$-$
B	turbulent fluctuations contribution in ACF	$-$
c	speed of light	m/s
D	pipe diameter	m
$D_{e^{-2}}$	waist diameter of laser beams before lens	m
$D_{k-\epsilon}$	turbulent viscous dissipation	m^2/s^3
D_u	deformation term of the mean flow	m^2/s^3
$d_{e^{-2}}$	waist diameter of focused laser beams	m
d_f	fringe distance	m
d_{lens}	distance between laser beams at lens	m
d_m	width scattering volume	m
E	kinetic energy of the mean flow	m^2/s^2
E_i	relative deviation from arithmetical mean velocity	$-$
$E(k)$	one-dimensional energy spectrum	m^3/s^2
e	turbulent kinetic energy	m^2/s^2
e'	instantaneous turbulent kinetic energy	m^2/s^2
e_{fr}	heat production per unit mass	m^2/s^2
F	focal length	m
f_{burst}	frequency of the burst	s^{-1}
f_d	resulting frequency difference	s^{-1}
f_{shift}	shift frequency	s^{-1}
f_{source}	emitted frequency of a source	s^{-1}
g_i	gravitational acceleration	m/s^2
K	flatness factor	$-$
k	wavenumber	m^{-1}
k^*	cutoff wavenumber	m^{-1}
L	characteristic length	m
$L_{entrance}$	entrance length	m
L_m	macro length scale	m
L_λ	Taylor length scale	m
l_m	length scattering volume	m
m_{corr}	displacement factor	$-$
N_{burst}	number of cycles in a Doppler burst	$-$
N_{fr}	number of fringes in scattering volume	$-$

N_{min}	minimal number of fringes	–
N_p	number of products in each slot (on average)	–
N_t	total number of velocity observations in the data	–
n	index of Power Law	–
n_a	refractive index of air	–
n_w	refractive index of water	–
P	probability	–
P_k	turbulent production	m^2/s^3
$P_{poisson}$	exponential probability distribution	–
P_u	production term of mean flow	m^2/s^3
p	pressure	kg/ms^2
p'	pressure, RMS value	kg/ms^2
R	radius	m
R_τ	auto covariance function	m^2/s^2
Re	Reynolds number	–
Re_{Φ_V}	Reynolds number, determined from the traverse measurements	–
r	distance from the centerline	m
S	skewness factor	–
$S(\omega)$	power spectrum	m^2/s
T	integration time	s
T_k	turbulent convection	m^2/s^3
T_m	macro time scale	s
T_{TBD}	time between data	s
$T_{TBD,A}$	average value of time between data	s
T_{tt}	transit time	s
T_u	transport term mean flow	m^2/s^3
T_{wave}	cycle time of a wave	s
T_λ	Taylor time scale	s
Δt	slot width	s
t_0	characteristic time of distribution	s
U	characteristic velocity	m/s
$\overline{U}$	average velocity of pipe flow	m/s
$< U >$	ensemble average velocity	m/s
U_m	macro velocity scale	m/s
U_{max}	maximum velocity (centerline)	m/s
U_λ	Taylor velocity scale	m/s
U_{Φ_V}	characteristic velocity, determined from the traverse measurements	m/s
u	local velocity	m/s
$\overline{u}$	local mean velocity	m/s
u'	turbulent velocity fluctuation	m/s
u^*	friction velocity	m/s
u_+	dimensionless wall velocity	–
u_i	velocity component	m/s
u, v, w	velocities along Cartesian (x, y, z) or cylindrical (x, r, ϕ) coordinates	m/s
$\overline{u}_c$	corrected local mean velocity	m/s
$\overline{u}_{ub}$	theoretical local unbiased mean velocity	m/s
w_i	weighting factor velocity bias correction method	–
y	distance from the wall	m
y_+	dimensionless coordinate from the wall	–

Greek Symbols

Symbol	Description	S.I. units
Γ	integral time scale	s
ϵ	energy dissipation	m^2/s^3
η_k	length scale of microstructure	m
θ	angle between laser beams	$-$
κ	Von Karman constant	$-$
λ	wavelength of laser beam	m
$\Delta\lambda$	change in observed wavelength	m
λ_{fr}	friction factor	$-$
μ	dynamic viscosity	kg/ms
ν	kinematic viscosity	m^2/s
Π_k	turbulent pressure transport	m^2/s^3
ρ	density of fluid	kg/m^3
$\rho(\tau)$	auto correlation function	$-$
σ_t	contribution of turbulent velocity fluctuations in ACF ($\tau = 0$)	$-$
σ_u^2	variance of the turbulent velocity	m^2/s^2
τ	time shift	s
τ_k	time scale of microstructure	s
τ_s	shear stress	kg/ms^2
τ_w	shear stress at the wall	kg/ms^2
υ_k	velocity scale of microstructure	m/s
Φ_V	flow rate, determined from the traverse measurements	m^3/s
χ	flow reversal parameter	$-$
χ_w	flow reversal parameter at the wall	$-$
ω	angular frequency	s^{-1}
$\Delta\omega$	size of wave package	s^{-1}

Abbreviations

Abbreviation	Description
ACF	Auto Correlation Function
CFD	Computational Fluid Dynamics
FFT	Fast Fourier Transform
HWA	Hot Wire Anemometry
IFA	Intelligent Flow Analyzer
LDA	Laser Doppler Anemometry
MS	Mean Square
PDF	Probability Density Function
PIV	Particle Image Velocity
RMS	Root Mean Square
SNR	Signal-to-Noise Ratio
TBD	Time Between Data

Contents

Abstract i

Acknowledgements iii

List of symbols v

Contents ix

Table of Contents ix

1 Introduction 1

1.1 Scope of the project 1

1.2 Objectives 2

1.3 Structure of the thesis 3

2 Turbulence 5

2.1 Turbulence - the basics 5

2.2 Statistics 7

2.3 Wall units 8

2.4 Scales 10

2.5 Turbulent kinetic energy 13

2.6 Correlation functions 15

3 Flow properties 19

3.1 Pipe flow 19

3.2 Venturi design 21
3.3 Contractions 23
3.4 Diffusers 23
3.4.1 Velocity profile 25
3.4.2 Turbulence intensity 27
3.4.3 Turbulent energy 27
3.4.4 Flow reversal 30
3.4.5 Downstream of the diffuser 30
3.5 Venturi flow 32

4 LDA **39**

4.1 Doppler effect 39
4.2 Configurations 40
4.3 Fringe model 41
4.4 Directional discrimination 43
4.5 Scattering volume 44
4.6 Tracer particles 45
4.7 Random sampling 46

5 Set-up of the flow loop and LDA system **47**

5.1 Flow loop 47
5.1.1 Venturi 47
5.1.2 Measurement section 50
5.1.3 Total flow loop 51
5.1.4 Regulation of the pump and water level 52
5.2 LDA set-up 52

6 Signal processing **55**

6.1 Diagnostic tools 55

6.2 Velocity bias 59
6.3 Auto correlation function 62
6.3.1 Properties of the ACF 63
6.4 Power spectrum 64
6.4.1 Properties of the power spectrum 64

7 Results **67**

7.1 General information 67
7.2 Time-velocity diagrams 68
7.3 Probability density functions 68
7.4 Velocity profiles 69
7.4.1 Profiles in wall units 70
7.5 Turbulence intensities 74
7.6 Auto correlation function 77
7.7 Power spectrum 81

8 Conclusions **87**

8.1 Measurement techniques 87
8.2 Signal processing 87
8.3 Flow properties 88

9 Recommendations **91**

9.1 Measurement techniques 91
9.2 Signal processing 91
9.3 Flow properties 92

Bibliography **93**

A Measurement parameters **97**

B Diagnostic tools **99**

C Time-velocity diagrams 103

D Probability density functions 113

E Auto correlation functions 123

F Power spectra 129

Chapter 1

Introduction

1.1 Scope of the project

Worldwide, the use of natural gas is increasing, as this is regarded as a clean fuel. Still, large resources are available. However, the number of resources producing only (dry) gas is negligible. Practically all reservoirs produce gas, as well as condensate (liquid consisting of hydrocarbons) and water. These two products condensate once the temperature and pressure drop below a certain level during production. The flow rate of such a three phase mixture (wet gas) is more difficult to measure as for single phase flow. Measuring the flow rate is essential, for this will be used for allocation of the fuel to several producers and production and reservoir management.

Currently, the production rate of the resources in e.g. the North Sea, is measured via a test-separator. This measuring device can be seen as a big tank in which the phases are separated by gravity. After separation, the single phase flow (dry gas) can be measured by ordinary flow meters. Yet, these test-separators have some severe disadvantages. The major problems are the size, the limited range, time and the costs. In particular the latter are the most problematic. Especially offshore, the required platform space enhances the costs significantly. For these reasons, Shell is searching for the application of cheaper and smaller flow metering devices.

Furthermore, as a test separator is too costly to install for each well, several wells are connected to one separator, resulting in non-continuous measurements and long switching times between measurements of the production rates of different wells. On the basis of these tests, of which results are only 'valid' at the time of the measurement, the allocation is calculated. To compensate for the inaccuracy of the flow rate measurement, the benefit goes to the producers transporting smaller amounts through the trunkline. For example, the wells of several producers in the North Sea are connected to one big trunk line to transport the gas to the mainland, where it will be allocated. Since NAM (50% Shell, 50% Esso) is the biggest user of the trunkline, the motivation for more accurate flow meters becomes clear, as this will save money.

To monitor the flow rate continuously, the best solution is to install a flow metering device for each well. Measuring the wet gas flow rate without a test-separator reduces the costs and could improve the operation of the field, in which the condensate is formed already. In these situations, acting at the right time can save a lot of valuable condensate, which would otherwise be left in the reservoir. As the metering device should be cheap, small, robust, reliable and reasonably accurate, Shell investigates the application of pressure difference measuring devices like a venturi.

In a venturi, a constricted pipe, three sections can be distinguished: an inlet, a throat and an outlet, see figure 1.1.

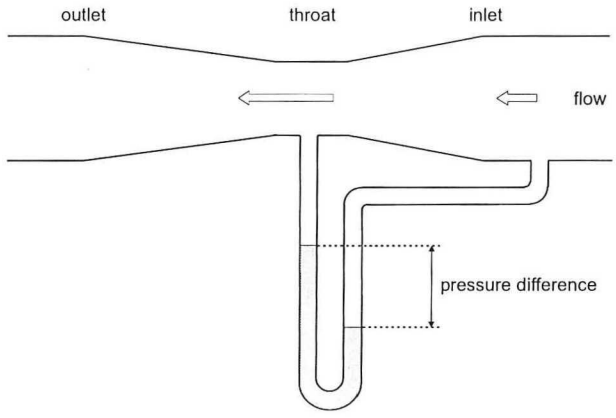

Figure 1.1: Schematic representation of a venturi and the measuring of the pressure difference between inlet and throat

From the inlet to the throat, the diameter slowly decreases. Between the throat and the outlet, the diameter gradually increases even more slowly towards the initial diameter. Owing to Bernoulli's law, as the velocity of the flow increases (in the throat due to a decrease in surface), the local pressure has to drop. A pressure difference between the inlet and the throat will be established, and this can be measured. A venturi is well shaped for measuring multi phase flows. Compared to e.g. a fringe orifice flow meter with the opening in the center, it is not possible that one of the phases is trapped in front of the fringe, causing unwanted pressure fluctuations and therefore erroneous flow metering results.

1.2 Objectives

All the advantages of the venturi convinced Shell to implement it in their wet gas fields in Egypt and Oman. An empirical model for estimating the flow rate, based on experiments, is used. Since this model lacks from any physical interpretation, a more thorough investigation is started. The goals of Shell are:
1. Improvement of a multi phase pressure related model with experimental data coming out of a venturi with a multi phase flow. This investigation delivers directly applicable knowledge.
2. A detailed study on a turbulent multi phase flow in a venturi, providing understanding of what is really happening there.
3. Obtaining more understanding about the total pressure loss across the venturi tube, as this is necessary to be able to calculate the gas and fluid flow rate.
This thesis is focussed on the second point and is a continuation of the work of Nievaart [Nievaart, 2000], who has studied the applied measurement technique (LDA) to perform measurements in a venturi thoroughly. To understand the behavior of a turbulent flow through a venturi, in this research work a 'simple' turbulent single phase flow has been studied. This flow is not that 'simple', as current CFD (Computational Fluid Dynamics) programs are not able to calculate the right maximum velocity or turbulence intensity in or downstream of the venturi [Tummers et al., 1997]. Furthermore, most experiments in venturi's are performed with less turbulent flows in venturi's with different shapes and often solely in the venturi. In order to obtain more insight in the development of a turbulent flow in and downstream of a venturi, several typical turbulent flow properties have been measured at eight locations in the flow. The results can be used to

validate computational simulations and to compare with two phase flow measurements, as this will probably be the next step in the main project. Well working CFD simulations will reduce the total number of experimental tests, and are interesting as this will save a lot of time and money.

1.3 Structure of the thesis

This thesis starts with a brief description of turbulence, followed by an overview of flow properties of turbulent pipe flow, flow through a contraction, diffuser and a tube with a constriction in chapter 3. Next, the applied measurement technique, Laser Doppler Anemometry (LDA), will be discussed, as with this technique it is possible to measure local time-velocity series close to the wall and in highly turbulent flows. In chapter 5 the experimental and LDA measurement set-up are explained. The next chapter deals with the signal processing, featuring the diagnostic tools, which warn in case there is something wrong with the data sets, although 'passed' data are not guaranteed 100% error free. It also discusses the velocity bias correction methods. In the chapter Results, flow properties as velocity and turbulence intensity profiles and turbulent kinetic energy production and dissipation will be covered. The results are from measurements upstream, in and downstream of the venturi, in order to form a perception of the development of a turbulent flow through such a device. Finally, this thesis will finish with the conclusions and recommendations for further investigations and experiments.

Chapter 2

Turbulence

One of the goals of the present investigation is to gain more knowledge about the turbulent behavior of a flow through and downstream of a venturi. Therefore, it's necessary to acquire more theoretical background about turbulence itself and the methods applied to measure turbulent flow properties.

In this chapter first some basics about turbulence and turbulent pipe flow will be discussed, followed by a more statistical approach of turbulence and the different (time) scales.

2.1 Turbulence - the basics

First of all, what *is* turbulence? Many books have been written about this subject and just as many descriptions have been given. First, we can say that turbulence is a property of the flow, not of the medium ([Nieuwstadt, 1998]). One of the most comprehensive 'definitions' on turbulence has been made by Bradshaw [Bradshaw, 1971], although it does not cover everything:
"Turbulence is a three-dimensional time-dependent motion in which vortex stretching causes velocity fluctuations to spread to all wavelengths between a minimum determined by viscous forces and a maximum determined by the boundary conditions of the flow. It is the usual state of fluid motion except at low Reynolds numbers".

From this definition, turbulence only occurs in a 3D environment in which vortex stretching is the source of a *disorganized* flow. As Nieuwstadt states: turbulence can be identified with "deterministic chaos". A turbulent flow is very sensitive to small distortions, which results in completely unpredictable solutions of differential equations which describe the flow. Bradshaw mentions the spreading of the velocity fluctuations to all wavelengths. A more detailed study about these different scales can be found in section 2.4.

In the last sentence of the definition, the Reynolds number is mentioned. This Reynolds number, Re, is a dimensionless number which is defined as the ratio of inertia and viscous forces and so is a measure for the relative importance of viscous effects [Janssen and Warmoeskerken, 1987]:

$$Re = \frac{\rho U L}{\mu} = \frac{U L}{\nu}, \tag{2.1}$$

in which U is the characteristic velocity, L the characteristic length scale and ν the kinematic viscosity of the flow, defined as the ratio of the dynamic viscosity μ and the density ρ. Generally speaking, a low Reynolds number corresponds to laminar flow, due to large viscous effects, and a high number to turbulent flow. In between there's a transition region with intermittent flow. Pipe flow e.g. is denominated turbulent for Re greater than 2300, but to make sure that the turbulence is fully developed, much higher Reynolds numbers are needed (like 100,000).

In a simple 1D-shear flow, the flow can be thought of as a set of 'slipping layers'. Each layer exerts a shear stress τ_s on the next layer. This drag force originates from the viscosity of the fluid. According to Newton's law of friction, which applies for specific types of fluids, the expression for the shear stress yields:

$$\tau_s = -\mu \frac{\partial u}{\partial y} \tag{2.2}$$

In this expression is μ the dynamic viscosity and y the coordinate normal to the flow direction, as defined in figure 2.1. u Is the local velocity in the flow direction.

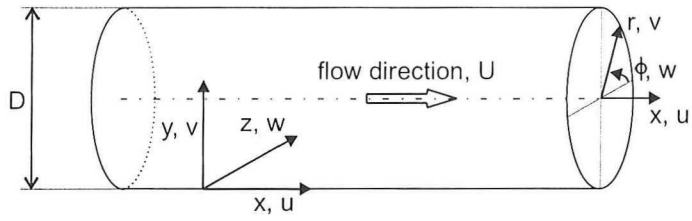

Figure 2.1: Definitions of Cartesian (left) and cylindrical coordinates (right), direction of mean flow velocity U and diameter D

The mathematical description of an incompressible, viscous Newtonian fluid is given by the Navier-Stokes equations. These differential equations result from the conservation of momentum [Nieuwstadt, 1998]. The three non-linear Navier-Stokes equations for an incompressible flow read:

$$\rho \left(\frac{\partial u_i}{\partial t} + u_j \frac{\partial u_i}{\partial x_j} \right) = \rho g_i - \frac{\partial p}{\partial x_i} + \mu \frac{\partial^2 u_i}{\partial x_j^2} \tag{2.3}$$

In which ρ is the density of the fluid, u_i are the three velocity components of the fluid, g_i are the components of the gravity acceleration vector and p the pressure.

The conservation of mass for an incompressible flow leads to the continuity equation:

$$\frac{\partial u_i}{\partial x_i} = 0 \tag{2.4}$$

With the condition of incompressibility, i.e. ρ is constant, the four equations of 2.3 and 2.4 (also known as the Reynolds Equations) can be solved for the four unknown parameters u_i and p as this system is closed. Due to the non-linearity of the Navier-Stokes equations, only for very special conditions the problem is well posed as is the case with laminar flows. In all other cases the solution is very sensitive for small disturbances which makes the solution completely unpredictable; this is the case for all turbulent flows. The only way to 'predict' turbulent flows with these differential equations is by numerical simulation, though this is at present only possible for restricted situations.

2.2 Statistics

As turbulence is a chaotic and fluctuating phenomenon, details are often less important than statistical quantities. Therefore, the time independent statistical quantities are useful tools to characterize the turbulent behavior.

Consider the velocity of a turbulent flow. The measured velocity u can be split in a mean value $\overline{u}$ and a fluctuating part u'.

$$u = \overline{u} + u' \tag{2.5}$$

Splitting such a variable is called Reynolds decomposition.

How to calculate the mean velocity? The first problem encountered is the definition of the mean velocity. Three methods are used: time, space and the ensemble average. For stationary and homogeneous turbulence the three averaging procedures lead to the same result, this assumption is known as the ergodic hypothesis [Hinze, 1975]. Actual turbulent flows are neither really stationary nor homogeneous. Therefore, the averaging procedures can only be carried out for finite values of e.g. the measuring time. However, it can be proved that different approaches of calculating the average converge to the same value [Tennekes and Lumley, 1972] as long as the time interval T has been taken sufficiently large, so the ensemble average equals the time average. For a statistical description of the ensemble average $< U >$, the probability density function (PDF) should be introduced. All probabilistic properties of the random signal $u(t)$ are completely specified by the PDF P. The averages of the velocity signal $u(t)$ are now given by:

$$< U > \equiv \int_{-\infty}^{\infty} uP(u)du = \lim_{T\to+\infty} \frac{1}{T} \int_0^T u(t)dt \equiv \overline{u} \tag{2.6}$$

This time averaged velocity $\overline{u}$ is also known as the first central moment. The second central moment, better known as the variance σ_u^2, can be written as:

$$\sigma_u^2 \equiv \int_{-\infty}^{\infty} (u - < U >)^2 P(u)du = \lim_{T\to+\infty} \frac{1}{T} \int_0^T (u(t) - \overline{u})^2 dt \equiv \overline{u'^2} \tag{2.7}$$

The square root of the variance is called the standard deviation. It measures the spread or width of the PDF, but it is also used in the definition for the turbulence intensity I:

$$I \equiv \frac{\sqrt{\sigma_u^2}}{\overline{u_i}} \tag{2.8}$$

For the mean velocity in this equation, the *local* mean velocity of one of the velocity components has been taken in this report. Besides this definition, there are several other ones for the turbulence intensity like the one after Nieuwstadt [Nieuwstadt, 1998], i.e. the turbulent kinetic energy divided by the square of the mean velocity or the ones applied after Hinze [Hinze, 1975], which is the fluctuating velocity component divided by the maximum velocity, the maximum local velocity or the friction velocity.

Furthermore, the higher order central moments can be specified. The n-th order central moment reads ([Absil, 1995]):

$$\overline{u'^n} \equiv \lim_{T\to+\infty} \frac{1}{T} \int_0^T (u(t) - \overline{u})^n dt \tag{2.9}$$

In the field of turbulence, moments up to the fourth are determined. The third central moment $\overline{u'^3}$ measures the degree of asymmetry of the distribution, a symmetric PDF yields $\overline{u'^3} = 0$. The dimensionless form of this moment is called the skewness factor $S \equiv \frac{\overline{u'^3}}{\sigma_u^3}$. A positive skewness factor indicates that relatively larger positive fluctuations occur more frequently than negative fluctuations and vice versa.

The flatness or peakedness of the distribution is measured by the fourth central moment $\overline{u'^4}$. It weights the large fluctuations heavily and its value is mainly determined by the tails of the PDF. The dimensionless form of the fourth moment is called the flatness factor or kurtosis $K \equiv \frac{\overline{u'^4}}{\sigma_u^4}$.

The skewness and flatness factors are most useful for indicating regions of strong intermittent flow. In the logarithmic region (see section 2.3) there's a tendency for both S and K to approach values of 0 and 3, respectively. These values apply to homogeneous turbulence (Gaussian PDF-shape) and therefore it may be that the flow in this region is tending towards homogeneity. In Browne ([Browne and Dinkelacker, 1995]) more properties of S and K can be found.

2.3 Wall units

The structure of a turbulent flow close to the wall is rather complex. It consists of four more or less distinct layers, each dominated by a different flow mechanism and having a different eddy size. This subdivision is shown in figure (2.3).

Eddies are a kind of circulations, though there isn't an exact definition for it. Pope ([Pope, 2000]) describes them as: *"An eddy eludes precise definition, but it is conceived to be a turbulent motion, localized within a region of size l, that is at least moderately coherent over this region. The region occupied by a large eddy can also contain smaller eddies".*

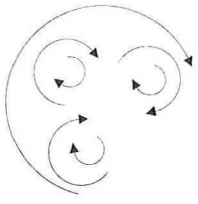

Figure 2.2: A large eddy containing smaller eddies

For a more mathematical description of the layers, first a friction velocity u_* must be defined. Making use of the shear stress at the wall, τ_w, where y=0, this velocity can be calculated with:

$$u_*^2 = \frac{\tau_s(0)}{\rho} = \frac{\tau_w}{\rho} \tag{2.10}$$

For a pipe flow, the shear stress at the wall can be determined with:

$$\frac{\partial p}{\partial x} = 4\frac{\tau_w}{D} \tag{2.11}$$

In which p is the pressure, x is a coordinate parallel to the direction of the flow and D is the diameter of the pipe, see figure 2.1. As equation 2.11 depends on many variables, a more applicable

approach will be utilized which can be found in e.g. Schlichting [Schlichting, 1965]:

$$\tau_w = \frac{\lambda_{fr}}{8}\rho U^2 \tag{2.12}$$

where λ_{fr} is the friction factor. From this equation and equation 2.10 another expression for the friction velocity can be derived:

$$u_* = \sqrt{\frac{\lambda_{fr}}{8}}U \tag{2.13}$$

The friction velocity will be used to make both the velocity and the distance to the wall dimensionless. This gives the opportunity to compare pipe flows with different geometries with each other. The dimensionless parameters will be indicated with subscript + and are given by:

$$u_+ = \frac{\overline{u}}{u_*} \tag{2.14}$$

$$y_+ = y\frac{u_*}{\nu} \tag{2.15}$$

Now the different layers can be defined, making use of Nieuwstadt ([Nieuwstadt, 1998]) and Absil ([Absil, 1995]).

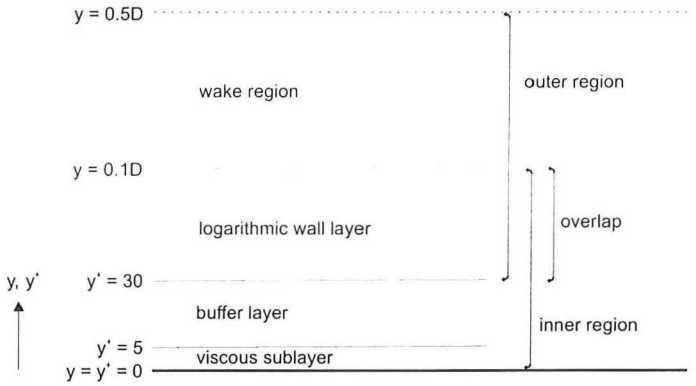

Figure 2.3: Sketch of the different layers in a turbulent pipe flow, at the left side an indication of the size of the layers is given

Wake region $\frac{y}{D} > 0.1$

In the wake region, the eddies scale with the geometry of the flow or the macro scale (see section 2.4). The flow is fully turbulent and the total shear stress is dominated by the turbulent shear stress. The velocity profile can be described with a defect law. For a pipe flow, many descriptions can be found. One of them is (see [Gersten and Herwig, 1992])

$$\frac{\overline{u}}{U_{max}} = \frac{U_{max} - u_* 2.457(\ln(1 + 2.09(\frac{r}{R})^2) - \ln(1 - (\frac{r}{R})^2))}{U_{max}} \tag{2.16}$$

Where U_{max} is the maximum mean velocity, which can be found at the centerline of the pipe, R is the radius of the pipe and r the distance to the centerline of the pipe. Other defect laws can be found in section 6.2.

Logarithmic wall layer $y_+ > 30$, $\frac{y}{D} \leq 0.1$
Getting closer to the wall, the eddies experience more influences of it. Hence, they scale with κ, where κ is the Von Kármán constant, an empirical constant of 0.41. In this layer the turbulent mixing is dominant and the viscous contribution can be neglected. The mixing is so intense, that the turbulent production and the dissipation of energy are in a state of equilibrium, and thus insensitive to external flow properties. Assuming the total shear stress in this layer is approximately constant, leads to a logarithmic velocity profile:

$$u_+ = A \ln(y_+) + B \tag{2.17}$$

Usually A equals the reciprocal value of κ (about 2.5). For a smooth pipe (pipes made of glass or plastic are smooth ([Fay, 1994])) many values for B are given, like 4.9 ([Nikuradse, 1932], 5.5 ([Schlichting, 1965]) or 5.85 ([Townsend, 1956]). Though the best fit with the experimental data goes with ([Bird et al., 1960]):

$$u_+ = 2.78 \ln(y_+) + 3.80 \tag{2.18}$$

Buffer layer $5 \leq y_+ \leq 30$
The buffer layer is the transition layer between the viscous sublayer (see below) and the logarithmic wall layer. The turbulent mixing and the viscous effects are both important. No proper description of the velocity profile can be given here.

Viscous sublayer $y_+ \leq 5$
Finally, the layer the closest to the wall: here the viscous stress dominates the flow, and turbulence can no longer exist. This does not mean that the flow in this layer is laminar, because still velocity fluctuations occur, due to the turbulence in upper layers. The mean axial velocity is directly proportional to the distance from the wall:

$$u_+ = y_+ \tag{2.19}$$

The two layers on top form the outer region, while the three boundary layers form the inner region, so there's a overlap at the logarithmic layer. The velocity profile in the inner region can be written as $u_+ = F(y_+)$. This velocity profile is completely determined by the dimensionless distance from the wall y_+, and is independent of the streamwise position x or the Reynolds number. This universal relation describes the general shape of turbulent boundary layers and is called the law of the wall. This law is represented in figure 2.4.

2.4 Scales

Instead of in terms of layers, another way of examining turbulent flows has to do with the different eddy sizes. Fully developed turbulent flows, say for $Re > 100,000$, can be split up into two scaling regimes: the macro- and the microstructure.

The largest eddies present in turbulent flows, referred to as macro scales, are of the order of the characteristic size of the turbulent region. These large eddies continuously extract energy from the mean flow by instabilities. By a vortex stretching mechanism (the vortexes are being strained by the shear), these larger eddies pass on their energy with the just-smaller eddies by deforming them. Therefore, the vorticity of the smaller eddies will increase. Vortex stretching is an efficient energy

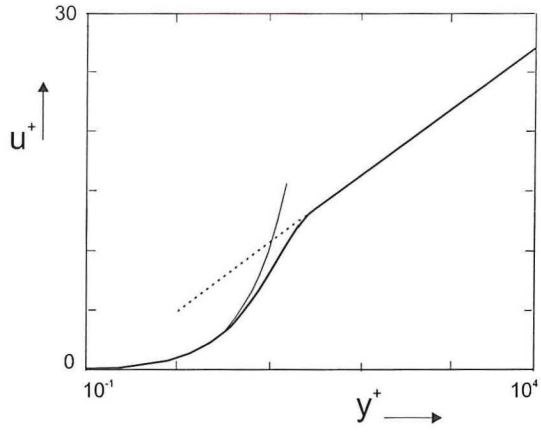

Figure 2.4: Universal velocity profile of the law of the wall

transfer mechanism. The energy cascade is transferring this energy to the smallest structure, the (Kolmogorov) micro scale. At the smallest scales the energy is finally dissipated by (molecular) viscosity and transformed into heat ([Tennekes and Lumley, 1972],[Absil, 1995]).

In a pipe flow the following expressions are applied to define the macro scales, which are directly related with the geometry ([Portela, 1998]).

Macro length scale:

$$L_m \sim \frac{D}{10} \tag{2.20}$$

Macro velocity scale:

$$U_m \sim \frac{\overline{U}}{10} \tag{2.21}$$

Macro time scale:

$$T_m \sim \frac{D}{\overline{U}} \tag{2.22}$$

Where D is the diameter of the pipe and $\overline{U}$ is the average velocity of the pipe flow. The Reynolds number $Re_m = L_m U_m / \nu \gg 1$. In the macro structure the turbulence is anisotropic, due to the vortex stretching in a preferred direction.

Turbulence is very dissipative compared to laminar flow, a turbulent flow will lose its energy rather fast. This can be illustrated with the rate of dissipation, e_{fr}, and the friction factor, λ_{fr}, for flow in tubes. The relation between the friction factor and the Reynolds number is represented in Janssen and Warmoeskerken [Janssen and Warmoeskerken, 1987]. As e_{fr} is proportional to $\lambda_{fr} \cdot \overline{U}^2$, laminar flow is less dissipative. The kinetic energy per unit mass e scales with U_m^2 and as $\frac{de}{dt} = -\epsilon$, the dissipation ϵ scales with the macro structures:

$$\epsilon \sim \frac{U_m^3}{L_m} \tag{2.23}$$

This is the relation of Kolmogorov and it could be read as: a turbulent eddy with energy $\sim U_m^2$ will lose its energy in time T_m. That is, the eddy will break up in this period T_m. Equation 2.23 is a well known link between the macro and micro scales.

Kolmogorov developed his universal equilibrium theory for small scales, based on the assumption that ϵ at the small scales is only controlled by the kinematic viscosity ν and the rate at which these small scales are supplied with energy by the larger scales. Because the geometry is of no importance, the turbulence in the micro scales is isotropic. Kolmogorov introduced the following relations for the micro scales:

Kolmogorov micro length scale:

$$\eta_k \equiv (\frac{\nu^3}{\epsilon})^{\frac{1}{4}} \tag{2.24}$$

Kolmogorov micro velocity scale:

$$\upsilon_k \equiv (\nu\varepsilon)^{\frac{1}{4}} \tag{2.25}$$

Kolmogorov micro time scale:

$$\tau_k \equiv (\frac{\nu}{\epsilon})^{\frac{1}{2}} \tag{2.26}$$

The Reynolds number Re_k based on this small Kolmogorov scales equals 1, so the microstructure is dominated by the viscosity as stated before.

To relate the small scales with the large ones, equation (2.23) is substituted in the relations for the micro scales mentioned above. Divided by the macro scales, this results into:

$$\frac{\eta_k}{L_m} \sim (\frac{U_m L_m}{\nu})^{-\frac{3}{4}} = Re_m^{-\frac{3}{4}} \tag{2.27}$$

$$\frac{\upsilon_k}{U_m} \sim (\frac{U_m L_m}{\nu})^{-\frac{1}{4}} = Re_m^{-\frac{1}{4}} \tag{2.28}$$

$$\frac{\tau_k}{T_m} \sim (\frac{U_m L_m}{\nu})^{-\frac{1}{2}} = Re_m^{-\frac{1}{2}} \tag{2.29}$$

Between the macro and micro scales, the turbulent motion covers a continuous spectrum of temporal and spatial scales. For this region one more scale will be defined as intermediate scale.

If a balance between the production and dissipation in the turbulent kinetic energy balance is obtained (see section 2.5), the length scale has to be much smaller than L_m. This length scale is often discussed in literature (see Tennekes, Nieuwstadt) and is called Taylor's microscale. The index λ is applied to indicate this scale, so L_λ, U_λ and T_λ are the Taylor length, velocity and time scale, respectively. Since the small-scale structure of turbulence at large Reynolds numbers is always approximately isotropic,

$$\epsilon \sim \nu \frac{U_m^2}{L_\lambda} \tag{2.30}$$

is used to define the dissipation. From this relation, the ratio between the Taylor and macro length scale can be solved:

$$\frac{L_\lambda}{L_m} \sim Re_m^{-\frac{1}{2}} \tag{2.31}$$

As $Re_m \gg 1$, the Taylor length scale (a length scale at which dissipation start to take place) is

much smaller than the macro length scale, but it's always considerably larger than the Kolmogorov micro scale!

The assumption of U_m in equation (2.30) is not correct, the velocity is often smaller. The value of the Taylor length scale lies in the comparative ease with which it can be measured, but it is an unsuitable quantity to use as scale in theoretical discussion ([Townsend, 1956]). The way in which these scales can easily be measured, will be explained in section 2.6

2.5 Turbulent kinetic energy

To obtain a better idea about of the dynamics of turbulence, a closer look at the kinetic energy of the flow is very useful. The following theory comes from Nieuwstadt and Townsend.

First, have a look at the mean kinetic energy. Due to the Reynolds decomposition, the measured velocity can be split up in a mean and fluctuating part (eq. 2.5). With the mean part, the kinetic energy per unit mass E can be defined as:

$$E = \frac{1}{2}\overline{u}_i^2 \tag{2.32}$$

In this equation the Einstein summation convention is applied, the energy equations will be summated over the three components. The balance equation for the kinetic energy of the mean flow, where density and temperature fluctuations are neglected, yields for a channel flow:

$$\frac{DE}{Dt} = P_u + T_u + D_u \tag{2.33}$$

with the following three components:
P_u: Production term. This term describes the energy supplied by the average pressure gradient to maintain the mean flow and is always greater than zero.
T_u: Transport term, which redistributes energy.
D_u: Deformation term, describes the energy loss on deforming liquid elements. This term is always negative.
As a channel flow shows much similarity with a pipe flow, equation (2.33) describes the flow in a pipe well. The contributions of these three terms as a function of the distance to the wall is represented in figure 2.5. This figure makes clear that the production is mainly in the outer region, while deformation will mostly occur near the wall. Compensation of the difference ($\frac{DE}{Dt}$ should be zero) is done by the transport term.

Another way of looking at the kinetic energy is the turbulent kinetic energy, which makes use of the fluctuating part of the Reynolds decomposition. The turbulent kinetic energy e is given by:

$$e = \frac{1}{2}\overline{u_i'^2} \tag{2.34}$$

Where again the Einstein summation convention is applied. As mentioned in section 2.2, this term is used in one of the definitions for the turbulence intensity: $I = \frac{e}{\overline{u}^2}$.

As fluctuations are directly related to the chaotic structure of the turbulence, the turbulent kinetic energy is of much interest. Townsend derived the turbulent kinetic energy balances for a pipe flow. For the outer region he stated for this balance and its components in cylindrical coordinates:

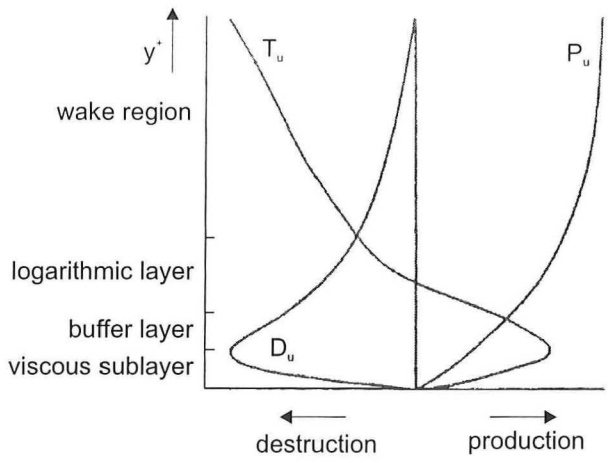

Figure 2.5: Graphical representation of the terms of the kinetic energy balance, after [Nieuwstadt, 1998]

$$\left(\frac{De}{Dt}\right)_{outer} = P_k + T_k + \Pi_k + D_k - \epsilon \tag{2.35}$$

$$P_k = -\overline{u'v'}\frac{\partial \overline{u}}{\partial r}$$

$$T_k = -\frac{\partial}{r\partial r}(\overline{e'v'}r)$$

$$\Pi_k = -\frac{1}{r\rho}\frac{\partial(\overline{p'v'}r)}{\partial r}$$

$$D_k - \epsilon = \nu[\overline{u'\nabla^2 u'} + \overline{v'\nabla^2 v'} + \overline{w'\nabla^2 w'} + \frac{2}{r^2}\left(\overline{w'\frac{\partial v'}{\partial \phi}} - \overline{u'\frac{\partial w'}{\partial \phi}}\right) - \frac{\overline{v'^2} + \overline{w'^2}}{r^2}]$$

Where P_k is the production term which can be interpreted as the rate of production of turbulent energy by working against the Reynolds stress $-\rho\overline{u'v'}$. T_k is the gain of energy by turbulent convection of kinetic energy (e' equals $\frac{1}{2}u_i'^2$). The gain of energy by working on pressure gradients (p' indicates pressure fluctuations) is represented by Π_k. Finally, the viscous transfer and dissipation is given by $D_k - \epsilon$.

The mean flow provides energy to the turbulence by the deformation energy. In figure 2.6 the various terms in the equation for the turbulent energy are shown for the central part of the pipe flow at $Re = 5 \cdot 10^5$. The terms were made non-dimensional by multiplying them by $R \cdot \tau_w^{-\frac{3}{2}}$. In this figure it is seen that production and dissipation of energy are nearly equal for y/R smaller than 0.5, where y is the distance to the wall, while closer to the center of the flow the dissipation exceeds the production level. The level of turbulent energy is maintained by the transport of energy by turbulent convective movements. Only for $y/R < 0.4$, transfer of energy by the action of Π_k is appreciable.

Closer to the wall, that is the inner region, a different approach is followed. Because of the small variations in y, Cartesian instead of cylindrical coordinates can be used. Townsend found for this region:

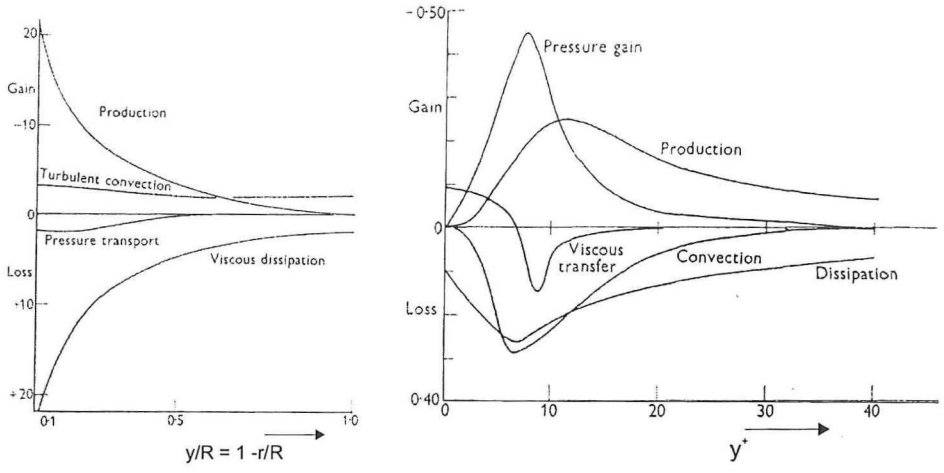

(a) Outer region (b) Inner region

Figure 2.6: Turbulent kinetic energy balances of a pipe flow [Townsend, 1956]

$$\left(\frac{De}{Dt}\right)_{inner} = P_k + T_k + \Pi_k + D_k - \epsilon \tag{2.36}$$

$$P_k = -\overline{u'v'}\frac{\partial \overline{u}}{\partial y}$$

$$T_k = -\frac{1}{2}\frac{\partial \overline{e'v'}}{\partial y}$$

$$\Pi_k = -\frac{1}{\rho}\frac{\partial \overline{p'v'}}{\partial y}$$

$$D_k - \epsilon = \nu(\overline{u'\nabla^2 u'} + \overline{v'\nabla^2 v'} + \overline{w'\nabla^2 w'})$$

As portrayed in figure 2.6 the measured quantities should be expressed in terms of the wall stress and the fluid viscosity for this part of the flow. Just outside the viscous layer ($y_+ > 30$), the production and dissipation are very nearly equal (but opposite to each other), in good agreement with the assumption of negligible energy transfer. The complete curves of the production and dissipation are looking quite similar and so do the terms for the pressure gain and convection.

2.6 Correlation functions

To study the structure of turbulent flow, statistics which are defined for one point in space do not satisfy. A correlation function describes the coherence between two variables at two different points, therefore correlation functions are a useful tool. In this section only an introduction will be given, while sections 6.3 and 6.4 clarify the autocorrelation function and power spectrum in more detail.

Two methods to measure a turbulent variable like $u'(t)$ with $\overline{u'} = 0$ exist:
Eulerian
u' is measured at a fixed point as a function of t, this is usually the case as measurements often take place like this.
Langrangian
$u'(t)$ is measured by travelling with a fluid element. Although this method is hard to realize in practice, this method has some theoretical advantages.

For a stationary turbulent process, the autocorrelation function $\rho(\tau)$ only depends on a time separation $t_1 - t_2 = \tau$. The temporal autocovariance function $R(\tau)$ then yields:

$$R(\tau) = \overline{u'(t_1)u'(t_2)} = \overline{u'^2}\rho(\tau) \equiv \lim_{T\to+\infty} \frac{1}{T}\int_0^T u'(t)u'(t+\tau)dt \tag{2.37}$$

Where $\overline{u'^2}$ is called the Mean Square (MS) value of the turbulence and is by definition independent of time for stationary processes, so the autocorrelation function ACF can be written as:

$$\rho(\tau) = \frac{R(\tau)}{R(0)} = \frac{R(\tau)}{\overline{u'^2}}, \tag{2.38}$$

with one of the properties of the ACF is $\rho(0) = 1$. Another important property is the fact that $\rho(\tau) \to 0$ if $\tau \to \infty$. This means that it is impossible to predict velocities over large time intervals, which is a property of chaos. As a matter of fact, an ACF can determine the "memory" of a chaotic signal. For chaotic processes a characteristic time separation over which correlation exists can be defined:

$$\Gamma = \int_0^\infty \rho(\tau)d\tau \tag{2.39}$$

Where the characteristic time separation Γ is called the integral time scale. In figure 2.7 a graphical representation of this time scale can be found.

Furthermore, the ACF offers the Taylor micro time scale. By taking the second derivative of $\rho(\tau)$ with τ at $\tau = 0$ the Taylor micro scale T_λ can be found. In a more mathematical way (see [Absil, 1995]):

$$\overline{\left(\frac{\partial u'}{\partial t}\right)^2} = -\overline{u'^2}\left(\frac{\partial^2\rho(\tau)}{\partial\tau^2}\right)_{\tau=0} = \frac{\overline{u'^2}}{T_\lambda^2} \tag{2.40}$$

Graphically, a parabola through $\tau = 0$ at an ACF can be fit. The value of τ where this parabola crosses the horizontal axis has the value of T_λ, as can be seen in figures 2.7 and 2.8. For $\tau \sim T_\lambda$ the ACF describes the macro structure, while for $\tau \sim 0$ the micro structure is described. The Taylor length scale L_λ can than be defined as:

$$L_\lambda = T_\lambda \overline{u} \tag{2.41}$$

The Fourier transformation of the correlation function leads to:

$$S(\omega) = \frac{1}{2\pi}\int_{-\infty}^{+\infty} e^{-i\omega\tau}R(\tau)d\tau \tag{2.42}$$

$$R(\tau) = \int_{-\infty}^{+\infty} e^{i\omega\tau}S(\omega)d\omega \tag{2.43}$$

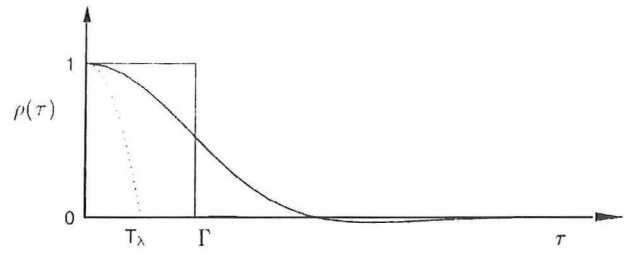

Figure 2.7: Sketch of an ACF in which the integral time scale and the Taylor time scale are represented, after [Absil, 1995]

$S(\omega)$ can be interpreted as the square of the amplitude of a wave with circular frequency ω. Therefore, $S(\omega)$ is called the energy spectrum. The angular frequency ω is related to the time period of a wave via $T_{wave} = 2\pi/\omega$, though eddies can't be compared with waves actually. Waves imply infinite duration while an eddy is finite. Therefore, the spectrum $S(\omega)$ is best interpreted as wave packages with size $\Delta\omega$ centered around frequency ω. As depicted in figure 2.8, $\omega \to \infty$ describes the micro structure, while $\omega \sim 0$ portrays the macro structure.

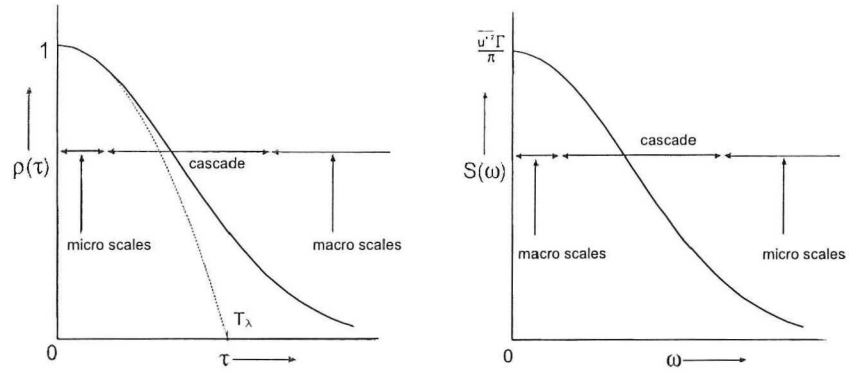

(a) ACF (b) Spectrum

Figure 2.8: Sketch of a temporal correlation function and spectrum, in which different scale regions are indicated, after [Nieuwstadt, 1998]

The way the ACF and energy spectrum are determined as well as more characteristic features can be found in sections 6.3 and 6.4 as mentioned above.

Chapter 3

Flow properties

In the previous chapter turbulence is described in a general way. In this chapter the specific turbulent behavior of a fluid in pipes, contractions, diffusers and venturis will be studied.

3.1 Pipe flow

First, the most elementary and most studied flow will be discussed: the turbulent pipe flow. Nikuradse [Nikuradse, 1932] has been investigating this subject thoroughly in the early 1930's. More recent literature still refers to his results, like Schlichting [Schlichting, 1965]. One of the findings of Nikuradse is that the shape of the turbulent velocity profile depends on the Reynolds number. This result is also known as the Power Law, according to:

$$\frac{u_x}{U_{max}} = \left(\frac{y}{R}\right)^{\frac{1}{n}} \tag{3.1}$$

Where U_{max} the maximum velocity in the x-direction at the centerline and n a factor is, depending on the Reynolds number. The higher the Reynolds number, the higher the value of n and the flatter the velocity profile will be. The factor n can be calculated by making use of the mean (characteristic), U, and maximum velocity of the flow, after Schlichting:

$$\frac{U}{U_{max}} = \frac{2n^2}{(n+1)(2n+1)} \tag{3.2}$$

Besides this mathematical approach to calculate n, this factor can also be derived from the slope of a log-log plot of the velocity versus the distance to the wall. For a fully developed turbulent flow, this line should be straight. Therefore, it is a useful tool to apply on a pipe flow just before an obstruction (i.e. venturi) after which measurements will be performed to be sure that no influences of the geometry upstream will be measured.

An impression of a turbulent flow at three different Reynolds numbers ($4.0 \cdot 10^3, 1.1 \cdot 10^5$ and $3.2 \cdot 10^6$) as well as the application of the Power Law is represented in figures 3.1 and 3.2 where $n = 5$, 7 and 10, respectively. As can be seen in these figures and already mentioned above: the higher the Reynolds number, the flatter the velocity profile is and the higher the value of n.

To estimate the distance from the entrance (or bend) in a pipe at which the velocity distribution

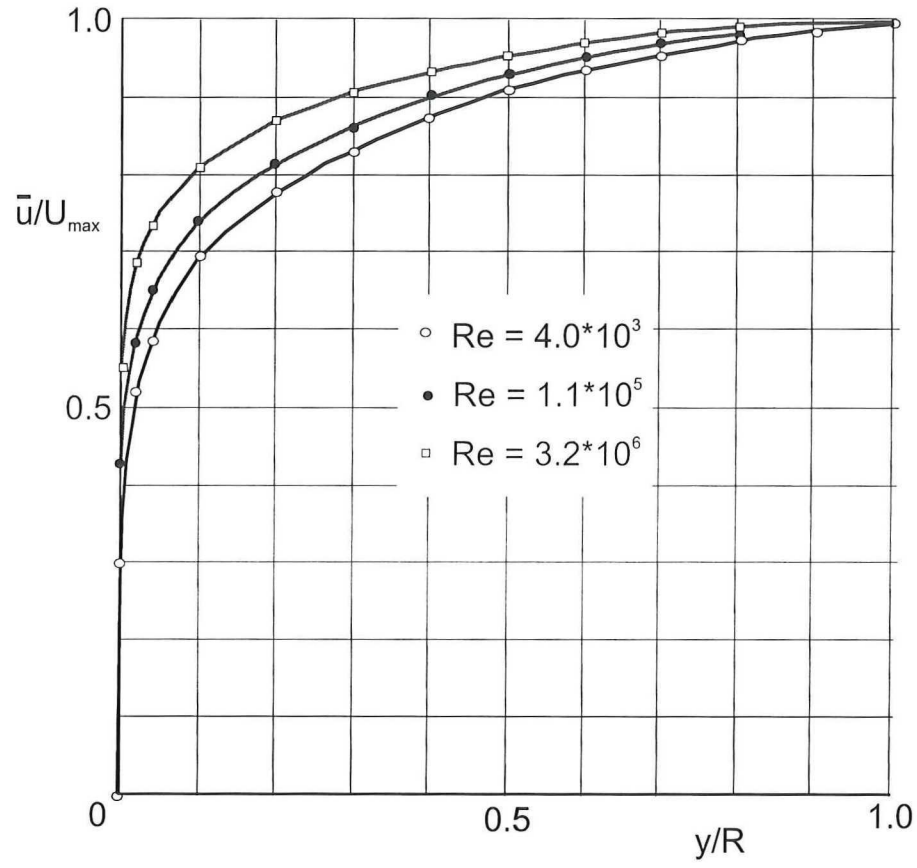

Figure 3.1: Velocity profile of a turbulent flow in a pipe at three different Reynolds numbers, after [Schlichting, 1965].
The higher the Reynolds number, the more flat the velocity profile is.

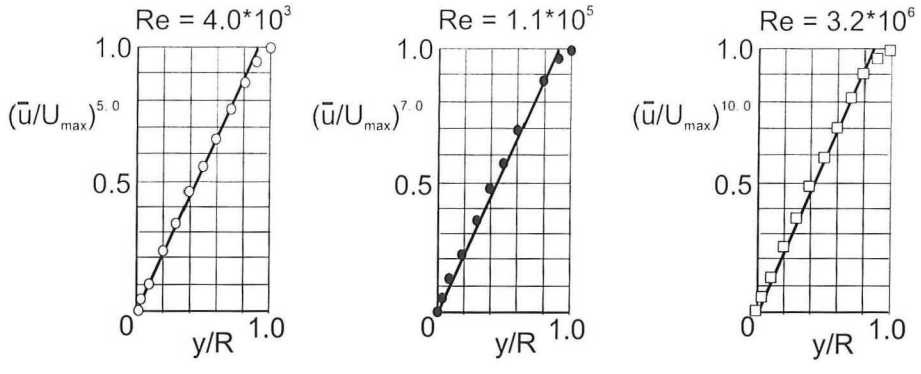

Figure 3.2: Power Law, applied on the velocity profiles of figure 3.1, after [Schlichting, 1965]
The higher the Reynolds number, the higher the value of n is.

approaches the Power Law of equation (3.1), many assumptions are made. While for a laminar flow entry lengths depend on the Reynolds number according to $L_{entrance} \sim 0.03 \cdot D \cdot Re$ (see Schlichting, this implies an entry length of 60 diameters at $Re \sim 2000$), for turbulent flows with much higher Reynolds numbers this is considerably shorter. In Hinze [Hinze, 1975] a brief overview is given for these estimates, where for practical purposes Nikuradse's value of 40 diameters is recommended.

The turbulence intensity is more difficult to compare as many definitions are used and in literature often the applied definition is not mentioned. Nevertheless, Laufer [Laufer, 1954] has done extensively measurements on fully developed turbulent pipe flow. His measurements on turbulence intensity profiles are shown in figure 3.4, which makes use of the definition u'/u_*. Hinze edited this figure for other definitions of the turbulence intensities, see figures 3.3, 3.4 and 3.5. Close to the wall the turbulence intensity first increases until a maximum value is reached, which position depends on the Reynolds number (the more turbulent, the shorter is the distance to the wall). After this peak the intensity decreases to about one third of the peak value at the centerline of the pipe. At this position $u'/u_* \sim 0.8$, see figure 3.4. The same holds for u'/U_{max} which reaches a value of about 0.03 at the centerline.

3.2 Venturi design

Measurements on the properties of a flow in a venturi and downstream this device can not be compared to literature easily for several reasons. First of all, not many data are available about venturi flows and the data that are available are valid for flows with lower Reynolds numbers. The second problem is the shape of a venturi. The convergence and divergence angles as well as the length of the throat vary a lot.

Currently, as a standard for single phase flow, the International Standard Organization (ISO) prescribes a venturi with a total convergence angle of 21°, while the divergence angle has to be between 7 and 15°. This design is known as the ISO 5167 standard.

The National Engineering Laboratory (NEL) situated in the UK, however, is researching the (shape of the) venturi for application on wet gas measuring, as no standard for this kind of measurements is set up to know. According to their research, for the contraction of a venturi a total convergence angle of 21° has been chosen. The shape of the contraction is very important, as it causes the streamlines to converge. Furthermore, the contraction should prevent disturbances like recirculations to occur in the venturi entrance region. The total diffuser angle is of less importance in venturi design, though its value is usually smaller than the convergence angle to accompany the streamlines gradually to a larger cross section. Due to this progressive transition, recirculations will be smoothed away.

Furthermore, the American Society of Mechanical Engineers (ASME) has been investigating shapes of venturis for a long time. Many manufactured venturis are build after their standards, like the short and long form venturis. Both have a total contraction angle of 21°, which suits wet gas metering, and have a total diffuser angle of 15 and 7°, respectively. The latter is better with respect to pressure recovery.

Before having a closer look at venturi flows, a more detailed study about contractions and diffusers will be given.

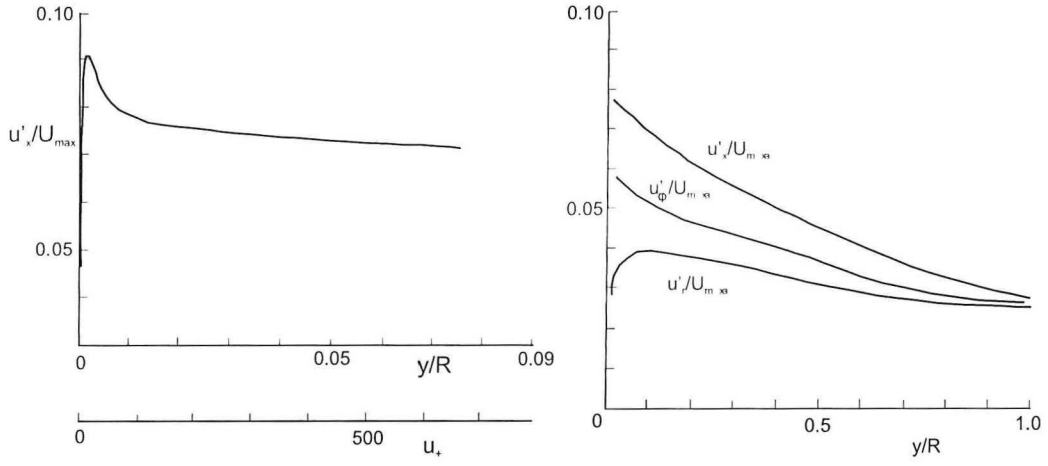

(a) Near the wall (b) Total profile

Figure 3.3: Relative turbulence intensity, defined as u'/U_{max}, in pipe flow, after [Hinze, 1975]

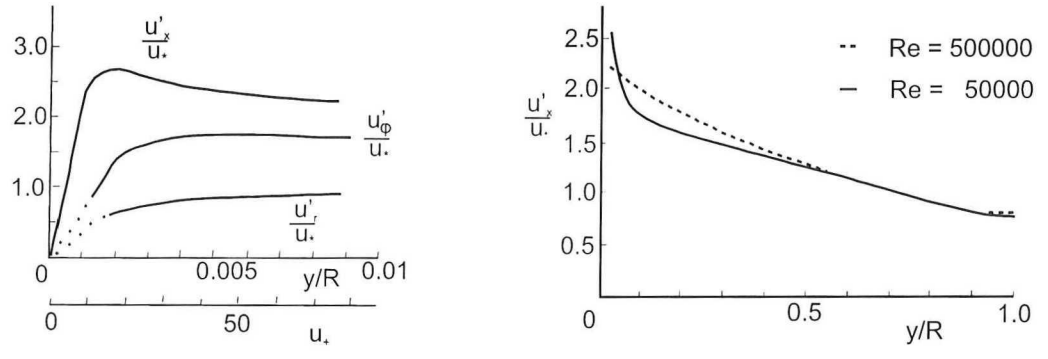

(a) Near the wall (b) Total profile

Figure 3.4: Relative turbulence intensity, defined as u'/u_*, in pipe flow, after [Hinze, 1975] and [Laufer, 1954], respectively

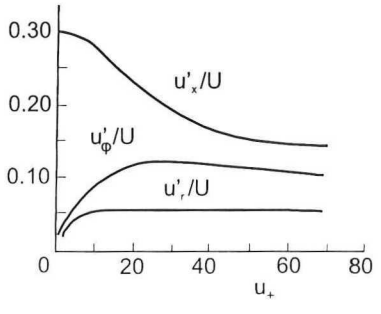

Figure 3.5: Relative turbulence intensity in pipe flow, defined as u'/U, after [Hinze, 1975]

3.3 Contractions

A contraction naturally leads to a rapid increase in mean velocity (equal to the inverse of the area ratio) and a considerable flattening of the velocity profile. Besides this, the turbulence will be appreciably reduced by passing through a contraction. As the contraction ratio increases, the reduction of the turbulence intensities will increase, because the velocity fluctuations become smaller compared to the average velocity.

In the article of Spencer et al. [Spencer et al., 1995] measurements on a contraction with water flow are described and compared with computer simulations. This contraction has a total angle of 40° and the shown graphics are the results of measurements at $Re = 100,000$. In figure 3.6 the design of the contraction is represented. As mentioned above, the flattening of the velocity profile is noticeable and the calculations approach the measurements (figure 3.7). Despite this, the prediction of the turbulent kinetic energy fails completely, the turbulence level even increases after the contraction while the measurements show a (correct) decrease! N.B. The flow at station 1 was close to, though not identical with, fully developed turbulent flow.

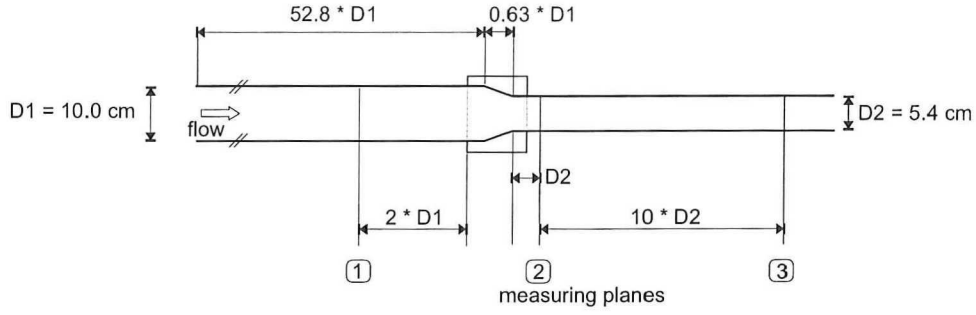

Figure 3.6: Position of the measuring planes of the contraction measurements, after [Spencer et al., 1995]. The total contraction angle is 40°.

In practise, the natural behavior of contractions is convenient for wind tunnels where they are applied to obtain a uniform velocity field and low turbulence intensities. Although the flow field after this contraction should satisfy several conditions, the contraction itself is often designed by eye. The most important thing is a smooth and gradual transition to the smaller region. As a result of the wish to achieve low turbulence intensities, the contraction ratio for 'recent' wind tunnel design is as high as 16 [Batchelor and Shaw, 1944] and 6 to 9 for the smaller tunnels [Mehta and Bradshaw, 1979]. Only, this causes a too rapid change of the velocity and a velocity decrease at the walls. To solve these problems, in front of the contraction a number of honeycombs and screens are positioned to reduce the turbulence intensity and make the velocity profile more uniform.

3.4 Diffusers

The flow field and properties in diffusers have been studied far more thoroughly, especially by Azad who wrote several articles about his research of this topic the last 30 years. Robertson & Calehuff (1957) already found that the longitudinal microscales of turbulence remained remarkably constant across and along the developing diffuser flow. Usually, flow through diffusers does not possess the simplified features of fully developed flow. It might be expected that any mathematical model of turbulence with reference to the existing experimental data for symmetric equilibrium flows will be inadequate when used to predict diffuser flows in moderate to strong adverse pressure gradients

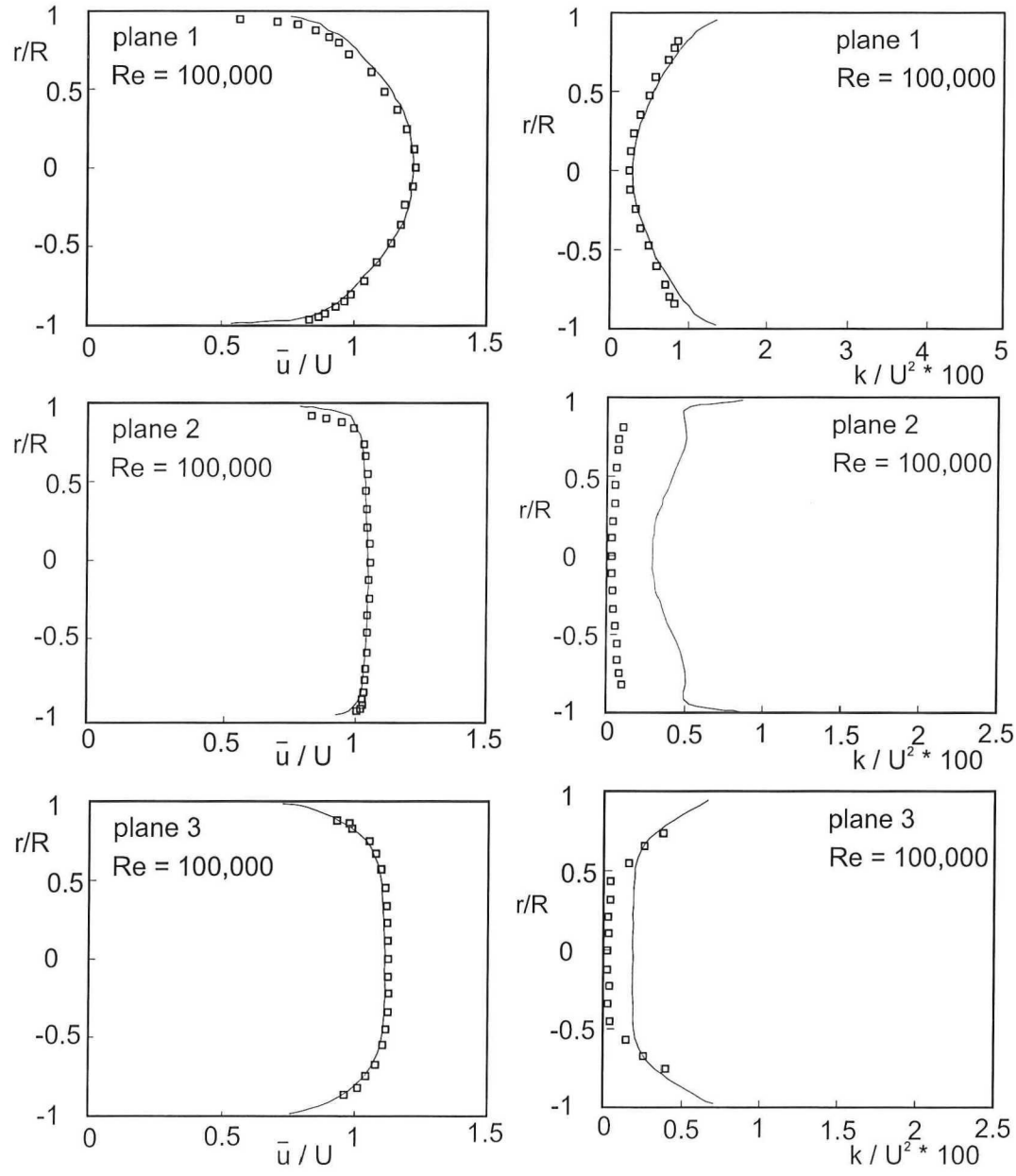

(a) Mean axial flow velocity distributions

(b) Distribution of turbulent kinetic energy, where $e = 1/2(\overline{u'}^2 + \overline{v'}^2 + \overline{w'}^2)$

Figure 3.7: Distribution of the mean axial velocity and turbulent kinetic energy at the three measuring planes of figure 3.6, after [Spencer et al., 1995]. □ results of Lab C, line results of Calc 1. Re = 100,000 at the reference plane, i.e. plane 1.

(APG) [Okwuobi and Azad, 1973]. Azad et al. therefore realized a lot of experiments to acquire more quantitative data.

Flow through a conical diffuser develops towards a jet-type of flow with a considerable increase in turbulence levels. The flow is subject to an APG which is strong enough to cause separation of the mean flow. Efficient conical diffusers should have a total divergence angle of $6 - 8°$. In such a diffuser, the APG is strong enough to cause appreciable instantaneous flow reversals (instantaneous backflow up to 30% of the time), but the time-average flow is non-separated. A sketch of the metal diffuser referred to in this section is shown in figure 3.8.

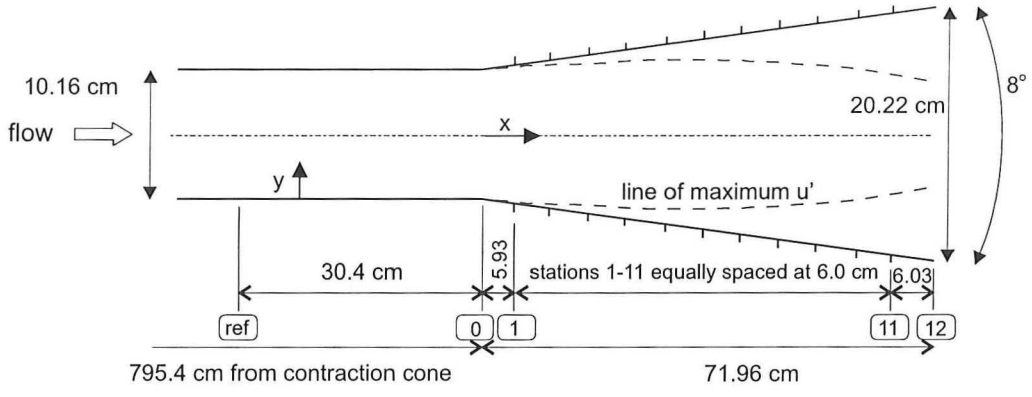

Figure 3.8: Sketch of a diffuser and the measurement planes, after [Okwuobi and Azad, 1973]

3.4.1 Velocity profile

Looking at the velocity profiles of different positions in the diffuser (figure 3.9) a decrease in the slope and magnitude, especially near the wall, is visible. This is due to the change in the diffuser cross-section in the axial direction which causes a reduction of U, as demanded by flow continuity, and a simultaneous rise in pressure. Because the radial variation of the static pressure is comparatively small, the amount by which the axial velocity is reduced would tend to be of the same order of magnitude across the diffuser, but it is modified by shear forces. The velocity profiles therefore show the biggest change of shape in regions with low velocity, i.e. near the wall. The profiles of stations 6 to 10 start showing points of inflection which are usually observed in boundary layers in adverse pressure gradients [Okwuobi and Azad, 1973].

Owing to these velocity profiles, the standard logarithmic law of the wall (see figure 2.4) does not hold for the profiles obtained in this conical diffuser. The deviation from the log-law increases at the downstream stations. In the wall region, the profiles deviate downwards from the standard log-law of the wall. The breakdown of this universal law seems to start before instantaneous flow reversals. Hence, the presence of strong APG in a conical diffuser produces mean velocity profiles that do not fit the law of the wall as can be seen in figure 3.10 . More velocity distributions in u_+, y_+ coordinates can be found in [Trupp et al., 1986] and [Singh and Azad, 1995]. Note that in the near-wall region any errors in u_* can have significant influence in velocity distributions in u_+, y_+ coordinates!

The Reynold shear stress $(-\overline{\rho u' v'})$ near the wall rises to a maximum which increases and rapidly moves away from the wall as the flow proceeds downstream [Okwuobi], while the law of the wall is based on the assumption that the shear stress in the inner region of the wall layer is independent of y. Thus, the failure of the velocity profiles in dimensionless coordinates to exhibit logarithmic

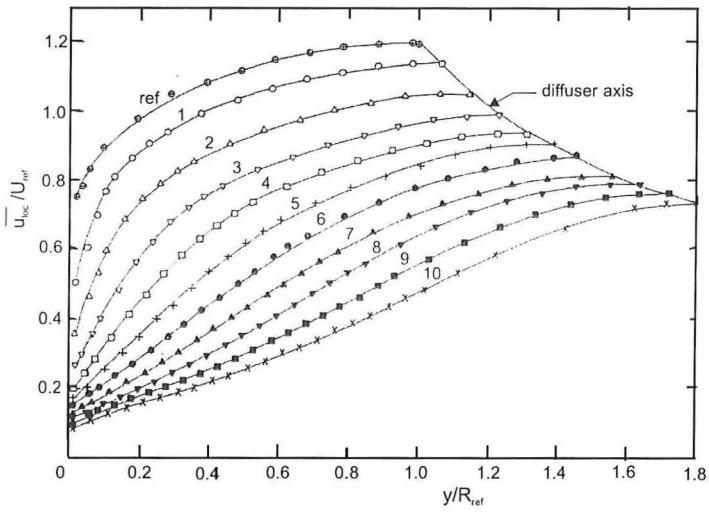

Figure 3.9: Velocity profiles in a diffuser. The local velocities are normalized with the characteristic (average) velocity at the reference station (pipe flow, Re = 293,000). The distance to the wall is normalized with the radius of the pipe, R_{ref}. After [Okwuobi and Azad, 1973]

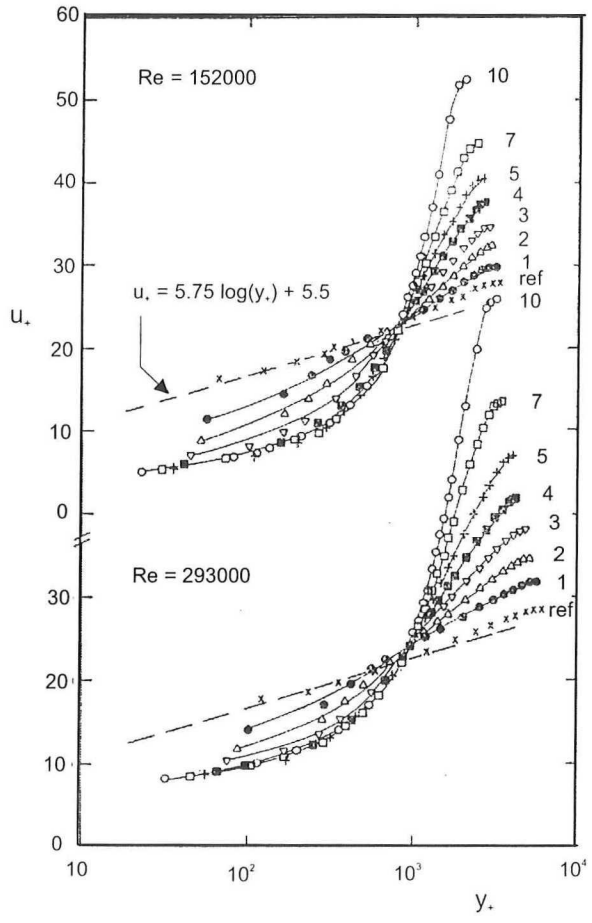

Figure 3.10: Velocity profiles in wall units at two Reynolds numbers in a diffuser, after [Okwuobi and Azad, 1973]

variation near the wall can be attributed to the strong APG in a conical diffuser [Singh and Azad, 1995]. The variation of the total shear stress τ_s/ρ, which is the sum of the viscous shear and the directly measured Reynolds stress according to equation 3.3 is depicted in figure 3.11.

$$\frac{\tau_s}{\rho} = \nu\frac{\partial u}{\partial y} - \overline{u'v'}, \tag{3.3}$$

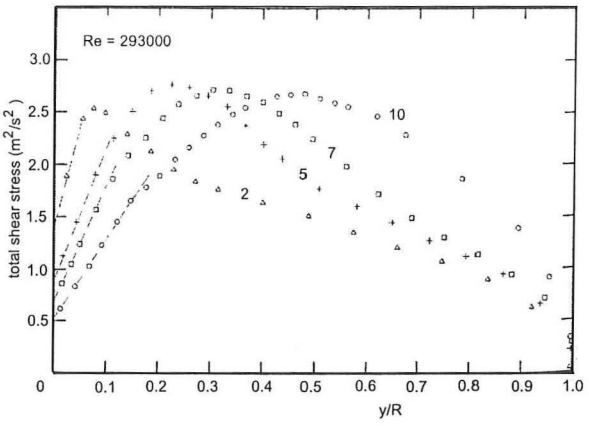

Figure 3.11: Variation of the total shear stress, after [Okwuobi and Azad, 1973]

3.4.2 Turbulence intensity

In figures 3.12 and 3.13 the turbulence intensities according to two different definitions are depicted, $u_x^{'}/U_{max}$ and $u_x^{'}/u_*$, respectively. As can be seen in figure 3.12, the turbulence increases considerably in a diffuser for both directions. The degree of anisotropy decreases from the wall to the diffuser axis. The level of the reference station (pipe flow) is quite similar to Laufer's experiments. The components of the turbulence intensity non-dimensionalized with the friction velocity (figure 3.13) shows a peak which is located very close to the wall near the inlet and which moves progressively towards the pipe axis in the streamwise direction.

3.4.3 Turbulent energy

As the peak of the turbulence intensity shifts to the centerline in the downstream direction, so does the production of turbulent energy, as can be found in Azad [Azad, 1996]. The following information comes from this article as well. As one proceeds from the inlet of the diffuser, the production at the wall decreases, whereas there is an increase of the production of kinetic energy per unit mass in the core region. The peak of the production shifts from the wall to the core region, and its value first decreases and finally comes to an asymptotic value in the outlet region of the diffuser flow.

The same story holds for the dissipation of turbulent kinetic energy, though it does not equal the production term. Because these two terms do not balance each other at each location in the diffuser, the transport terms (mean and turbulent) come into play to bring the physical system into balance, see also [Okwuobi and Azad, 1973]. Advection partly balances dissipation in the wall layer and partly turbulent diffusion in the core region. The pressure term is negligible, so

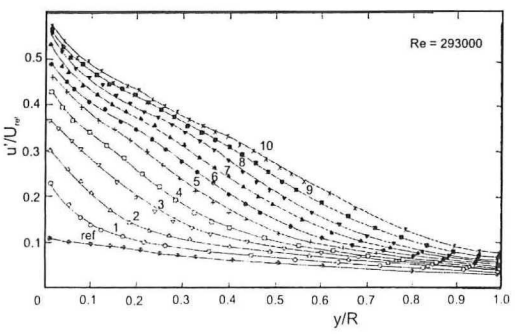

(a) Velocity fluctuations in the flow direction

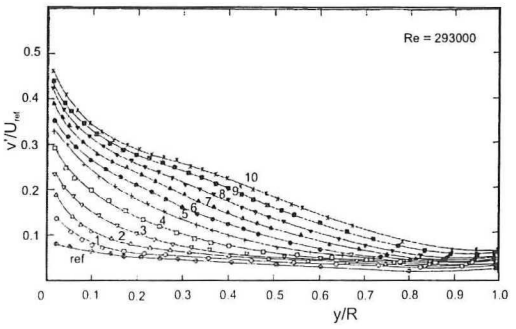

(b) Velocity fluctuations perpendicular to the flow direction

Figure 3.12: Distribution of the turbulence intensities at different stations in a diffuser. The velocity fluctuations are normalized by the local average velocity at the reference station in the flow direction. After [Okwuobi and Azad, 1973]

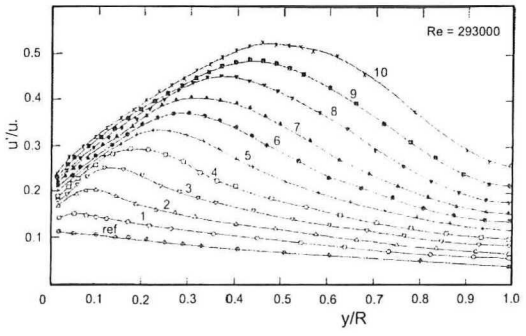

(a) Velocity fluctuations in the flow direction, normalized by the friction velocity at the reference station

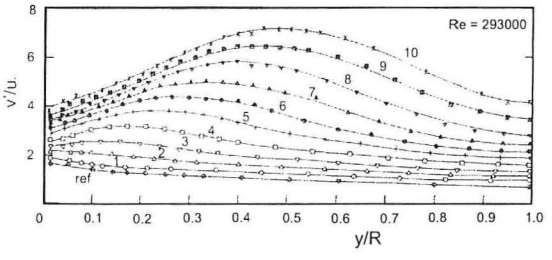

(b) Velocity fluctuations perpendicular to the flow direction, normalized by the friction velocity at the reference station

Figure 3.13: Distribution of the turbulence intensities at different positions in a diffuser. The velocity fluctuations are normalized by the friction velocity at the reference station. After [Okwuobi and Azad, 1973]

the remainder term (diffusion), partially balances advection in the core region and joins with it to balance dissipation in the wall region.

The advection term, which has an initially zero magnitude in the pipe, rises sharply at the first location of measurements in the diffuser, stays nearly at the same value, and then finally decreases approximately to zero at the third station. Generally, the ratio of advection to production can be taken as a measure of perturbation of the flow, and this ratio is very large (about 40 %) at the beginning of the diffuser.

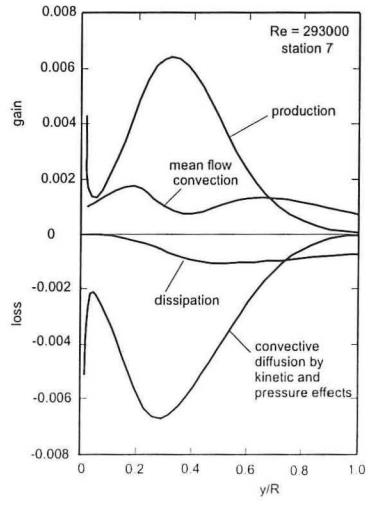

Figure 3.14: Sketch of the turbulent kinetic energy balance of station 7, after [Okwuobi and Azad, 1973]

The energy balance at position 7 ($x = 41.93$ cm) is shown in figure 3.14. The viscous work at this position is about two orders of magnitude less than the production. The profile of the energy production shows a local minimum value near the wall ($y/R = 0.03$); this is a result of the decrease of $\partial u_x/\partial y$ close to the wall (see figure 3.9). From this energy balance, the following conclusions may be drawn:

- In the region $0.8 \leq y/R \leq 1.0$, the dissipation is mostly balanced by the mean flow convection. This picture is different from that for fully developed pipe flow, where the dissipation is mostly balanced by the kinetic energy diffusion while the mean flow convection is zero.
- For $0.2 < y/R < 0.8$, the energy production and the convective diffusion due to kinetic and pressure effects are approximately equal in magnitude while the mean flow convection, which is less than the production, is approximately equal in magnitude to the dissipation. The increased significance of the convective diffusion is due to diffusion in both streamwise and transverse directions.
- For $0.01 < y/R < 0.2$, the rate of energy production and convection by mean motion is mostly balanced by the rate of convective diffusion.

Summarizing: the magnitude of the convective diffusion due to kinetic and pressure effects is increased in relation to that of the dissipation and is comparable with that of the production. This is totally different from fully developed pipe flow, where the rate of production is comparable with the dissipation.

3.4.4 Flow reversal

Studying the instantaneous reversal zones helps in understanding the separation processes in highly turbulent flows. The degree of detachment of a turbulent flow can be quantitatively presented in terms of the reverse-flow parameter χ, defined as the fraction of time that the flow moves in an upstream direction. In the diffuser of figure 3.8 three distinct regions of flow development can be indicated, based on the value of χ_w 0.05 mm from the wall. The initial stage runs from the inlet to 0.15 m, which is called the location of incipient detachment (ID); the final stage from approximately 0.40 m to 0.72 m and in between these two regions the intermediate stage can be found. At location ID in the initial stage, almost no flow reversals will take place (χ equals 0.01). The location at $x \approx 0.40$ m is the position of intermittent transitory detachment (ITD). At this point χ equals 0.20. After this point, the flow will approach the position of transitory detachment (TD) where $\chi \approx 0.50$, though in the used diffuser only a value of 0.30 will be achieved at x =0.695 m. These regions are shown in figure 3.15.

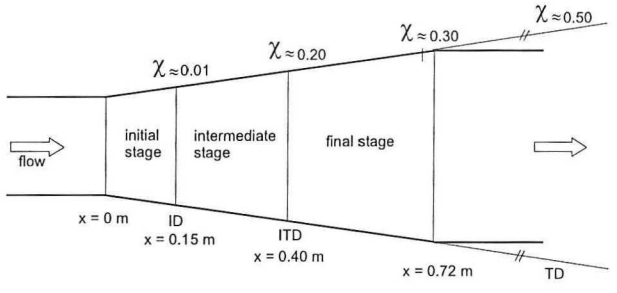

Figure 3.15: Sketch of the distinct zones in a diffuser, after [Singh and Azad, 1995]

The exact positions of ID and ITD depend on the Reynolds number and on the position at which the value of χ at the wall is specified. For Reynolds numbers of $6.9 \cdot 10^4$ or $1.2 \cdot 10^5$ the values mentioned above will apply, but at appreciable higher Reynolds numbers, the amount of instantaneous flow reversals decreases, the positions of ID and ITD move slowly downstream and the region of instantaneous backflow is suppressed. While the value of χ decreases considerably towards the core region, defining the value of it at the wall at a larger distance of the wall will shift the positions of ID and ITD more downstream as well. Figure 3.16 shows the distribution of the wall value of χ and the friction velocity along the axial direction. In this figure, it can be seen that χ increases rapidly in the intermediate stage and that its values are slightly higher for the lower Reynolds number. Furthermore, it seems that the increase of intermittent flow separation in the latter half of the diffuser is suppressed due to rapid growth of turbulence in the core region. The distributions of χ at three positions in the diffuser are shown in figure 3.17.

3.4.5 Downstream of the diffuser

In Spencer et al. [Spencer et al., 1995] measurements and calculations in and downstream of a diffuser are represented. This diffuser has a total divergence angle of 10°. The set-up for these experiments is depicted in figure 3.18. As can be seen in this picture, one measuring plane is just in front of the diffuser and is used as a reference station, while two other planes are situated at one and ten diameters downstream, respectively. As mentioned before, flow through the conical diffuser develops towards a jet-type of flow, which follows also from figure 3.19*a*, plane 2. At station 3 the velocity profile is flatter than the one at station 1 (whereas the local Reynolds number is lower at position 3!), though it looks like an almost developed turbulent flow. In fact, this is not

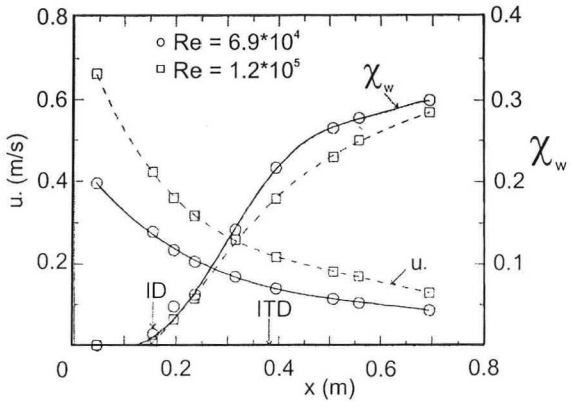

Figure 3.16: Distribution of the friction velocity u_* and the wall value of the reverse flow parameter χ_w in a conical diffuser, after [Singh and Azad, 1995]. The indications of ID and ITD are valid for Re = 69,000.

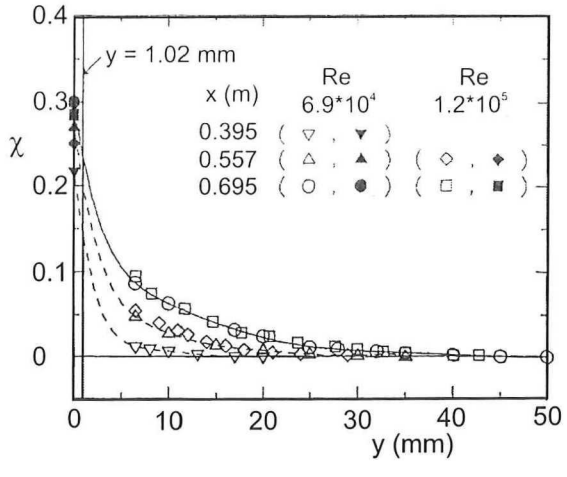

Figure 3.17: Profiles of the reverse flow parameter χ at three stations. Full symbols indicate the wall values χ_w, after [Singh and Azad, 1995]

the case. Even at the third station the turbulent kinetic energy has not reached the level of station 1, as the value at the centerline is still 4 times higher (figure 3.19*b*).

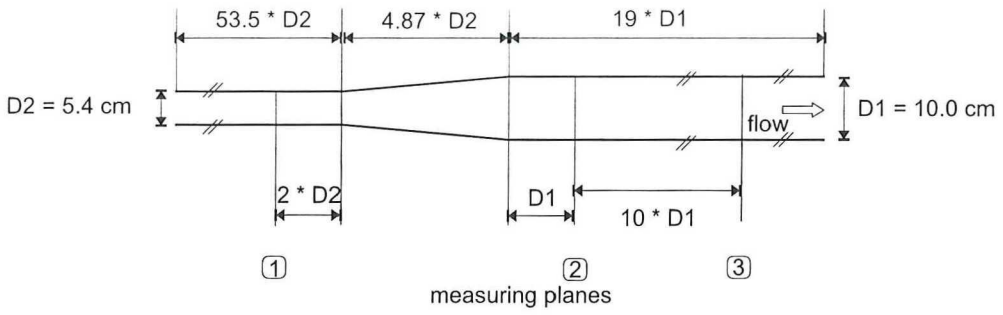

Figure 3.18: Position of the measuring planes of the diffuser measurements, after [Spencer et al., 1995]. The total diffuser angle is 10°.

Comparison of the measurements with the calculations *Calc*1, done by one of the participating institutes of Spencer's investigation, shows that the latter do not predict the velocity and turbulent kinetic energy profiles well. The simulations under predict the centerline velocity by at least 25%. While the shape of the kinetic energy profile at station 2 is well predicted (although only 50% of the actual value), this does not hold for the shape at station 3. The presented calculation curves result from an algebraic stress model, rather than an eddy viscosity model, whereas these results are slightly better than those obtained using the standard $k - \epsilon$ model. It should be noted however, that the numerical solution of the momentum equations depends much more on the turbulence model than it does in the contraction case. This is because the turbulence levels increase substantially as the flow passes through the diffuser, so that the turbulence terms in the equation of motion contribute much more significantly to the overall momentum balance than they do in the contraction case where they become very small quite rapidly.

3.5 Venturi flow

In order to obtain experimental data useful in evaluating turbulence models for computational fluid dynamics, Deshpande and Giddens [Deshpande and Giddens, 1980] have done extensive measurements of axial and tangential r.m.s. turbulence velocity components at a Reynolds number of 15,000 in a tube with a constriction. This constriction is shown in figure 3.20, where Z implies the number of diameters down- or upstream of the center of the obstruction. The constriction has a smooth cosine shape. It should create an intensely turbulent field. Upstream this device, there is a pipe of 37 diameters, while downstream a pipe of 13 diameters is used. The following part is based on the article of Deshpande and Giddens.

Although the entrance length is rather short, the velocity profile 4 diameters upstream (at $Z = -4$) is in reasonable agreement with the fully developed Power Law profile ($n \cong 6.4$, see section 3.1) for this Reynolds number. At the entrance plane of the constriction ($Z = -2$), the measured profile was very close to that at $Z = -4$. This profile, as well as 10 others, is depicted in figure 3.21. A noticable acceleration is demonstrated by the data points for $Z = -1$ and a plug-like profile is seen at the throat ($Z = 0$). Interestingly, at this station the maximum velocity does not occur at the centerline but at a near wall position! This result can be found for all measurements mentioned in the article of Deshpande i.e. $Re = 5,000$, 10,000 and 15,000. Flow recirculation is distinctly apparent in the profiles from $Z = 1$ to 4, while flow reattachments take place just prior to $Z = 5$. The profiles following this station reflect a gradual return toward the upstream condition. This

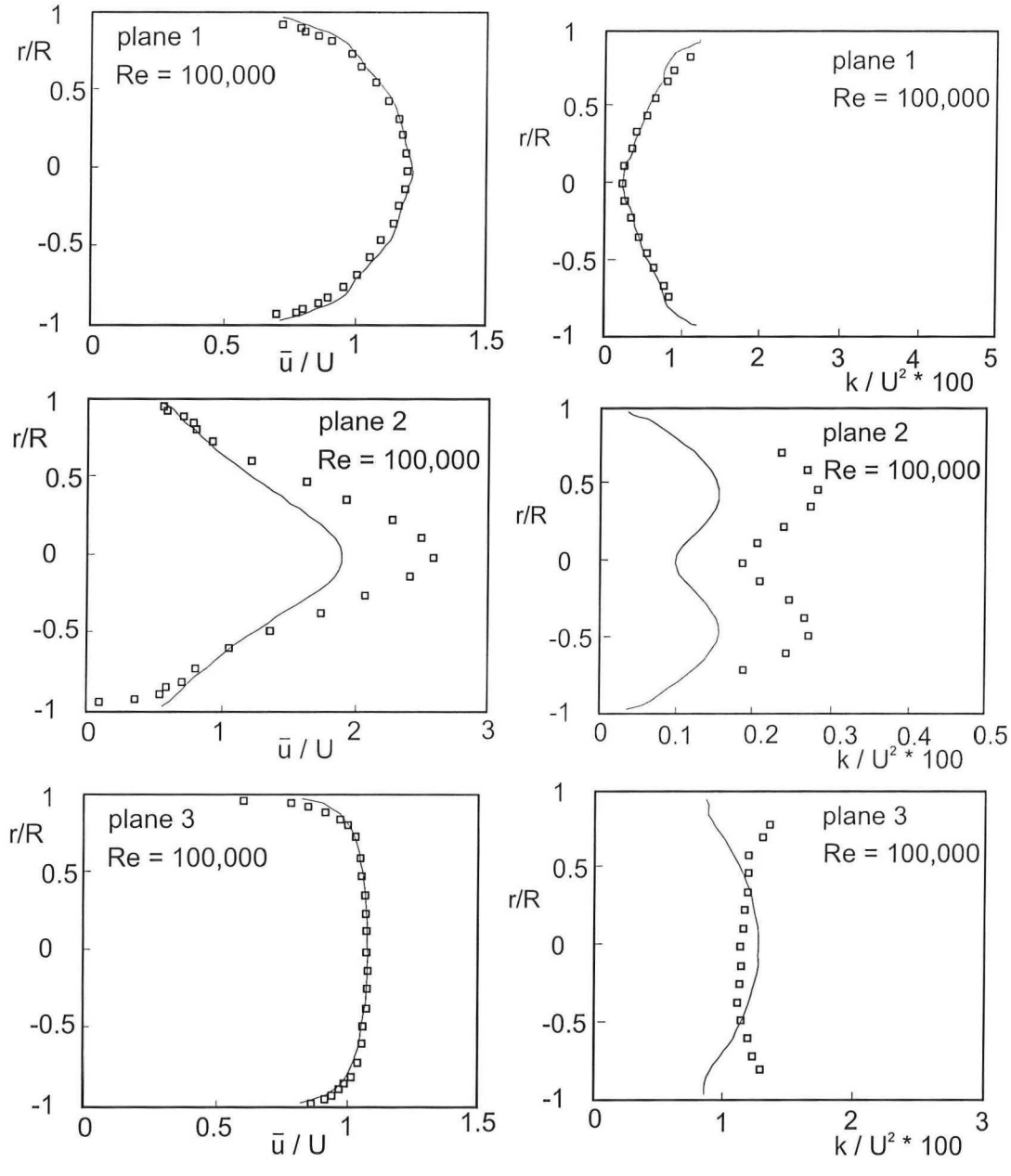

(a) Mean axial flow velocity distributions

(b) Distribution of turbulent kinetic energy, where $e = 1/2(\overline{u'}^2 + \overline{v'}^2 + \overline{w'}^2)$

Figure 3.19: Distribution of the mean axial velocity and turbulent kinetic energy of a diffuser flow at the three measuring planes of figure 3.18, after [Spencer et al., 1995]. □ results of Lab C, line results of Calc 1. Re = 100,000 at the reference plane, i.e. plane 1.

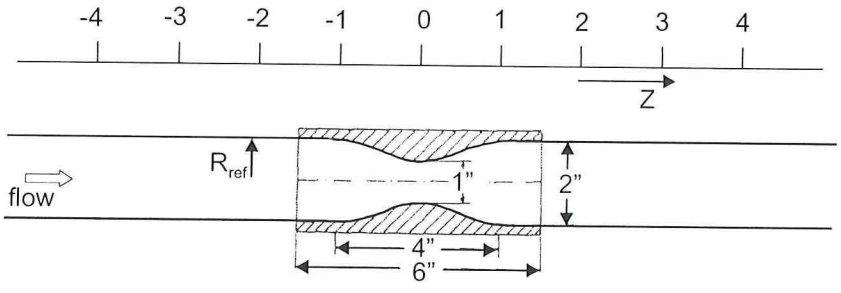

Figure 3.20: Dimensions of the constriction in a tube and definition of the Z direction. Note that the dimensions are in inches, after [Deshpande and Giddens, 1980]

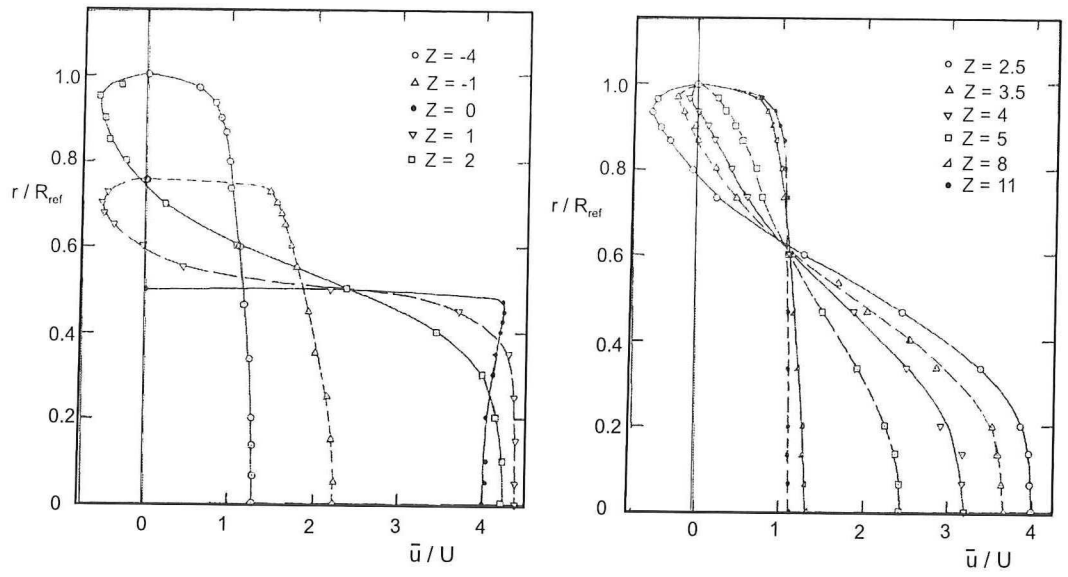

(a) Profiles of Z = -4, -1, 0, 1 and 2

(b) Profiles of Z = 2.5, 3.5, 4, 5, 8 and 11

Figure 3.21: Axial velocity profiles at Re = 15,000. After [Deshpande and Giddens, 1980]

return is not monotonic, however, in that the profile at $Z = 11$ is flatter than the upstream profile and, consequently, flatter than the relevant Power Law shape. Note that the turbulence intensities at this station remain considerably -about 2 to 5 times- greater than the fully developed pipe flow values.

Figure 3.22 illustrates the axial variation of the centerline velocity. Again, it is seen that the velocity dips under the fully developed value, bearing an interesting similarity to the case of turbulent flow development in the entrance region of a pipe where the centerline mean velocity reaches a maximum and then recedes to its final value as flow develops. Flows at the three Reynolds numbers differ substantially beyond the nozzle exit. The higher the Reynolds number, the larger the decrease of the velocity after the obstruction and the faster the velocity downstream will equal the value of the fully developed pipe flow.

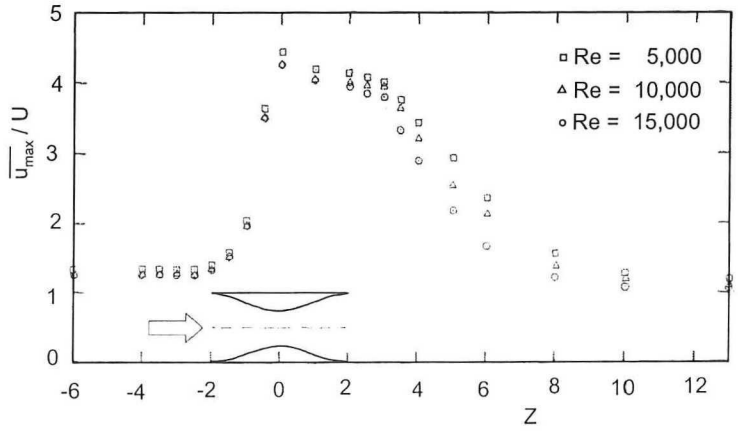

Figure 3.22: Axial variation of the centerline velocity for different Reynolds numbers, after [Deshpande and Giddens, 1980]

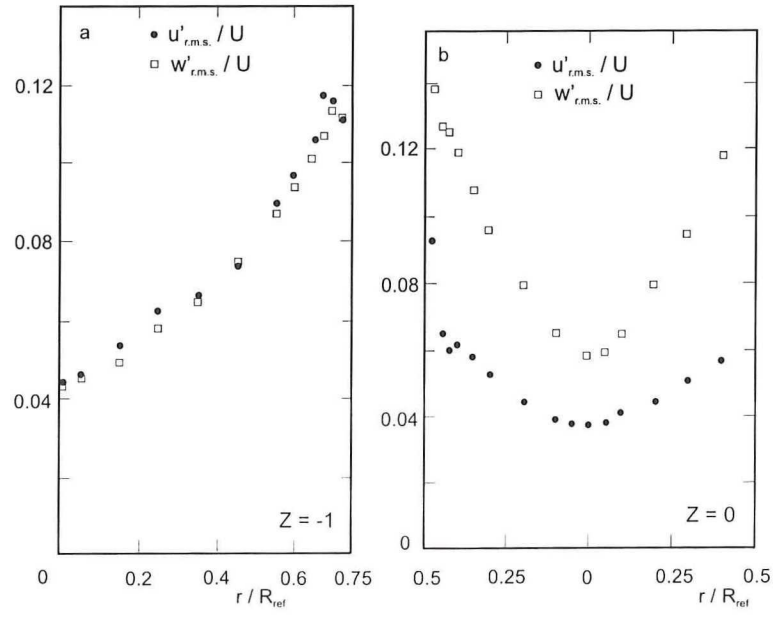

Figure 3.23: Profiles of turbulence velocity components at Re = 15,000 of Z = -1 and 0 (throat), after [Deshpande and Giddens, 1980]

The turbulent velocity fluctuations are represented in figure 3.23 for stations $Z = -1$ and $Z = 0$

(throat). The turbulence velocities u'_{rms} and w'_{rms} are non-dimensionalized by the bulk velocity U upstream of the contraction, the mean velocity of the pipe flow. The axial component of the turbulent velocity fluctuations attenuate slightly in the converging section, while the azimuthal component is amplified. This is consistent with the data of Hussain & Ramjee (1976) for wind tunnel turbulence. In the diverging section, sharp increases in u'_{rms} and w'_{rms} occur. Figure 3.24 present those values at $Z = 1, 2, 4, 6$ and 11. The axial component is greatly amplified in the shear region at $Z = 1$. The largest fluctuations occur in the shear region. Beyond $Z = 1$, the value of $w'_{r.m.s.}$ was seen to be smaller than $u'_{r.m.s.}$. This is due to the mean kinetic energy being siphoned primarily into $u'_{r.m.s.}$, and later redistributed into $v'_{r.m.s.}$ and $w'_{r.m.s.}$. It is not until downstream of reattachment that the centerline fluctuations are the largest at the given station. Downstream, there is a very clearly anisotropic behavior with u'_{rms} often being more than 50% larger than w'_{rms}. Two-equation turbulence models will thus be hard pressed to give accurate flow predictions in this region.

For measurements in the throat of a venturi, March [March, 1998] found for his measurements with an upstream $Re \sim 400,000$ an significant decrease in the turbulence intensity near the axis of the pipe. Whereas the turbulence intensity in the pipe upstream of the constriction (diameter of 108 mm) was found 7%, the intensity at the throat (diameter of 50 mm) was only 1%. The used venturi had a contraction and diffuser angle of 20.3 and 14.5°, respectively.

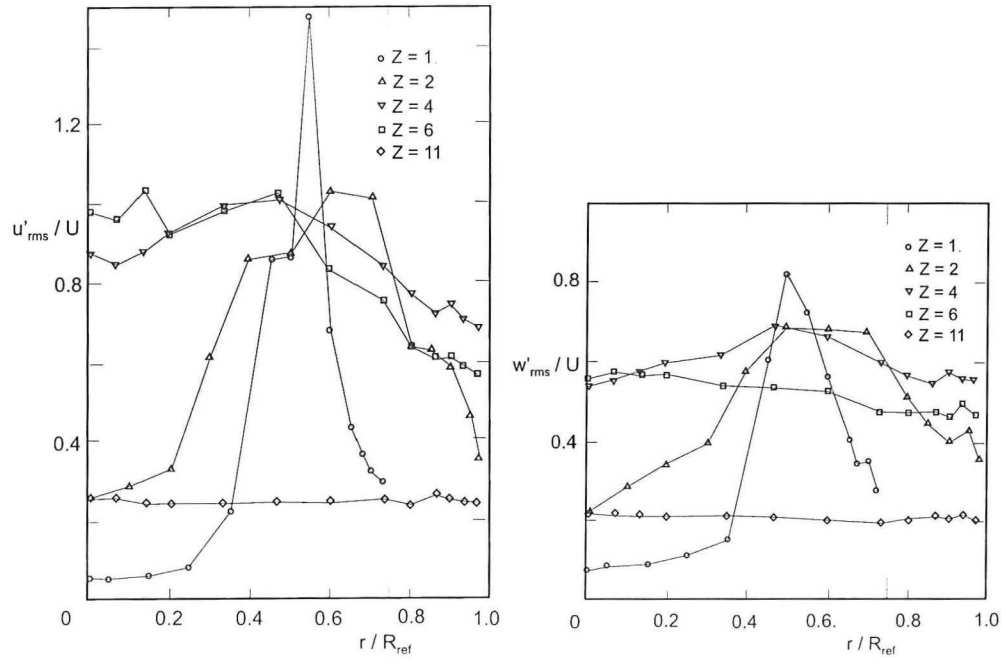

(a) Profiles of $u'_{r.m.s.}$

(b) Profiles of $w'_{r.m.s.}$

Figure 3.24: Profiles of turbulence velocity components at different axial locations: Z = 1, 2, 4, 6 and 11, Re = 15,000. After [Deshpande and Giddens, 1980]

The data presented in the article of Deshpande show that the length of the circulation region is almost constant with the Reynolds number over the range studied (5,000 to 15,000). In fact, there is a slight tendency for this length to decrease at the higher Reynolds numbers. This is different from the behavior reported by Clark (1976) using flow visualization. One of the reasons for this discrepancy is the somewhat different geometries, though the more likely explanation depends on the method for detecting reattachment (dye injection method depending upon visual inspection versus LDA).

In Deshpande, the energy spectra of the different stations is depicted. Upstream of the contraction, at Z = -4, the flow seems to be fully developed. The measured data equals the hot wire measurements of Resch (1970) in fully developed turbulent pipe flow, except for the higher frequency segment, where noise and ambiguity become apparent in the LDA results. Measurements taken at different positions from the wall are almost identical, the same holds for the measurements in the throat. Close to the centerline of the throat, a peak occurs in the spectrum at approximately 4 Hz. One diameter downstream, this peak occurs as well only at the centerline, though the points of the measurements at different positions from the wall at this station do not equal each other in this extremely turbulent region as was the case for measurements at Z = -4 and in the throat.

At Z = 4, close to the reattachment point, the radial spectra are again similar to each other, although they are not similar to turbulent pipe flow. The normalized spectrum lies below the one of turbulent pipe flow. Further downstream, the spectra equal the spectrum of turbulent pipe flow, though only for the lower frequencies. After 50 Hz, the spectra of Z = 6 and 11 are situated above the turbulent pipe flow spectrum, both having a less steeper slope than this curve.

Chapter 4

LDA

In this chapter a brief overview of the LDA principles will be given, which will handle the Doppler effect, several configurations, the fringe model, frequency shifting and tracer particles. A more extensive overview is given in Nievaart [Nievaart, 2000], while a more detailed description can be found in Drain [Drain, 1980], Durst [Durst et al., 1976] and Absil [Absil, 1995]

LDA, an abbreviation of Laser Doppler Anemometry, is a technique to measure the velocity of a flow field. Other measuring techniques are e.g. Particle Image Velocity (PIV) or Hot Wire Anemometry (HWA). The reason why LDA is so popular is that it is a non-intrusive technique, so it does not influence the flow. Besides this non-intrusive behavior, many other advantages can be given like:

- possibility to measure negative velocities
- able to measure a wide range of velocities
- measuring different separated velocity components at the same time
- continuous measurements (examine time series, apply statistics)

Of course, disadvantages occur as well, like the need for tracer particles, long data series and a transparent flow.

4.1 Doppler effect

The basic idea of LDA depends on the Doppler effect, which is known as a frequency change due to the motion of the source or receiver of a sound for example. Everybody is familiar with this Doppler shift, think about a passing ambulance. The emitted pitch of the ambulance does not change, while when it is approaching the pitch will be higher and it will be lower as the ambulance recedes. The explanation is that the perceived wavelength changes, as illustrated in figure (4.1). The change in this observed wavelength $\Delta\lambda$ is proportional to the velocity along the line source - receiver, in this case u_x:

$$\Delta\lambda = u_x \frac{\lambda}{c} = \frac{u_x}{f_{source}} \tag{4.1}$$

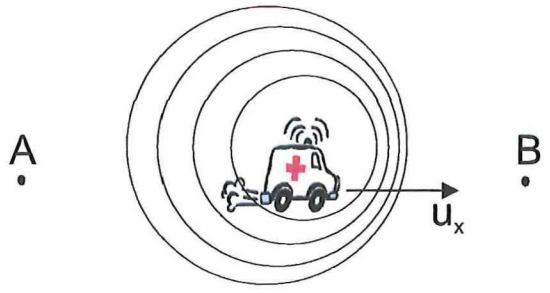

Figure 4.1: Passing ambulance: an observer at position A perceives a lower frequency than an observer at position B, due to a change in the perceived wavelengths

Where f_{source} is the emitted frequency of a source and c the velocity of sound. This equation can be transformed to give the change in the perceived frequency, thus by knowing the emitted frequency and measuring the received frequency, the velocity of the source can be calculated. This approach is also valid for light, as for instance can be seen in the red shift of receding stars.

Instead of a passing ambulance, in a flow small light scattering particles are added to measure its properties. So in reality, technically speaking in case of LDA, there are two Doppler shifts. The first is from source to particle, while the second is from particle to observer. More information about this approach can be found in the literature mentioned above.

However, applying the Doppler effect for light directly will lead to technical problems. The frequency of light is of the order of 10^{14} Hz. The Doppler shift (about 100 MHz), is very small compared to that frequency, as the velocity of a moving particle is much smaller than the velocity of light. This means that the ratio of the shift and the frequency of the source is about 10^{-6}. This is far beyond the capabilities of the highest resolution optical spectrometers. Yeh and Cummins (1964) were the first to overcome this problem [Nievaart, 2000]. The basic concept is mixing two light waves in a non-linear device like a detector which will produce a beat frequency low enough to be further processed by conventional electronic circuitry.

4.2 Configurations

Basically, two different LDA set-ups are applied. The first one is known as the reference beam LDA technique. One of the beams is used as reference beam and is directed into a light sensor, while a second beam intersects with the reference beam. This second beam usually has a higher intensity and it is not aimed at the light sensor, as is shown in figure 4.2. As soon as a particle crosses the intersection, light of the second beam will be scattered in all directions, including the direction of the detector. Because the angle between the reference beam and the scattering intersection beam is small (compared to the angle of the scattered light of other particles in the path of the intersection beam and the reference beam), the detector is able to measure and distinguish the scattered light. From the beat frequency in this superposition of light of the reference beam and scattered intersection beam, the velocity of the particle can be determined.

The second technique is the dual beam LDA, where the scattered light from the particles is received and measured at a different position than the path of one of the laser beams, for instance in the middle of the two laser beams as is illustrated in figure 4.3. The two beams should have identical wavelengths as well as intensities. This is generally achieved by splitting a laser beam in two parallel beams, which will intersect at the focus of a convex lens.

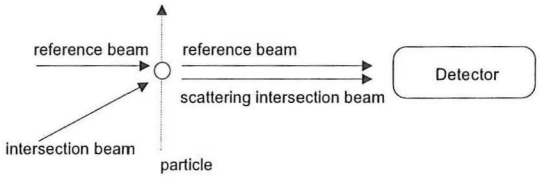

Figure 4.2: Reference beam LDA mode

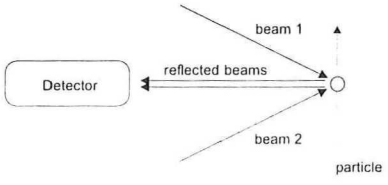

Figure 4.3: Dual beam LDA mode

The advantage of reference beam LDA is the much higher data rate. As the impurities of the fluid are often sufficient, there's also a possibility to measure without tracer particles. Unfortunately, the set-up of this method is very labour-intensive for the alignment of the two intersecting beams and light sensor. Moreover, an undisturbed laser path on both ends of the measurement point has to be available.

Therefore, the dual beam LDA is often preferred, despite its lower data rate. Dual beam LDA can be applied in different configurations: backward scattering, where the detector is positioned at the same side as where the light is coming from, forward scattering (detecting at the other side) and side scattering. Whereas forward scattering offers the highest data rate and side scattering measurements with less noise, due to (again) the labour-intensive alignments of these two configurations, the backward scatter mode is most often applied. Moving the probe to another coordinate doesn't shift the relative position of the lasers beams and light sensor, which is very practical. Therefore it is possible to start a new measurement instantly. For traverses of flow fields, this advantage counterbalances the lower date rate and the use of tracer particles amply.

4.3 Fringe model

To explain the principle of LDA, the fringe model will be applied. Although it's only an approximation of the actual theory behind LDA, the basic idea can be clarified. As described before, LDA makes use of two intersecting laser beams. This is usually achieved by dividing one laser beam in two parallel beams. These two beams pass the same lens to form an intersection. In the intersection volume of two coherent beams an interference pattern will form. The waves will amplify when they are in phase, and will extinguish when in anti-phase. This results in a pattern with parallel light and dark bands, called fringes.The interference pattern is shown in figure 4.4. The distance between two light (or dark) fringes is called the fringe spacing d_f and this can be calculated by:

$$d_f = \frac{\lambda}{2\sin(\frac{\theta}{2})}, \tag{4.2}$$

where λ is the wavelength of the light of the laser and θ the angle between the two laser beams. This angle can be calculated from the distance of the beams at the lens, d_{lens}, and the focal length

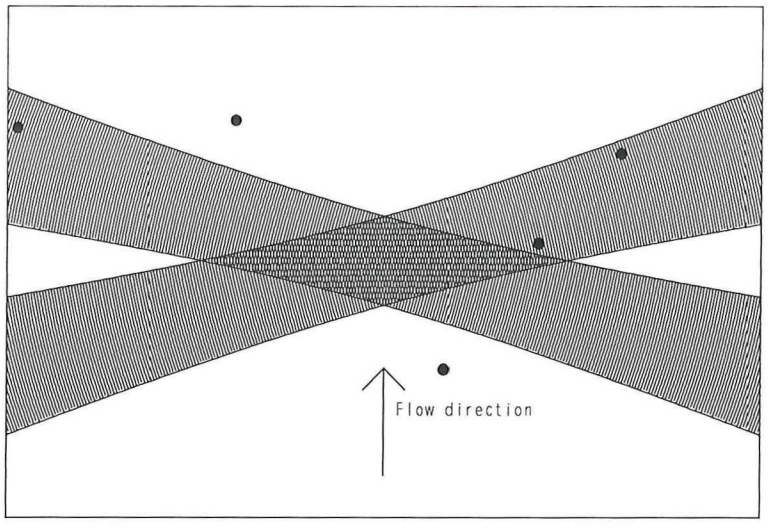

Figure 4.4: Interference pattern of two intersecting laser beams, after [Van Maanen, 1999]

F of the used lens:

$$\tan(\theta) = \frac{d_{lens}}{2F} \tag{4.3}$$

Small particles crossing the interference pattern will alternatively travel through a light or dark region, scattering a lot of light while in a light band and less light while in a dark fringe. The laser beams have a maximum intensity in the middle and fading intensities towards the edges of the beam. Superposed with the fluctuations owing to the travelling of particles through the fringe pattern, the signal of a Doppler burst for a particle travelling through the middle of the pattern will look like that of figure 4.5 in which a Doppler burst is depicted.

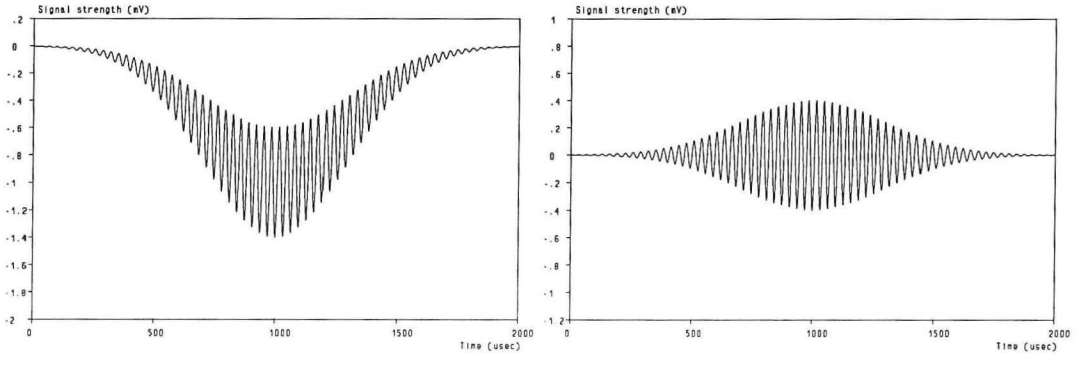

(a) Measured burst from photomultiplier

(b) Burst after removal of the 'DC' component, showing only the fluctuations owing to the travelling of particles

Figure 4.5: Example of measuring a burst, after [Van Maanen, 1999]

The higher the velocity of the particles, the shorter the time which they spend in the interference pattern and the higher the frequency of the fluctuations. The frequency of the burst, f_{burst}, is

calculated from the velocity of the particle and the fringe spacing:

$$f_{burst} = \frac{u_x}{d_f} = u_x\left(\frac{2\sin(\frac{\theta}{2})}{\lambda}\right) \tag{4.4}$$

Note that only the velocity component perpendicular to the fringes (in this case u_x) is calculated! Velocity components along the two other directions can not be calculated as the particles will only intersect one fringe maximum. Besides this, motions perpendicular to the plane of the laser beams will cause no Doppler effect. To measure other components more pairs of laser beams should be used.

4.4 Directional discrimination

By measuring the burst frequency and using equation (4.4), the velocity can be calculated. Only, a particle crossing in the opposite direction with the same speed will produce exactly the same signal and so an identical velocity! No directional discrimination can thus be made. To get rid of this problem, the frequency of one of the beams will be shifted. The resulting frequency difference f_d after applying this frequency shift f_{shift} yields:

$$f_d = f_{shift} + f_{burst} \tag{4.5}$$

A zero velocity is now represented with a fluctuating burst with f_{shift}. Negative velocities will generate frequencies below f_{shift}, while positive velocities will give higher frequencies. This is illustrated in figure 4.6.

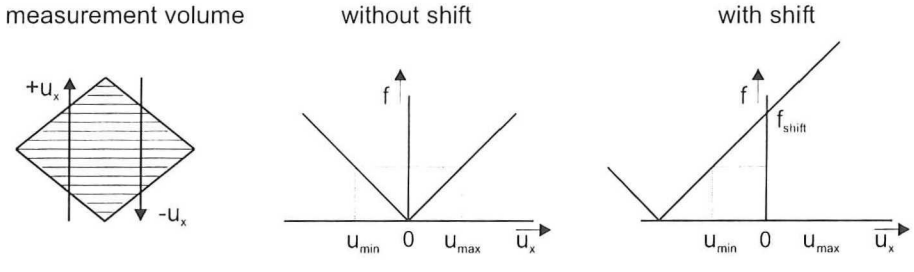

Figure 4.6: Negative velocity discrimination due to frequency shifting, after [Absil, 1995]

Using the fringe model (figure 4.4), the interference pattern seems to be moving, due to the frequency shift. Seen from the lens, the fringes move from the shifted to the unshifted beam, i.e. from a higher to a lower frequency. In case of a stagnant particle, the fringes cross the particle instead of the particle crosses the fringes, but still a fluctuating burst will be generated.

To measure negative velocities, a general rule is to select a shift that is twice the Doppler frequency corresponding to the maximum negative velocity. Another way to measure negative velocities is to force the Doppler frequency into a preferable frequency range for filtering or signal processing reasons. In practice, frequency shifting is often arranged by making use of a Bragg cell. This implies a typical frequency shift of 40 MHz.

4.5 Scattering volume

The intersection volume of the two laser beams is also called the scattering volume. This volume is defined to have a ellipsoidal shape for Gaussian beams, and is depicted in figure 4.7. In this figure, two scattering volume parameters are shown. They are defined as:

diameter of the volume d_m:

$$d_m = \frac{d_{e^{-2}}}{\cos(\frac{\theta}{2})} \tag{4.6}$$

length of the volume l_m:

$$l_m = \frac{d_{e^{-2}}}{\sin(\frac{\theta}{2})} \tag{4.7}$$

In these formulas θ denotes the angle between the two laser beams while $d_{e^{-2}}$ is the waist diameter of the focused beams. This diameter is related to the original diameter of the laser beams $D_{e^{-2}}$, the diameter where the intensity drops with e^{-2} times the value at the center of the beam, according to:

$$d_{e^{-2}} \approx \sqrt{\frac{n_w}{n_a}} \frac{4F\lambda}{\pi D_{e^{-2}}} \tag{4.8}$$

in which an magnification factor due to the refraction indices of water (n_w) and air (n_a) is included. By increasing the input waist and decreasing the focal length, a smaller scattering volume will be obtained, which will result in a better estimate of the arrival time ([Van Maanen, 1999]) and more localized experiments.

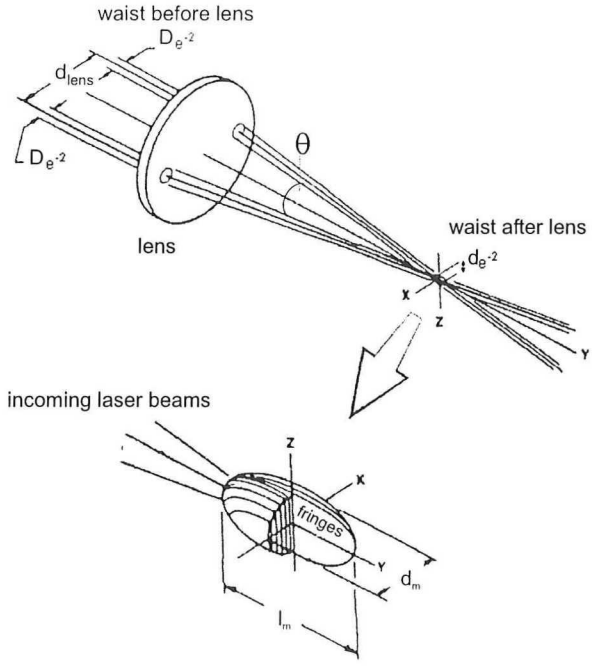

Figure 4.7: Construction of the measurement volume and definition of the its parameters, after [TSI, 1990]

Combining the diameter of equation (4.6) with the fringe model, the number of fringes in the volume, N_{fr} is determined by:

$$N_{fr} = \frac{d_m}{d_f}, \tag{4.9}$$

though it is more interesting to know the number of fringes a moving particle will encounter. According to van Maanen ([Van Maanen, 2000]) the number of cycles N_{burst} in a Doppler burst equals:

$$N_{burst} = T_{tt}\left(\frac{u_x + f_{shift}d_f}{d_f}\right) \tag{4.10}$$

In which, for this case, the velocity in the x-direction has been taken. T_{tt} is the transit time, the time it takes a particle to travel through the measuring volume.

For a pipe flow, the velocity components in the y- and z-direction are rather small compared to u_x. Therefore the modulus of the velocity vector approximates u_x. Knowing this velocity and the sizes of the scattering volume, the shift frequency in order to get a certain amount of fringes can be determined by:

$$N_{min} = \frac{d_m(u_x + f_{shift}d_f)}{d_f u_x} \tag{4.11}$$

Where N_{min} is the minimal amount of fringes. In practise, this equals often 8.

4.6 Tracer particles

As mentioned above, dual beam LDA needs added tracer particles in the fluid to work properly. These tracer particles are also known as seeding. The particles should satisfy the main requirements for seeding:

- the particles must be able to follow the flow correctly, so their density should equal that of the fluid and the particles should be small;
- the particles must have good light scattering properties to all directions, such as a different index of refraction than the fluid;
- the particles should be cheap and inert;
- the particles should be conveniently generated and at a sufficient rate;
- the particles have to be small enough to cross one fringe at a time (ideally, smaller than one fringe).

The bigger a particle is, the more light will be reflected. The problem that arises when particles are larger than the fringe spacing is that they cross a couple of fringes at the same time which result in a less fluctuating signal. The less fluctuating the signal is, the less visible the particle is. The size of the particle should therefore be small, preferably just smaller than the fringe spacing, though not too small, because this leads to low intensities and a noisy signal. This problem is illustrated in figure 4.8. Usually, choosing the size of the tracer particles goes by trial and error.

Using hollow glass spheres with a diameter around ten micrometers satisfies the conditions mentioned above. The glass spheres are in powder form (very small), have the same density of water owing to a hollow core and they reflect light due to the glass surface.

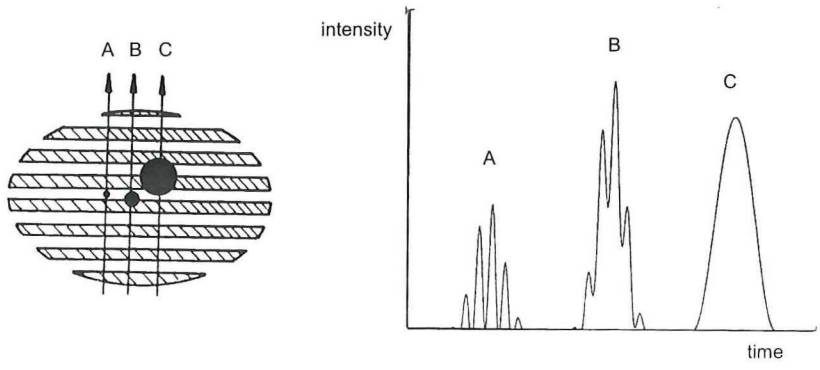

Figure 4.8: Signal quality depends on the particle size, after [Absil, 1995]

4.7 Random sampling

As LDA gives a velocity signal which is not continuous as with e.g. HWA, the velocity information arrives randomly when a tracer particle traverses the measurement volume. The time between data (TBD) is defined as the time between two successive measurements. The distribution, like many random processes in nature, can be characterized by a Poisson distribution. Consider the particles are random, though homogeneously distributed across the flow and that their velocity within the volume is constant. The exponential distribution for the time between data is then given by:

$$P_{poisson}(T_{TBD}) = \frac{1}{T_{TBD,A}} e^{-\frac{T_{TBD}}{T_{TBD,A}}} \tag{4.12}$$

In which $P_{poisson}$ is the probability, T_{TBD} the time between data, where is $T_{TBD,A}$ the mean value of it. The reciprocal value of this average equals the mean data rate. The probability is exponential, which implies that the highest probability that a Doppler signal will occur is immediately after the previous one.

To deal with these randomly sampled data (instead of periodically sampled data), interpolation techniques have to be applied for time signal reconstruction ([Van Maanen, 1999]). For this reason the data rate should be at least 2π times the highest frequency of the turbulent velocity fluctuations of interest. This demand does not count for determining statistical properties like the mean value, although high data rates are useful.

Chapter 5

Set-up of the flow loop and LDA system

The LDA measurements were done in a large set-up containing the venturi tube. This set-up, as well as some details of the flow loop and the control of the pump can be found in section 5.1. After this, the set-up of the LDA equipment will be clarified in section 5.2.

5.1 Flow loop

First, attention will be paid to the major part of the set-up, the venturi tube. Besides giving the dimensions of this part of the set-up, some inevitable modifications to be able to do LDA measurements will be explained. After this, the measurement section will be illuminated. Finally, the assimilation implementation of the measurement section in a flow loop will be given.

5.1.1 Venturi

Out of a massive perspex cylinder, an ISO model 5167 short form venturi tube is cut. The dimensions of this venturi are shown in figure 5.1. A venturi consists of a contraction (inlet), a throat and a diffuser (outlet). As can be seen, a part of the throat has been removed and replaced by a thin transparent sheet, as a 'thick' wall distorts the incoming laser beams in such a way that the measured component is inaccurate. This sheet is taped at the borders to prevent it sweeping away by the flow and fits into a special grinded edge of 0.1 mm. The sheet has a thickness of 0.25 mm, does not attract dirt and is stiff enough to avoid vibrations which could affect the measurements. To prevent a thick wall in the outlet measurement location, a large window section has been cut out and replaced by the foil as well.

As the surfaces of the measuring locations are not flat, but curved, a second problem arises while doing measurements with laser beams. The two beams in a horizontal plane used to measure the axial velocity component do not suffer from this problem, but the two beams in a vertical plane used to achieve the tangential component will focus too close to the wall, see figure 5.2. Therefore, simultaneous measurements of both velocity components are not possible. This problem is easily solved by placing a perspex box around the throat of the venturi, a flat plate in front of the large

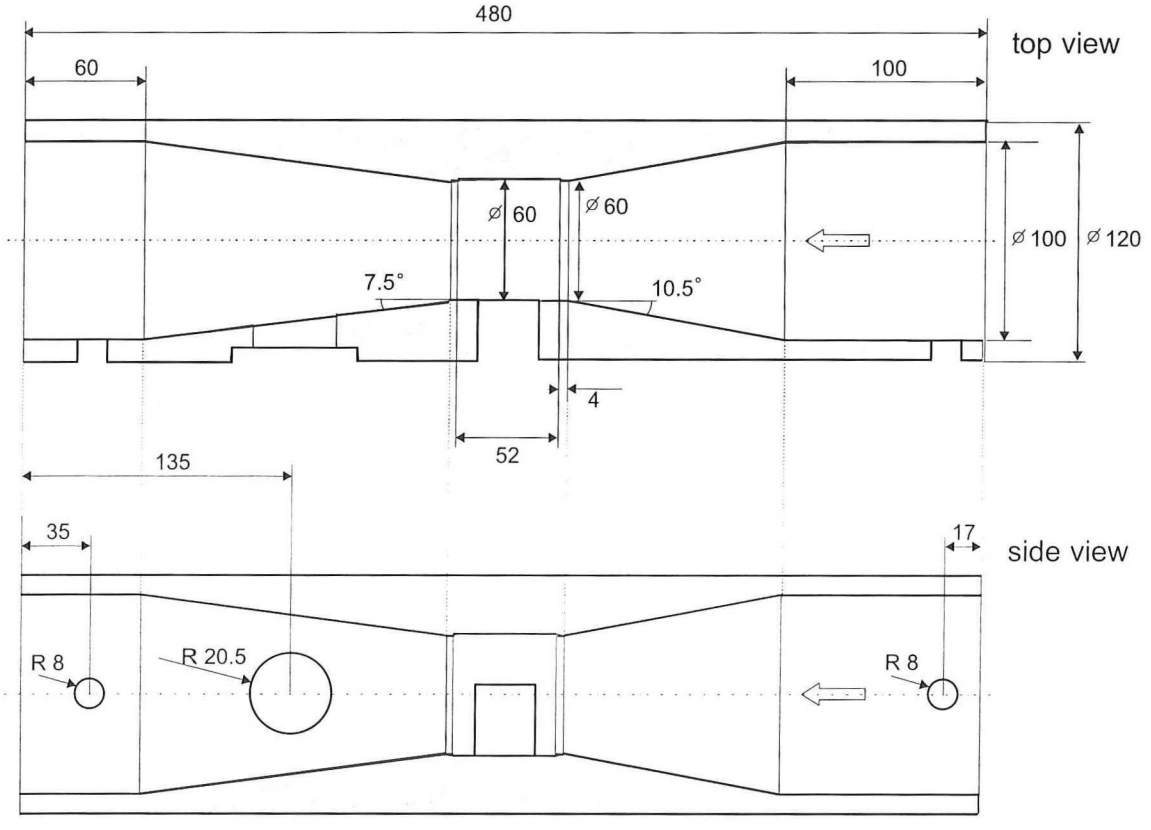

Figure 5.1: The venturi and its dimensions (in mm). Note that the flow is from right to left

measuring window and mounting glass 'screws' with a flat surface as 'windows' in the measurement pipe. Figure 5.3 shows the outlet of the venturi, together with these three solutions. The volume between the flat plate of the large measuring window and the foil, as well as the perspex box, are filled with water for refraction reasons.

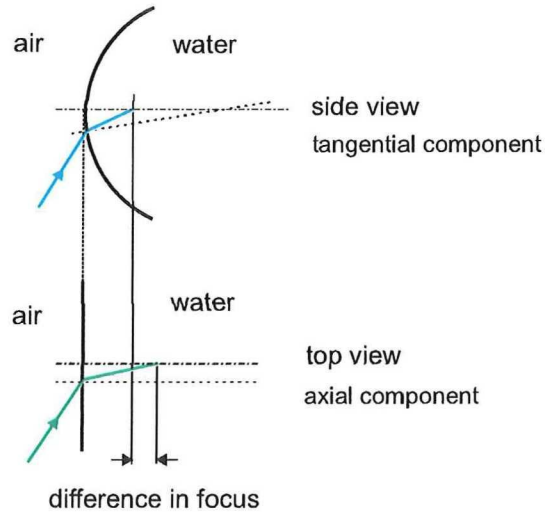

Figure 5.2: Schematic representation of the two laser beam pairs used to measure two components of a flow field in a tube. The curved surface for one of the two pairs leads to a difference between the positions of the two focusses

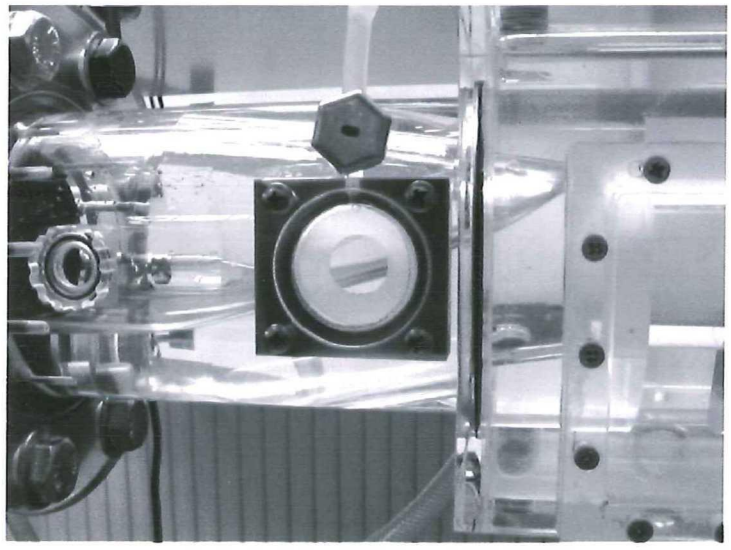

Figure 5.3: Outlet of the venturi with, from left to right, three solutions to carry out simultaneous measurements of the two velocity components: glass 'screw', flat plate in front of the large measuring window and a part of the perspex box around the throat of the venturi. The flow is from right to left.

Owing to Bernoulli's law, the higher mean velocity in the throat of the venturi leads to a lower pressure in that region. Due to this under pressure in the throat, the foil will be sucked into the flow. A lower pressure in the box relative to the pressure in the throat is arranged by using a vacuum pump connected to the perspex box. This will cause both the sheets, as the large window section is connected to the perspex box, to be pressed against the edges of the venturi. The way the venturi is positioned in the measurement section can be found in the following paragraph.

5.1.2 Measurement section

The measurement section consists of the venturi and a part of a pipe upstream and downstream of the venturi. The measurement locations in the pipes are equipped with the flat, glass 'screws' as well. As can be seen in figure 5.4, a lot of hoses are applied to monitor the pressure at several locations. Furthermore, a hose connects the water filled perspex box to a vacuum pump via an U-trap.

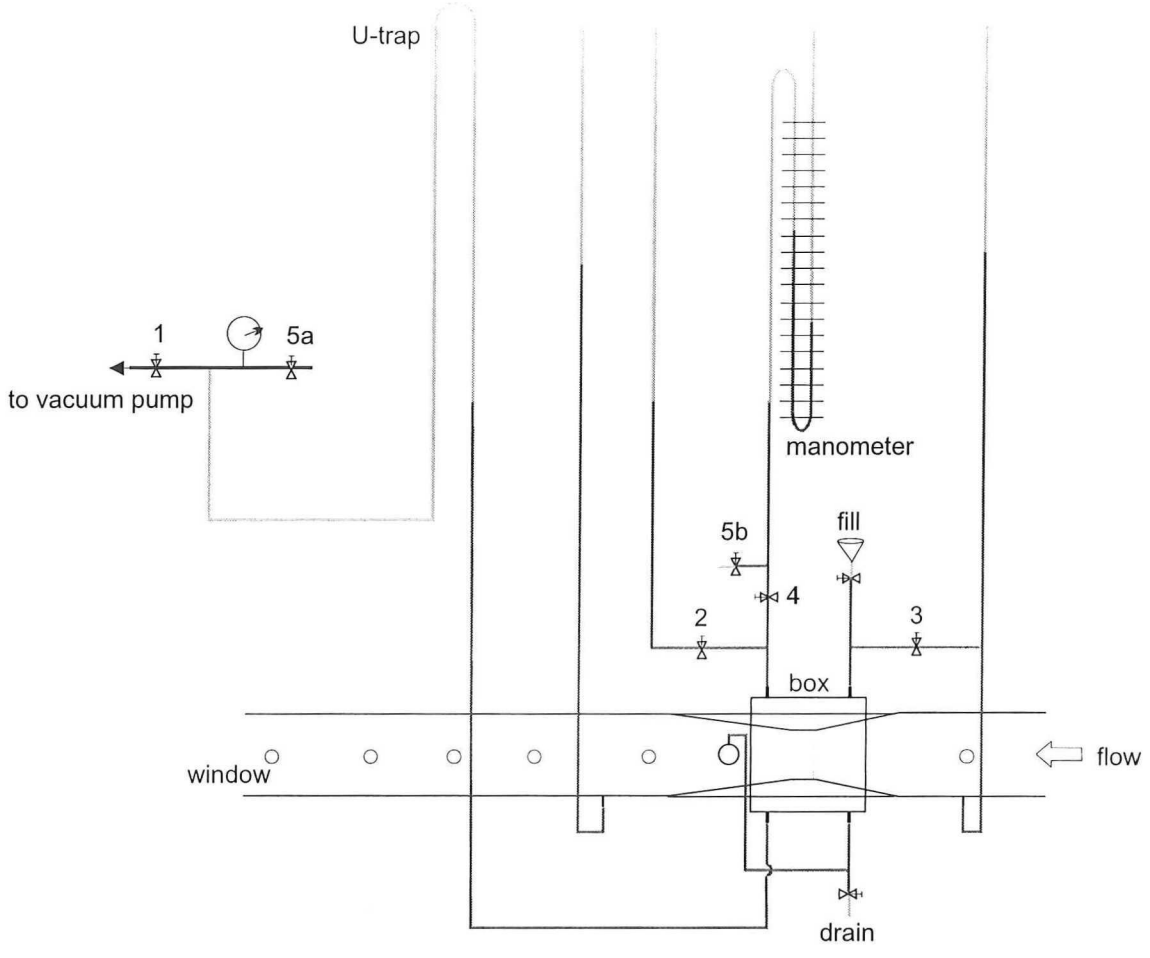

Figure 5.4: Measurement section in more detail, including the hoses connected to this part of the set-up

The perspex box, a cube of which each side has a length of 140 mm, around the venturi is linked to the upstream pipe flow by valve 3 to equalize the pressure in the box. This is necessary as long as there is no flow, as valve 2 in figure 5.5 is closed at that time. Besides this, valve 3 is also used to fill the box. To prevent water flowing in the manometer, valve 4 should be closed in that case as well. As soon as there is a flow through the venturi, valves 2 and 3 (in figure 5.4) should be closed. The manometer can be used now (open valve 4). To enforce a low pressure in the box, the vacuum pump has to be switched on. Closing valve 1, the pressure in the box remains at the established pressure. This can be monitored via the manometer.

5.1.3 Total flow loop

The single phase flow measurements in and close to the venturi are performed in the set-up of figure 5.5. The upper pipe has a diameter of 15 cm, while after some bends the diameter is decreased to 10 cm. In this lower pipe, the measurement section is positioned. A description of the several devices is given below:

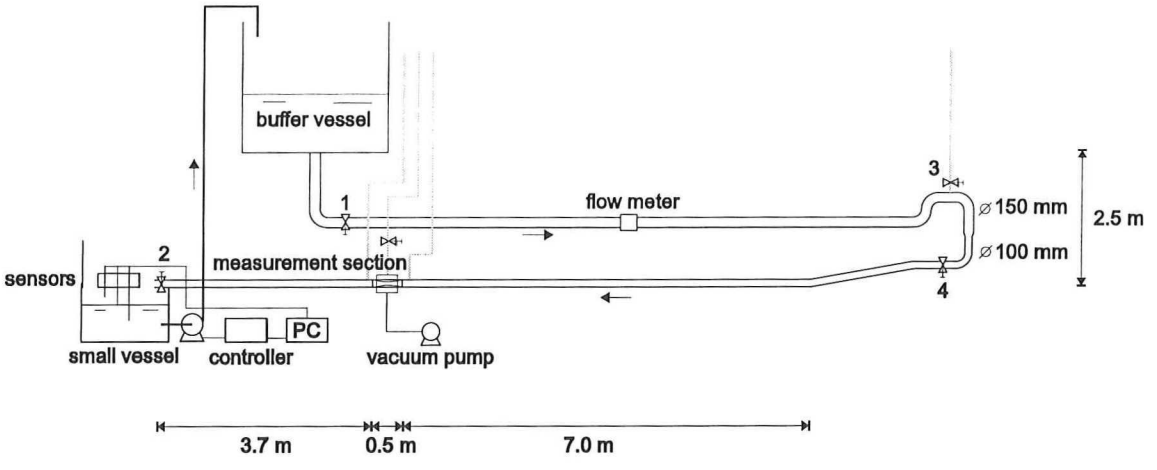

Figure 5.5: Experimental set-up of the loop used for the turbulent flow measurements

Buffer vessel:
A large stainless steel vessel with a diameter of 2.5 m is filled with approximately 4,700 liters of water. This vessel damps oscillations and avoids trapping of air bubbles, but most of all it takes care of the 'natural', gravity driven flow of the system. A constant water level in the vessel causes a constant velocity of the water flow.

Flow meter:
The flow through the upper pipe is measured with the Krone Altoflux Altometer K300 DN150, a magnetic flow-metering device.

Measurement pipe:
The measurement pipe is made of a transparent material and has a diameter of 100 mm. In this pipe, the venturi is mounted. Between the last bend and the venturi, an entrance length of 70 diameters is applied to obtain a fully developed turbulent pipe flow upstream of the venturi. This is considerably longer than an entrance length of 40 diameters, approved by Nikuradse.

Measurement section:
This section in the measurement pipe contains the venturi in a perspex box, as well as several measuring windows from one diameter upstream to 5 diameters downstream. The box around the throat of the venturi is connected to a vacuum pump.

Vacuum pump:
An adjustable pump with a maximum capacity of 1,200 l/min is used to obtain a pressure in the perspex box just below the pressure of the water in the throat of the venturi.

Small vessel:
The smaller vessel with a diameter of 1.5 m acts like a reservoir for the flow, containing about 650 liters of water. The level of the fluid is regulated by three sensors, a computer, a controller and a

pump to achieve an almost constant water level in this vessel. Due to the larger diameter of the buffer vessel, the variation in water level in that vessel is only 36% of the variation in the lower, smaller vessel.

pump, controller and PC:
An adjustable pump of Sterling Fluid Systems with a maximum capacity of 1,450 l/min corresponding to 50 Hz of the motor, is controlled by a computer which reads the signals of the sensors in the small vessel. Via the controller (Commander SE) the PC communicates with the pump.

Valves:
Valves 1 and 2 are used to stop the flow as long as the set-up is not in use. Valve 3 can be used to remove trapped air bubbles. The flow rate is controlled by valve 4.

5.1.4 Regulation of the pump and water level

In order to maintain a constant water level in the large buffer vessel, in the small vessel three sensors are mounted at different levels. Each sensor can detect whether the water level is under or above its own level by means of a float. A program in C is written to control a PC (`pomp.c`, see listing on CD-ROM). The PC reads the three signals every second and decides in which region the water level can be located. Depending on this region and the given flow rate range, the value of the required power of the pump is sent to the controller, which is connected to the pump. In this way the water level remains between the height of sensor A and B (see figure 5.6). Besides regulation of the water level, with the program the user can switch off the pump, make the pump do its work with maximum power or switch to manual operation. The height between sensor A and B is 40 mm, while the height between B and C is 50 mm.

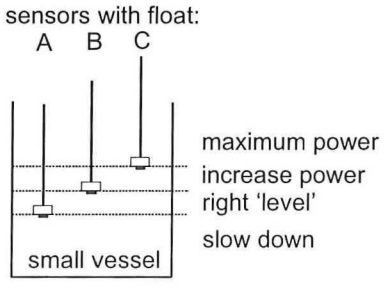

Figure 5.6: Small vessel with the three sensors with floats and the four regions of the water level

5.2 LDA set-up

All the LDA related equipment used during the experiments is sketched in figure 5.7. It consist of the following components:

Laser: A water cooled Argon-Ion laser, Stabilite 2016 from Spectra-Physics, is used. It delivers up to 5 W of all-lines Argon power and $>$ 100 mW of TEM_{00} single-line powers from most of the visible Argon lines between 454.5 nm and 514.5 nm. The coherence length is about 4 cm.

ColorBurst: The TSI model 9201 ColorBurst Multicolour Beam Separator converts the Argon-Ion laser output into three pairs of beams: two green beams of 514.5 nm, two blue ones of 488.0

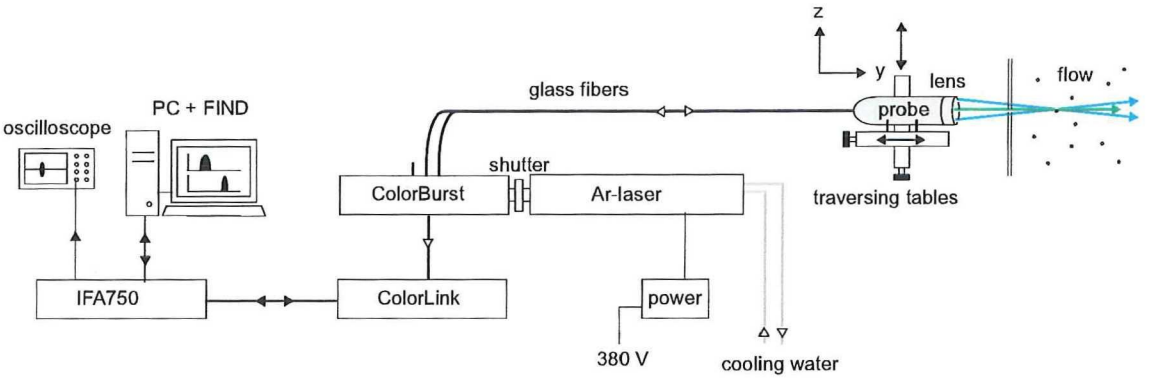

Figure 5.7: The set-up of the equipment used for the LDA measurements

nm and two violet ones of 476.5 nm. In every pair, one of the beams is optically shifted over 40 MHz. The shifting is done by an acousto-optic modulator (Bragg cell) located in the ColorBurst, which is driven by a 40 MHz signal generated in the ColorLink. The beams can be switched off separately, by which the desired beams can be chosen.

Probe: The probe contains both the emitting and receiving optics and is connected to the ColorBurst and ColorLink by glass fibers. TSI model 9832 is a 83 mm diameter probe for emitting and measuring simultaneously with two laser pairs (green and blue). The laser pairs are emitted perpendicularly, and so two perpendicular velocity components can be measured. The laser beams of one of the pairs, as they come out of the probe, are spaced by 50 mm and have a $D_{e^{-2}}$ of 3 mm. The lens is mounted on the probe. Table 5.1 shows the scattering volume characteristics for the applied lenses with focal lengths of 122.2 mm and 250 mm. These values, $\theta/2$, $d_{e^{-2}}$, d_m, l_m and d_f, are calculated with formulas 4.3, 4.8, 4.6, 4.7 and 4.2, respectively.

Table 5.1: Characteristics of the scattering volume for the two used lenses

Focal length (mm)	λ (nm)	$\theta/2$ (°)	$d_{e^{-2}}$ (μm)	d_m (μm)	l_m (mm)	d_f (μm)
250.0	514.5	5.71	63.0	63.3	0.63	2.58
250.0	488.0	5.71	59.8	60.1	0.60	2.45
122.2	514.5	11.56	30.8	31.5	0.15	1.28
122.2	488.0	11.56	29.2	29.8	0.15	1.21

ColorLink: The TSI model 9230 ColorLink Multicolour receiver processes the light, received by the probe. It separates the light by wavelength and converts it to an electrical signal in the photo multiplier. After that, a frequency mixer adds the selected frequency shift electronically. Finally an analogue output is send to the signal processor.

IFA750: The TSI Intelligent Flow Analyzer (IFA) 750 is the signal processor in the LDA set-up, and detects bursts simultaneously for three channels or components of the velocity. The user can set the criteria, after which the IFA collects and stores the validated bursts. A more elaborate description of the IFA750 can be found in Nievaart [Nievaart, 2000] or in the IFA750 manual [TSI, 1992]. The IFA750 and the ColorLink can be computer controlled with the program `FIND`.

Oscilloscope: The analogue output from the ColorLink can be monitored on an oscilloscope to check the shape of the bursts, the signal to noise ratio and the number of crossed fringes per bursts for different settings. A Yokogawa DL2220 400MS/s digital oscilloscope is convenient in this case, because it can bring the bursts to a 'stop' to check their properties.

Traversing system: The probe is mounted on a traversable table which gives the possibility for 2-D movements. The axes could be set up in the desired spatial orientation to measure the predefined planes or cross sections of the flow field. According to figure 5.7, the probe can be moved in the y,z directions using adjusting wheels. The wheels are stepped and the smallest movement is 0.01 mm.

Seeding: As seeding, hollow glass spheres of TSI, Part#900890, with an avarage diameter of 8 - 12 μm have been used.

`FIND`: Running on a PC, Flow Information Display Software (`FIND`) sends and receives information from the IFA750 and the ColorLink. The PC receives the measurement data and the status of the signal processor from the IFA750. `FIND` enables the user to save the data and look at real time generated velocity histograms. The user can send general settings to the signal processor. The remote control of the ColorLink enables the user to set preshift and photo multiplier gain easily. Although `FIND` contains many features to process recorded data like statistics and probability distribution functions, the data are processed with own programs (as `FIND` acts like a 'black box'). `Dumpfind`, a program made by Jaap Beekman, extracts information like arrival time, time between data, transit time and the velocity from the raw data files, ready to use for further calculations.

The measurements have been done with the 488.0 nm and 514.5 nm laser beams for the tangential and axial velocity components respectively, in the dual beam back scattering mode. Therefore, only one probe was in use. To perform the measurements, lenses with focal lengths of 122.2 mm and 250 mm where utilized.

The probe is aligned in the horizontal and vertical planes with respect to the measurement section by observing the reflections of the laser beams coming from the flat surface of the transition air - perspex. The probe was adjusted so that these reflections travelled along symmetric paths with respect to the incoming beams. Furthermore, the probe was rotated about its optical axis and fixed in the position in which the mean velocity measured with the vertical laser beam pair in the center of the pipe was identically zero. An additional advantage is that a well aligned probe often gives a higher data rate. To find the location of the wall, the measuring volume is moved towards the wall by traversing the probe. When the measurement volume hits the wall (or foil), this shows up as a sudden increase in noise level of the observed signal and a increase of the data rate. This position of the traversing table is set to 0.00 mm.

The actual location of the measurement volume inside the fluid compared to the wall does not equal the displacement of the probe outside the fluid. This is due to the refraction of the laser beams on the transitions from air to perspex and from perspex to water. To solve this problem, the displacement outside the fluid has to be multiplied with a factor to find the displacement in the fluid. The expression for this factor, m_{corr}, reads:

$$m_{corr} = \frac{F}{0.5 d_{lens}} \tan\left(\arcsin\left(\frac{n_w}{n_a}\sin(\theta)\right)\right) \tag{5.1}$$

The derivation of this formula can be found in Deelder [Deelder, 2001]. Note: the properties of perspex do not influence m_{corr}, because finding the position of the wall already deals with the 'offset', due to travelling of the laser beams through perspex. Substitution of the relevant data in eq. (5.1) gives for the lenses with focal lengths of 122.2 mm and 250.0 mm a correction factor of 1.35 and 1.34, respectively. These values approximate the value of the ratio of the refraction indices of water and air (4/3). For rough estimations this value can be used.

Chapter 6

Signal processing

The raw data series obtained during the measurements contain information about the flow, as well as some properties like the fringe distance, the frequency shift and filter range, which the user of the program `FIND` can adjust. The program `Dumpfind` extracts this information to several files. One of them contains the specifications of the measurements. Furthermore, for each velocity component, a file holding vectors of among other things the velocity, transit time and the time between data is created. These files can be read into other programs to process these data files.

The properties of the velocity (like u_i and $\overline{u}$) can not be calculated in a straight way, especially when the flow is highly turbulent (with turbulence intensities of more than 30%) as velocity bias occurs. Section 6.2 handles this problem. Furthermore, sections 6.3 and 6.4 give more information about the way of determining the auto correlation function and power spectrum, respectively, as well as their properties. However, first, the data files have to be checked for erroneous behavior. This will be done with diagnostic tools, see the following section.

6.1 Diagnostic tools

In this section a short description of every diagnostic tool used and the way it works will be given. In Van Maanen [Van Maanen, 1999] a more extensive description can be found. These tests do not guarantee the data are a hundred percent reliable, though the main problems causing erroneous data will be found.

1. Velocity signal
Plotting the velocity against time is a first and simple step in evaluating the data set. This should give a picture like figure 6.1*a*. Although measurements are performed because it is unknown how the flow develops, one can still use common sense. Figure 6.1*b* shows some peaks, an indication of erroneous behavior. Following one streamline, some qualitative predictions can be made about the turbulence intensities from the way the frequency of the velocity fluctuations changes. Furthermore, the velocity signal shows flow reversals.

2. Linear velocity probability distribution
Usually, the velocity probability distribution has a more or less Gaussian shape, shifted over the average velocity of the component being measured. Most distributions are skewed, however (figure 6.2*a*). When the probability distribution deviates strongly from what one could expect under given

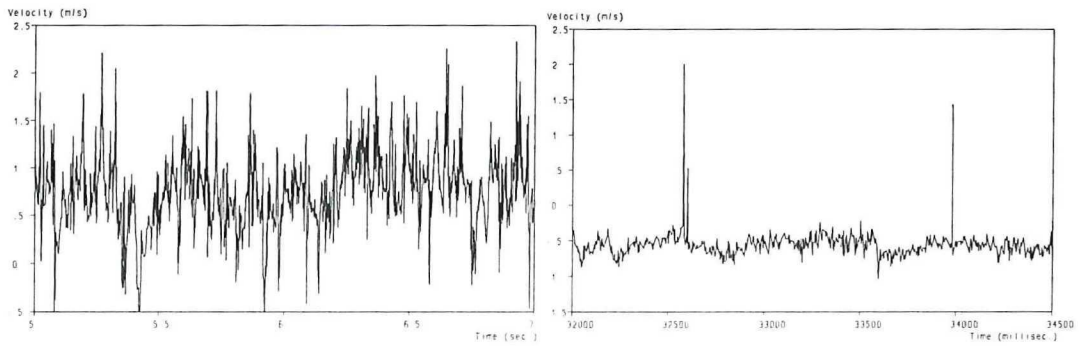

(a) Normal velocity fluctuations without multiple validation

(b) A raw velocity trace containing a few excursions

Figure 6.1: Velocity traces, from [Van Maanen, 1999]

conditions, there is a severe chance that something is wrong. An example is given in figure 6.2*b*. This figure shows a 'comb-like' structure, an indication of round off errors due to the quantization of the processor. The most probable cause is a far from optimum choice of the velocity range of the processor for the experimental conditions.

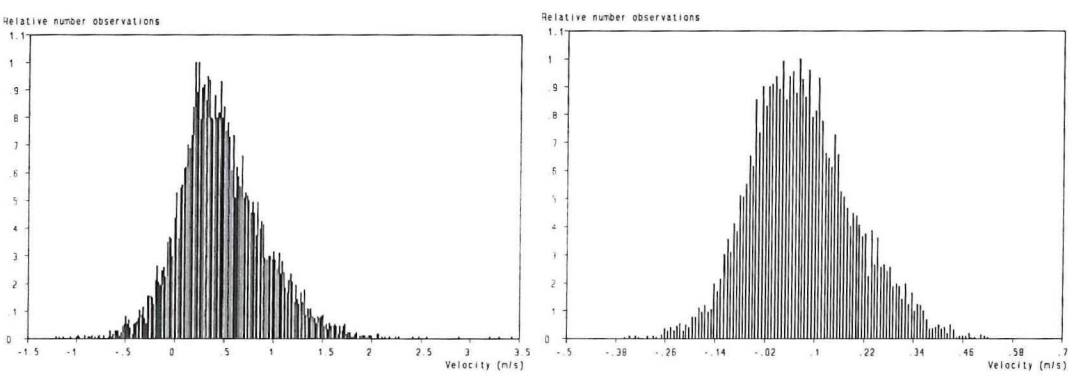

(a) Normal

(b) 'Comb-like'

Figure 6.2: Linear velocity probability distributions, from [Van Maanen, 1999]

3. Logarithmic velocity probability distribution

There is no real difference between the logarithmic and linear velocity probability distribution, only the vertical scale is made logarithmic to enhance small contributions. Figures 6.3*a* en 6.3*b* show this clearly: the small contributions which can not be seen in the linear distribution, can be easily distinguished when the vertical axis is made logarithmic. The small contributions at the higher velocities can be caused by frequency shift leakage for example.

4. Time between data histogram

As explained in section 4.7, the velocity signal is randomly sampled since the crossing of the measurement volume by a tracer particle is a random process. The resulting exponential distribution for the time between data (TBD) gives a straight line in a semi logarithmic plot. Although the distribution slightly differs, it is still a good approximation for turbulent flows. Some examples of

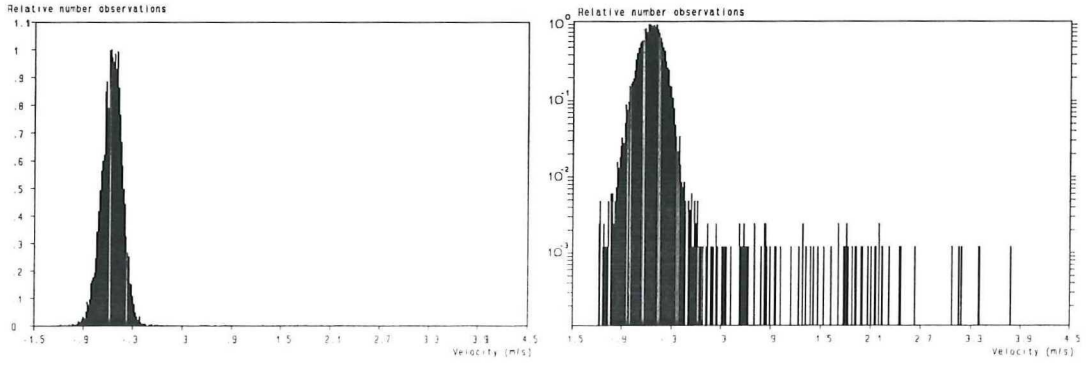

(a) Linear

(b) Logarithmic, showing small contributions

Figure 6.3: Velocity probability distributions, from [Van Maanen, 1999]

TBD-diagrams on a semi logarithmic scale are shown in figure 6.4. The first figure (*a*) reveals a straight line, in which the slope of this line gives an indication of the data rate of a well performed measurement. Figure 6.4*b* shows multiple validation in the data set: sometimes more than one tracer particle is travelling through the measuring volume causing camel-shape bursts and bias in the TBD. Figure 6.4*c* depicts the dead time of the processor, which is an indication of problems with the processing speed of the signal processor. Finally, figure 6.4*d* shows a convex shape of the TBD, this is the way how velocity bias can influence the TBD. The convex shape in this case is caused by a turbulence intensity of 30% in combination with 1-D velocity bias. The higher the turbulence intensity, the more convex the shape of the TBD-diagram will be. More information about the velocity bias can be found in section 6.2.

5. Auto correlation function

The auto correlation function (ACF) of the stochastic velocity signal $u(t)$ is introduced in section 2.6. It is possible to calculate an auto correlation function of the measured velocities. As the data are randomly sampled, a special slotted auto correlation function will be needed in order to get the best estimate. The way the ACF is calculated is called the slotting technique with local normalization. Details about this technique can be found in Van Maanen [Van Maanen, 1999]. This technique has shown to be a good approach, as long as the raw data are reliable. It is very sensitive to multiple validation as the estimated ACF becomes unpredictable. Figure 6.5*a* shows the ACF of a reliable data set: the variance around $\tau = 0$ is limited, it has a clear noise peak at the origin and the slope is declining. This is not the case in figure 6.5*b*, which has been effected by multiple validation. The large variance for all values of τ indicates that something is seriously wrong. More information about the slotting technique as well as some properties of the ACF can be found in section 6.3.

Another application of the ACF is related to the duration of the measurement. The measurement should last long enough to achieve a good accuracy. After 100 integral time scales (Γ), the average velocity and the root mean square (RMS) value of the turbulent fluctuations start to convergence reasonably well. Although these parameters have not reached their final values, a minimum of 100 Γ is applied [Van Maanen, 2000].

6. Number of products in the slotted auto correlation function

When calculating the auto correlation function using the slotting technique, in each slot a number of products is collected. This number of products in each slot, N_p is, on average, equal to:

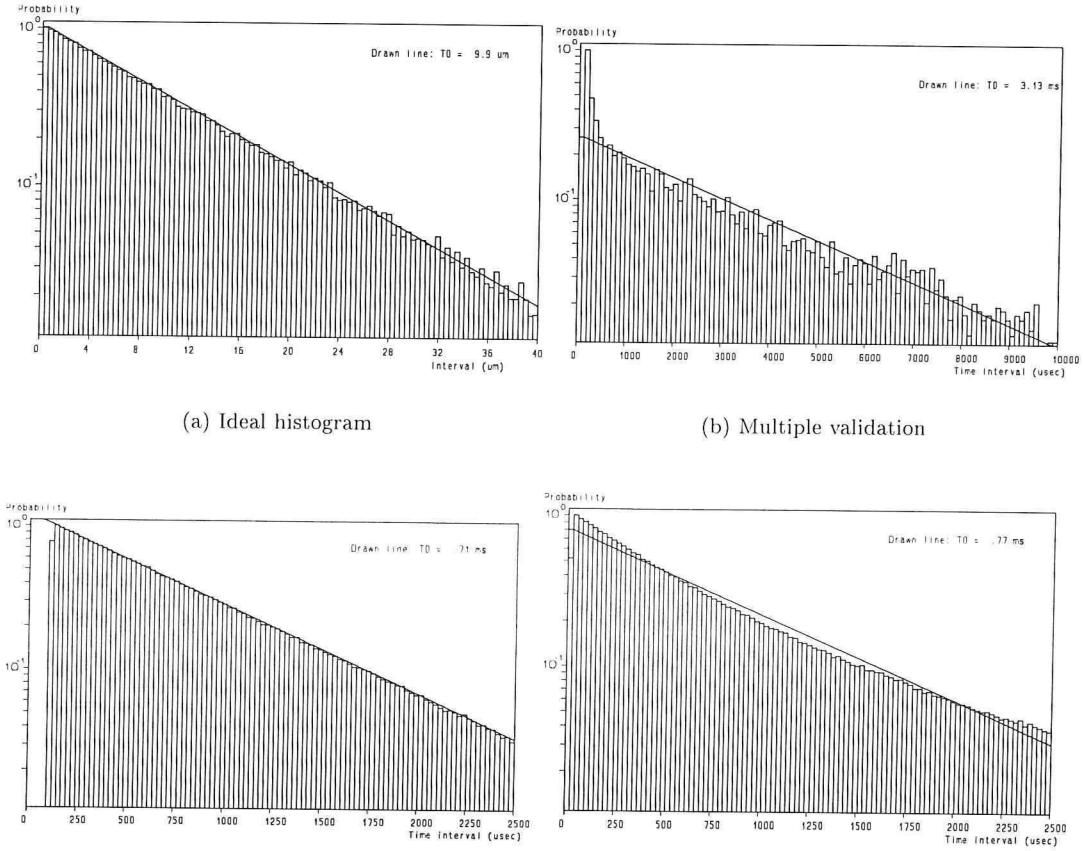

(a) Ideal histogram

(b) Multiple validation

(c) Dead time of the processor

(d) Velocity bias

Figure 6.4: Time between data histograms, from [Van Maanen, 1999]

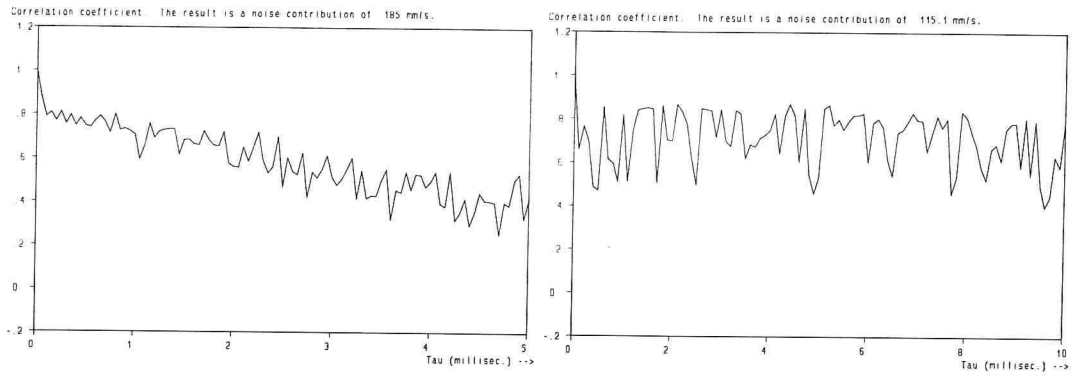

(a) Reliable data set

(b) Multiple validation

Figure 6.5: Auto correlation function with local normalization, from [Van Maanen, 1999]

$$N_p = N_t\left(\frac{\Delta t}{t_0}\right) \tag{6.1}$$

in which N_t is the total number of velocity observations, Δt is the slot width and t_0 is the characteristic time distribution (= 1 / data rate). Deviations from this average number of products indicate problems, as can be seen in figure 6.6: the low number of products in the first slots indicates a low number of observations with short TBD. The 'comb-like' structure comes from round-off errors.

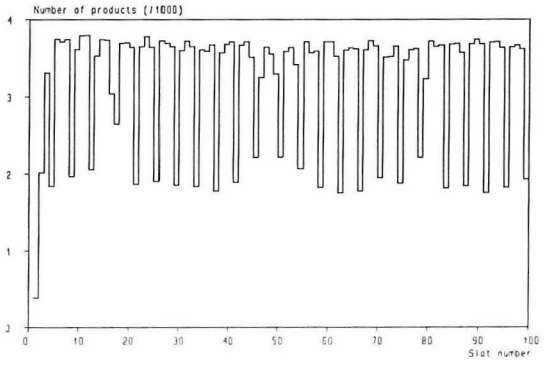

Figure 6.6: Number of products in de auto correlation coefficients which indicates problems: all bins should be filled uniformly, from [Van Maanen, 1999]

6.2 Velocity bias

Issues of biasing in mean velocity and turbulence measurements have been recognized since 1973 (McLaughlin and Tiederman) and continue to be topics of debate. Velocity bias is present for all LDA systems operating in 'burst' mode, meaning that each particle causes a measurement. Assuming the particles are uniformly distributed in the fluid, the likelihood of a particle passing through the measurement volume is proportional to the fluid velocity. Accordingly, the time between velocity samples is not equidistant. The arithmetical average of sampled velocities is higher than the velocity based on equidistant time intervals. This shift towards the high value is known as velocity bias. Not only the mean velocity, but also other flow parameters, such as the standard deviation of fluctuating velocities, deviate from their true values, due to the bias effect. The velocity bias can thus be considered a flow phenomenon [Zhang, 2002].

In situations where the data density is high, this bias can be avoided by equal time sampling of the processor, thereby not relying on the biased particle arrival times. Alternatively, velocity histories can be created by time stamping each sample, and then re-sampling the velocity history in equal time intervals. When the data density is low, however, these methods are not feasible since they operate by discarding many of the velocity samples [DeGraaff, 1999].

When analyzing velocity bias, three conditions are usually assumed: uniform seed density, a spherical measuring volume, and isotropic conditions existing inside the measuring volume. The first condition eliminates seeding effects from the analysis while the latter two conditions eliminate the basis for other biasing mechanisms [Loseke and Gould, 1991].

Several different correction schemes have been developed to correct the biased data by post-processing the data samples. A brief overview of some correction methods will be presented (see

[Loseke and Gould, 1991]). The first of the correction methods is the two-dimensional weighting function (MT2-D) proposed by McLaughlin and Tiederman [McLaughlin and Tiederman, 1973], also known as the reciprocal velocity method. They hypothesized that the bias error is proportional to the magnitude of the instantaneous velocity, and introduced a weighting function that is the inverse of this magnitude. This method is very limited though, as the absolute value of each individual velocity vector has to be known.
The next method is the residence or transit time (RT) correction. The transit time can be determined by measuring the burst lengths. However, this is not a straightforward matter, because several important problems occur with this technique [Van Maanen, 2000]. Often a too short transit time is measured due to e.g. eccentrically moving particles through the measurement volume or weaker scattering particles. This leads to higher values for the measured velocities. Besides this, the transit time is usually short. Most clocks which are used for the measurement of transit times have a lower resolution than necessary and therefore, the accuracy of the determination of the transit time is often insufficient for bias correction.
As a third method, the time between data (TBD) method is often applied. The inverse of the time between each realization, or inter arrival time, is the weighting factor in this case.
The fourth method is based on simulated data and is called the conditional measurement rate (CMR) method. Since this method is rather complex and the results of this correction are not that good (due to overcorrection), the CMR method has not been tested.
Finally, the velocity pdf shape (VPS) correction technique is introduced. This is the most recent correction scheme and uses an empirical function, in contrast to the other methods, which attempts to transform the skewed (i.e. biased) PDF into a symmetrical Gaussian (normal) distribution shape. Uniform seed density is unnecessary when using this correction and thus the method, in principle, is applicable in highly turbulent regions with poor seeding conditions. Two variations were applied in this study: VPS1 and VPS2. The VPS methods use the ensemble analysis technique and can be applied only after $\overline{u}$ is calculated. Table 6.1 gives a summary of the weighting functions and the data that are required for each method applied.

Table 6.1: Proposed weighting functions

Correction	Weighting function, w_i	Data used
MT2-D	$1/\sqrt{u_i^2 + v_i^2}$	u, v
RT	$1/T_{tt,i}$	u, T_{tt}
TBD	$1/T_{TBD,i}$	u, T_{TBD}
VPS1	$\lvert 1 + E_i \rvert^{1.5}$	u
VPS2	$(1 + E_i)^{1.5}$, $E_i \geq -1$ $(1 + \lvert E_i \rvert)^{1.5}$, $E_i < -1$ with $E_i = (\overline{u} - u_i)/\overline{u}$	u

The ensemble corrected local mean can be obtained with the following relation:

$$\overline{u} = \frac{\sum_{i=1}^{N_t} u_i w_i}{\sum_{i=1}^{N_T} w_i} \tag{6.2}$$

Loseke and Gould [Loseke and Gould, 1991] state that the VPS2 method gives the best bias correction. Due to the fact that velocity bias is still topic of debate, the best correction method for the performed measurements does not have to be the VPS2 method. Therefore, it is necessary to check the correction methods. Usually, these correction methods are compared to the unbiased (equal time sampling) data. As stated above, calculation of the unbiased velocity is not always feasible. Therefore, instead of the unbiased velocity a theoretical approach is applied. Four theoretical descriptions for the velocity profile of a turbulent pipe flow have been compared to the ensemble mean velocity. Measurements on this pipe flow have been done at $Re = 190 \cdot 10^3$, with a characteristic mean velocity U of approximately 1.9 m/s. More details about this flow can be

found in chapter 7. Besides the description of Gersten and Herwig (equation 2.16) and the Power Law of Nikuradse (equation 3.1 with $n = 7$, due to the Reynolds number), two other descriptions have been used:

Fay [Fay, 1994]:

$$\frac{\overline{u}}{U_{max}} = \left(\frac{60}{49}(1 - \frac{r}{R})^{\frac{1}{7}}\right)/U_{max} \tag{6.3}$$

Schlichting [Schlichting, 1965]:

$$\frac{\overline{u}}{U_{max}} = \left(U_{max} - 2.5u^* \ln \frac{R}{y}\right)/U_{max} \tag{6.4}$$

As can be distinguished in figure 6.7, the normalized velocity profile of a measured pipe flow, is mainly enclosed by the theoretical approaches of Nikuradse and Gersten and Herwig. The measured velocity profile is based on the arithmetical average and can be biased towards a higher velocity. Therefore, the best theoretical description comes from Nikuradse. Furthermore, as the log-log plot of the measured axial pipe velocity to the power of 7 versus the distance to the wall is a straight line, it is proven that the flow at this position is a well developed turbulent pipe flow.

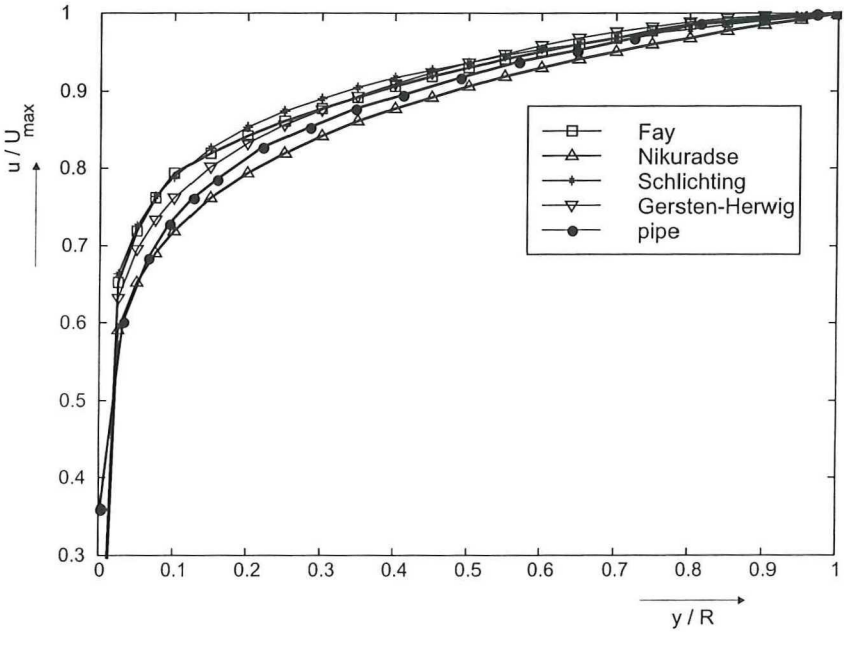

Figure 6.7: Normalized velocity profiles of four theoretical descriptions and a measured pipe flow at $Re = 190 \cdot 10^3$

The data of the pipe flow measurement were corrected for velocity bias by the following methods: MT2-D, RT, TBD, VPS1 and VPS2. The relative deviation from the theoretical, unbiased, velocity is given by:

$$(\overline{u}_c - \overline{u}_{ub})/\overline{u}_{ub} * 100 \tag{6.5}$$

Where $\overline{u}_c$ is the corrected local mean velocity and $\overline{u}_{ub}$ the theoretical local unbiased mean velocity. Figure 6.8 shows the relative deviation of the mentioned correction methods on the measured pipe flow velocities from the best theoretical fit (Nikuradse's Power Law), as well as the biased arithmetical mean velocity. As long as the error is small, i.e. less than 4%, the data need not be

corrected [Loseke and Gould, 1991]. This is usually the case for turbulence intensities less than 15%. For higher turbulence intensities, velocity bias correction is useful (especially downstream of the venturi). The MT2-D method should not be used, this method makes the error even worse! The RT and VPS1 methods overcorrect the error too much close to the wall, so the TBD and VPS2 methods are left. Both methods remain in the 4%-zone, though for high turbulence intensities (i.e. close to the wall), when a correction method is necessary, the VPS2 method shows a trend towards overcorrection. This is an important point, because the VPS2 method is overcorrecting 3.5% close to the wall, where the turbulence intensity in pipe flow is about 35%. After the throat, the turbulence intensity increases up to approximately 80% close to the wall in the diffuser. Probably, the VPS2 method will overcorrect with more than 4% in that case. Therefore, the TBD correction method has been chosen to apply on the data.

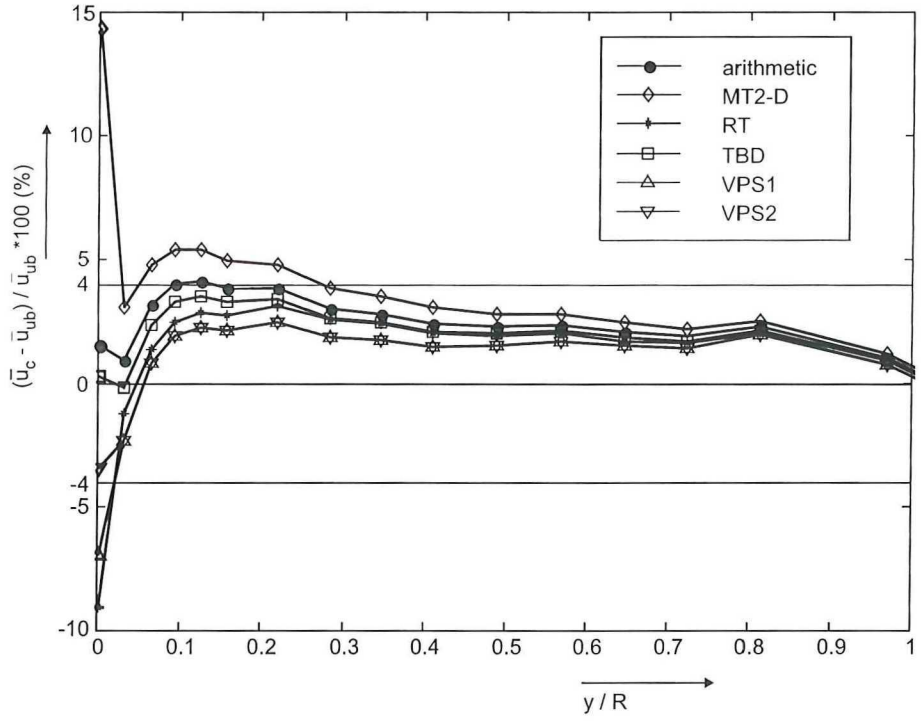

Figure 6.8: Relative deviation from the theoretical description of Nikuradse (eq. 3.1) for the arithmetical average and five velocity bias correction methods

6.3 Auto correlation function

Using the slotting technique with local normalization (see [Van Maanen, 1999]), the ACF is derived directly from the data, instead of using the Fast Fourier Transform (FFT). The algorithm assigns products of two individual velocity estimates to 'slots' of finite width, depending on the time difference of the two velocity estimates. The value of the slot width and window could be chosen by the user of the program `acf.exe`. Due to statistics: the more data, the less erratic the ACF will be. Important to know is that at time shift 0 (or slot 0) the ACF is normalized to 1. Immediately after that (in slot 1) the ACF drops because the noise contribution in the correlation coefficient vanishes as the noise is uncorrelated with the velocity component and with itself [Nievaart, 2000].

6.3.1 Properties of the ACF

Besides the derivation of the integral time and Taylor time scale, the ACF offers more properties of the signal and flow.

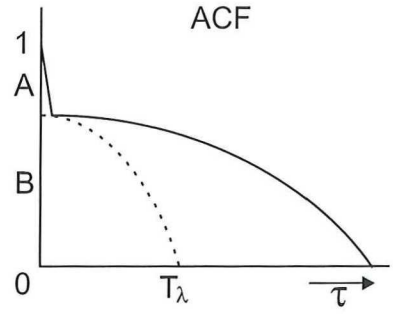

Figure 6.9: Sketch of the ACF with noise peak

According to section 2.6, the Taylor time scale can be derived by fitting a parabola to the ACF at $\tau = 0$ using the least square approach. In this way the vertical axis is cut in two: the mean square (MS) value of the measured velocity estimates is the sum of the MS values of the noise and the turbulent velocity fluctuations. Shortened in a formula:

$$MS(measured) = MS(noise) + MS(turbulence) \tag{6.6}$$

Defining the contribution of turbulent velocity fluctuations to the ACF at $\tau = 0$ as σ_t, the noise contribution A and the turbulent fluctuations contribution B in the ACF of figure 6.9 become:

$$\begin{aligned} A &= \frac{MS(noise)}{MS(measured)} = \frac{1 - \sigma_t^2}{MS(measured)} \\ B &= \frac{MS(turbulence)}{MS(measured)} = \frac{\sigma_t^2}{MS(measured)} \end{aligned} \tag{6.7}$$

With this result, Van Maanen [Van Maanen, 1999] gives an estimate for the signal to noise ratio (SNR):

$$SNR = \sqrt{\frac{B}{A}} = \sqrt{\frac{\sigma_t^2}{1 - \sigma_t^2}} \tag{6.8}$$

For LDA measurements, a SNR of 5 to 8 is an excellent figure, while with HWA an SNR of 300 is readily achieved [Van Maanen, 1999].

The shape of the ACF gives some quantitative information about the flow as well. In many cases, the slope of the ACF decays exponentially after the noise peak at $\tau = 0$. Unexpected peaks in the ACF show that some slots show more correlation than others, which is suspect. In figure 6.10 is sketched how big and small vortices influence the slope of the ACF. Small vortices indicate dissipation, which results in a big negative slope and a small Taylor micro time scale ($T_{\lambda,dis}$). Big vortices indicate production, a smaller negative slope and a larger Taylor time scale ($T_{\lambda,prod}$). In the flow both dissipation and production occur, so the real ACF is a combination of both curves (with $T_{\lambda,flow}$). Two ACF's of the same flow, though of different positions in the flow, can thus be compared. The position in the flow where more dissipation takes place, can be distinguished by a steeper decay of the ACF.

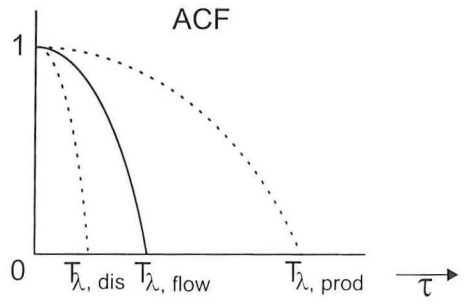

Figure 6.10: Sketch of the construction of an ACF

6.4 Power spectrum

The power spectrum can be determined from the ACF. Mathematically, the power spectrum is the FFT of the auto correlation function, but this power spectrum shows a lot of noise at the higher frequencies. To solve this problem, the ACF has been fit by a smooth curve (see [Van Maanen, 1999]). The power spectrum of this fitted ACF is a smooth curve too and gives a good approximation of the power spectrum at higher frequencies. The represented power spectra are a combination of both spectra: for the lower frequencies the original power spectrum is used, while the spectrum for the higher frequencies is represented by the fitted spectrum. Instead of the frequency and $S(\omega)$, the figures are plotted with the wavenumber, $k = \omega/\overline{u}$, and the one-dimensional energy spectrum $E(k)$, which equals $S(\omega)\overline{u}$. The weighting factors of both spectra (original and fitted) are shown in figure 6.11. The cutoff wavenumber where the PS starts to be extremely noisy, compared to the part of the spectrum of the macro scales, is called k^*. This value is a rough visual estimation. Up to this wavelength, the direct calculated spectrum is a part of the new constructed power spectrum. The more data are achieved, the less noisy the spectrum is and thus the bigger k^* will be.

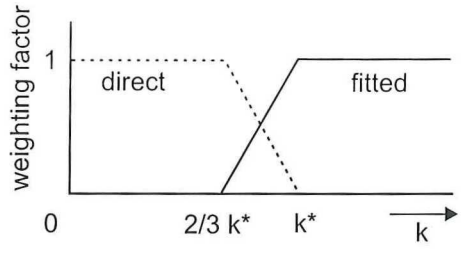

Figure 6.11: Weighting factors for the direct calculated and fitted power spectrum to obtain a good power spectrum for all wavenumbers

6.4.1 Properties of the power spectrum

The inertial subrange of $E(k)$, the part where the cascade process takes place, of a turbulent equilibrium flow has a specific shape. In this range of wavenumbers, the power spectrum is independent of the macro scales, as well as the viscosity ν [Nieuwstadt, 1998]. The only parameters which play a part in the spectrum are the dissipation ϵ, which describes the energy transport along the cascade, and the wavenumber k. Using dimension analysis one can find for an uniform, isotropic turbulent flow:

$$E(k) \sim \epsilon^{2/3} k^{-5/3} \tag{6.9}$$

Therefore, in turbulent equilibrium flows the power spectrum in the inertial subrange should show a straight line with a slope of -5/3. When the decrease of $E(k)$ is less in this region, it is an indication for a position in the flow where more dissipation than production occurs (e.g. close to the wall in pipe flow). In this case the power spectrum will be 'wider', which leads to more energy available for the smaller vortices and thus more dissipation.

Measurements at one position (e.g. in the throat of the venturi) at different positions from the wall, can show different heights in the power spectrum for low wavenumbers. The higher the spectrum, the more production (and the wider the ACF, see section 6.3.1).

The area under the power spectrum has the same value of the MS of the turbulent fluctuations ($\overline{u'^2}$). This value is used to scale the power spectrum.

Chapter 7

Results

The set-up described in chapter 5 has been used to perform several measurements in the flow. In this chapter, first some general information about the measurement locations and flow properties will be given. After that, a selection of the measurements will be presented regarding time-velocity diagrams, velocity profiles, turbulence intensities, auto correlation functions and power spectra.

7.1 General information

At nine locations, the axial and tangential velocity components at a number of positions from the wall (a traverse) have been measured. The exact locations are depicted in figure 7.1. Upstream one measurement location is positioned. Furthermore, the discussed windows in the throat and diffuser are visible. Finally, the five downstream locations, nominated 0, 2, 3, 4 and 5D down, can be found. When the venturi tube was removed once, the measurements in pipe flow have been performed through the 2D down measurement window located at the 1D upstream position.

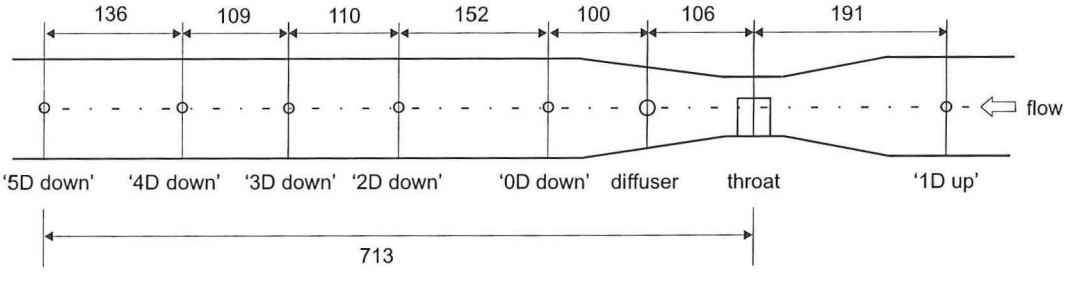

Figure 7.1: Exact location of the eight measurement locations, dimensions in mm

All measurements have been performed at a characteristic mean upstream velocity U of approximately 2.0 m/s, resulting in an upstream Reynolds number of $2.0 \cdot 10^5$. The exact values of the selected mean upstream velocity and LDA parameters per traverse can be found in appendix A. Immediately after the measurements, the data was checked quickly with the program `CofLDA.exe`, showing rough figures of the time series, probability density functions and the time between data. The obtained data files have been tested later with all diagnostic tools (section 6.1). An example of the results of this tests on two measurements can be found in appendix B.

7.2 Time-velocity diagrams

The first mentioned diagnostic tool in section 6.1 was the velocity signal. These diagrams give a lot of information about the frequency and magnitude of the turbulent velocity fluctuations. The larger the relative magnitude (according to the value of the local mean velocity), the higher the turbulence intensity will be. Of each traverse, three positions have been selected to represent the time-velocity signal. These positions are $y/R = 0.01$ (close to the wall), 0.1 (the steep part of the axial velocity profile of turbulent pipe flow) and 1.0 (center of the flow), respectively. These figures can be found in appendix C. Generally speaking, the relative velocity fluctuations at the centerline at every measuring location are small compared to the fluctuations closer to the wall, even at $y/R = 0.1$. This results in low turbulence intensities at the centerline, see section 7.5. In the diffuser and at 0D downstream, the fluctuations at $y/R = 0.01$ and 0.1 are of the same order of magnitude, while at the centerline the fluctuations are still of the same order as in turbulent pipe flow. At 2D and further downstream, the fluctuations at the centerline increase towards the magnitude close to the wall. As this is the case even at 5D downstream, which differs from the almost identical u-t diagrams of turbulent pipe flow and 1D upstream, it can be concluded that at the last measuring position the effects of the venturi can still be measured.

Time-velocity diagrams also show flow reversals in and downstream of the diffuser, as the velocity in the u-t diagrams sometimes drops below 0 m/s, as can be seen in figure 7.2. Flow reversals occur only in the diffuser and at the 0D and 2D downstream locations close to the wall. From this type of diagrams, it can be concluded that flow reversals occur up to $y/R = 0.10$, 0.27 and 0.02 for the positions in the diffuser and at 0D and 2D downstream, respectively.

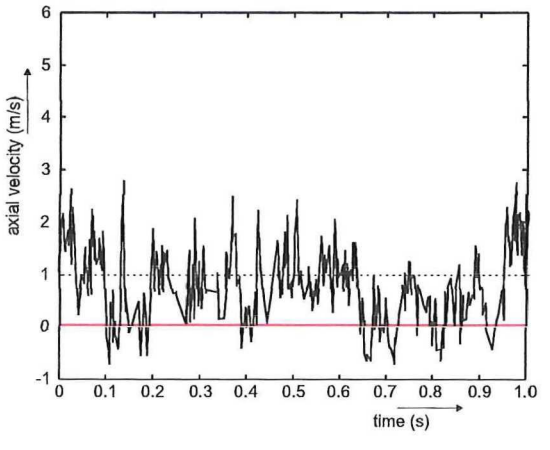

Figure 7.2: Axial time-velocity profile at $y/R = 0.01$ in the diffuser showing reversals, upstream $Re \approx 180 \cdot 10^3$

7.3 Probability density functions

Besides the time-velocity diagrams, the linear and logarithmic probability density functions can be used as diagnostic tool. These PDF-figures at the familiar distances from the wall of each measuring location are listed in appendix D. The velocity range of the PDF-figures is directly related to the magnitude of the fluctuations in the time-velocity diagrams. For this reason, in general, the velocity range is larger the closer to the wall (more diversity in the measured velocities). The figures for turbulent pipe flow and 1D upstream show a 'Gaussian' shape and no frequency shift leakages. In

the throat, close to the wall the PDF is skewed towards a higher velocity. At the locations where flow reversals occur (from diffuser to 2D downstream), the PDF's show negative velocities. Close to the wall at 3D, 4D and 5D downstream, the logarithmic PDF shows some negative velocities as well, though in such small amounts (less than 10^{-3} of the total measuring points), that this can not be seen as flow reversals. As could be expected on the basis of the time-velocity diagrams, the velocity range of the PDF-figures of 2D and further downstream are up to three times as wide.

7.4 Velocity profiles

Of each measured position, the local mean velocity is calculated, taking into account the TBD-velocity bias correction method (see equation 6.2). In this manner the axial and tangential velocity profiles can be depicted. Figure 7.3 shows the axial velocity profiles in the measurement section in real dimensions, as well as with a stretched diameter. The 'plug'like flow caused by the venturi is clearly visible in this figure. Note that not all measurements have been performed with an upstream Reynolds number of $196 \cdot 10^3$, but with a slightly lower Reynolds number. These are the measurements in turbulent pipe flow and in the throat. These flows have a Reynolds number which is 3.6% and 8.6% lower, respectively. The difference in Re for the pipe flow did not influences the shape of the velocity profile (compare the velocity profile at 1D upstream with the one of the turbulent pipe flow). Downstream of the venturi, the profiles are not axis-symmetric. The reason for this behavior is not clear, it could depend on the measuring method (refractional problems with some of the window 'screws') or the flow really behaves like this because of the venturi. The existence of a 'swirling' flow is not likely, as these velocity effects will be averaged out.

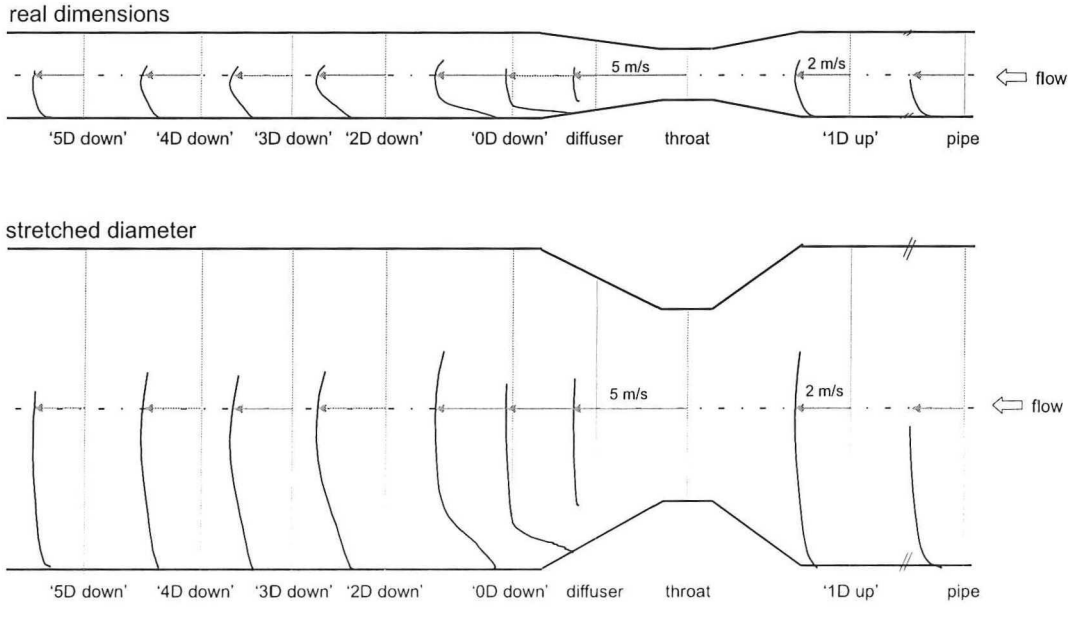

Figure 7.3: Axial turbulent velocity profiles in the measurement section, upstream $Re \approx 2.0 \cdot 10^5$

These axial velocity profiles are shown in a more quantitative way in figure 7.4. In contrast to figure 3.21, $\overline{u}_{max}$ is situated at the centerline in the throat. At 5D downstream, the velocity profile is more flatten than at 1D upstream, which was to be expected according to the information in sections 3.4 and 3.5. The tangential velocity profiles can be found in figure 7.5. The tangential component is close, though not equal, to 0 m/s, due to influences of the axial velocity component. As the measurement section caused by the laser beams is not aligned in a vertical direction exactly

(which is very difficult), a small component of the axial velocity will be easily measured. This axial velocity is considerably higher than the tangential velocity, resulting in a 'tangential' velocity not equal to 0 m/s. Therefore, no conclusions can be drawn about flow reversals and radial velocity components on the basis of figure 7.5

Using the measurement positions and the measured local mean velocities, a flow rate can be calculated by 'integrating' the velocity profile in a discrete way. The cross-section will be divided in small annular surfaces. Each surface is multiplied with the measured local mean velocity. Adding up all small surfaces multiplied with $\overline{u}$ gives the calculated flow rate Φ_V. Dividing the flow rate by the total cross-section gives the calculated average characteristic velocity U_{Φ_V}, which can be compared to the chosen characteristic velocity U. These values, as well as the calculated local Reynolds numbers, are listed in table 7.1. Downstream of the venturi, the calculated value U_{Φ_V} is considerably higher than U at 0D downstream (9.1%). At the other locations, the difference between the chosen U and the calculated U_{Φ_V} is less (1.5 to 5.6%). This deviation can be explained by the shape of the axial velocity profile: downstream of the venturi, the profile is not axis-symmetrical, resulting in higher local mean velocities for the annular surfaces. Furthermore, for the calculated flow rate, only about 20 measuring points have been used. Therefore, the calculated value is only a rough estimation of the chosen flow rate. The calculated value will be more accurate if more measuring points are available along the traverse.

Table 7.1: Calculated flow rates and characteristic velocities

	Φ_V $(10^3 m^3)$	U_{Φ_V} (m/s)	Re_{Φ_V} $(\cdot 10^3)$	U (m/s)	Re $(\cdot 10^3)$
pipe	0.143	1.82	181	1.91	190
1Dup	0.148	1.88	187	1.97	196
throat	0.139	4.93	295	4.99	298
diffuser	0.142	2.85	227	3.09	246
0Ddown	0.169	2.15	214	1.97	196
2Ddown	0.160	2.02	203	1.97	196
3Ddown	0.159	2.02	202	1.97	196
4Ddown	0.157	2.00	199	1.97	196
5Ddown	0.146	1.86	185	1.97	196

7.4.1 Profiles in wall units

As stated in section 2.3, the structure of a turbulent pipe flow consists of four layers. Due to the size of the measuring volume in the flow, only measurements in the logarithmic wall layer and wake region have been performed. In the logarithmic region, the axial velocity profiles in wall units of turbulent pipe flow and one diameter upstream should equal the theoretical approach of Bird (eq. 2.18). As the turbulent velocity profiles downstream of the 1D upstream location differ from the pipe flow profile (figure 7.4), it is expected that the downsteam velocity profiles in wall units will not fit the theoretical description. The turbulent axial velocity profiles in wall units are depicted in figure 7.6.

Figure 7.6*a* shows the logarithmic behavior of the pipe flow and the flow 1D upstream, which fit with Bird's characterization. The (almost) uniform velocity in the throat is clearly visible. Although the shape of the divergent part of the venturi differs from the diffuser used in the experiments of Okwuobi (section 3.4), the velocity profiles of the diffuser and 0D downstream measurements (fig. 7.6*b*) follow the same trend as the profiles in figure 3.10. The farther downstream in the diffuser, the more the profile deviates from the theoretical line. In both figures, the profiles cross the theoretical description just below $y_+ = 700$. Downstream of the diffuser, the top of the profiles

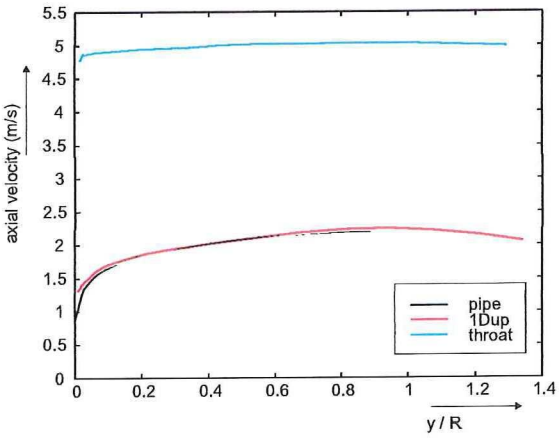

(a) Velocity profiles of the pipe flow, at 1Dup and throat

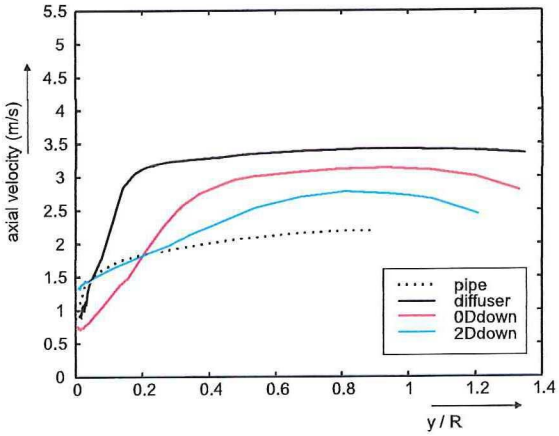

(b) Velocity profiles in the diffuser, at 0D and 2D downstream

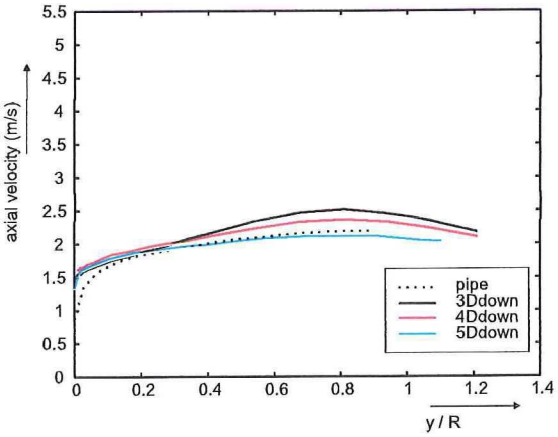

(c) Velocity profiles at 3, 4 and 5 D downstream

Figure 7.4: Axial turbulent velocity profiles

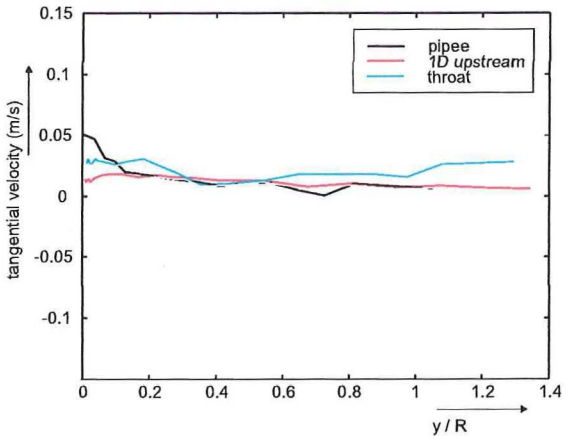

(a) Velocity profiles of the pipe flow, at 1Dup and throat

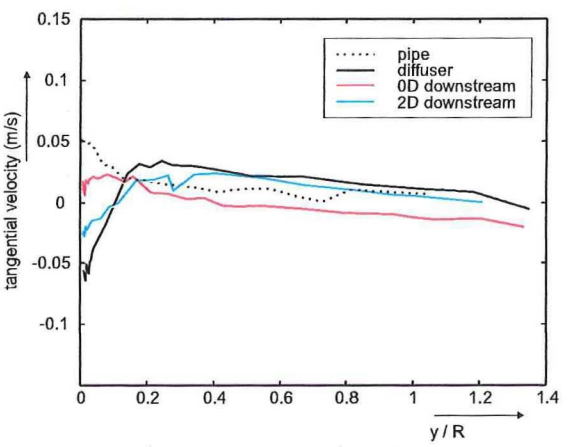

(b) Velocity profiles in the diffuser, at 0D and 2D downstream

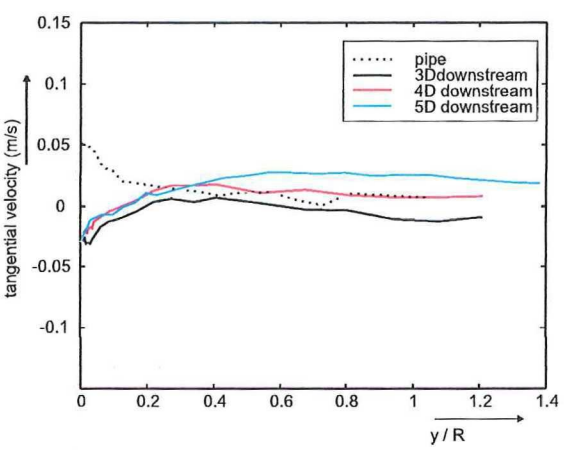

(c) Velocity profiles at 3, 4 and 5D downstream, respectively

Figure 7.5: Tangential turbulent velocity profiles

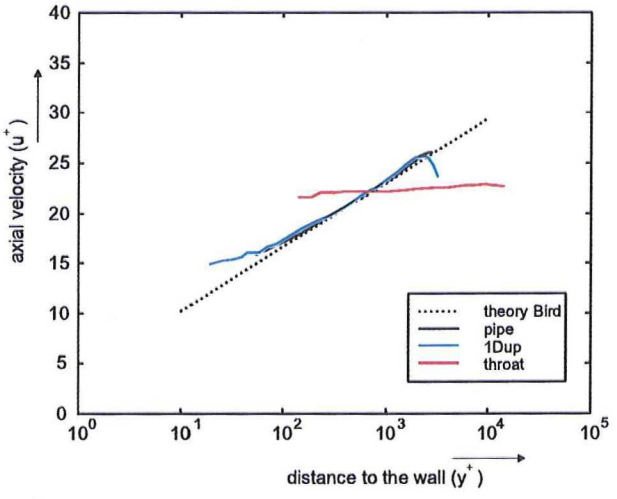

(a) Velocity profiles of the axial velocity in the pipe flow, at 1Dup and throat, in wall units

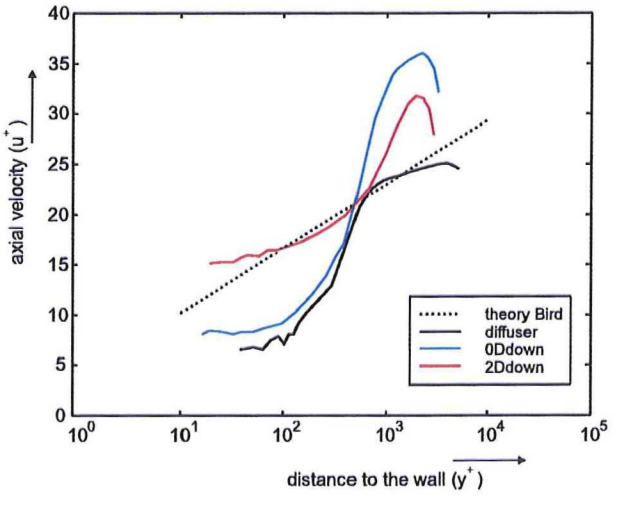

(b) Velocity profiles in the diffuser, at 0D and 2D downstream, in wall units

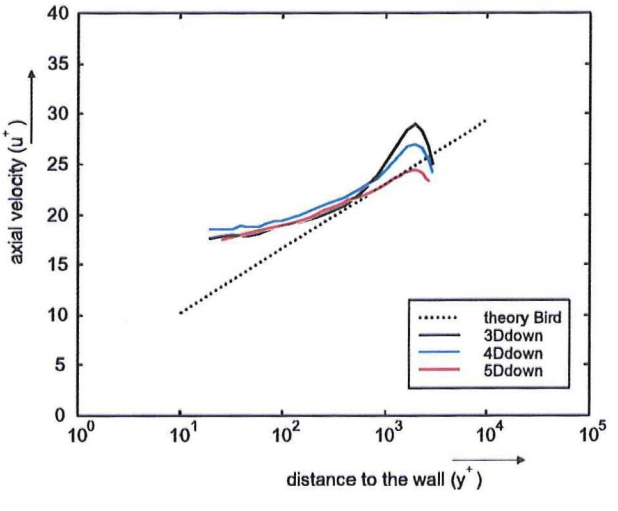

(c) Velocity profiles at 3, 4 and 5D downstream, in wall units

Figure 7.6: Axial turbulent velocity profiles in wall units. The dashed line is the theo-

slowly decreases towards the value of the top of the pipe flow profile (fig. 7.6*c*). The increase of the profiles downstream of the diffuser for $y_+ < 700$ towards a higher value than the theoretical expectation attracts the attention. On the basis of figure 7.6*c* it can also be concluded that close to the wall, the velocity profile at 5 diameters downstream still does not equal the profile of a turbulent pipe flow.

7.5 Turbulence intensities

The axial and tangential turbulence intensities have been calculated by using equation 2.8. For the mean velocity, the calculated local mean velocity of each measuring point has been chosen, instead of a maximum upstream velocity or friction velocity. Because of small deviations in the mean velocity upstream of the venturi between every measuring position (the flow loop had to be started up again for every traverse) and large differences in the friction velocity (up to 2.5 times), this method with the local mean velocity seems to be the most accurate.

The calculated turbulence intensity is corrected for the noise contribution. This correction makes use of the auto correlation function. At $\tau = 0$, the noise and turbulent fluctuations contributions can be distinguished in the ACF. Multiplying the local turbulence intensity with the square root of the value of the turbulent fluctuations contribution of the ACF provides the noise corrected turbulence intensity value. The values of the turbulent fluctuations contributions can be found in appendix E. The noise corrected turbulent intensity profiles are shown in figures 7.7 and 7.8.

Close to the wall the turbulence intensities increase a lot, for the applied definition of the turbulence intensity I and low local mean velocities close to the wall. In the center of the pipe (pipe flow) and at 1D upstream, I reaches a value of 3.6% (figure 7.7*a*). If this value was calculated with the mean upstream velocity, which in this case equals the characteristic mean velocity of the pipe flow or the flow at 1D upstream, the turbulence intensity would be 4.3%. This value is in agreement with the value for the turbulence intensity at the centerline of the reference measurement of figure 3.12*a*.

The streamlines of the flow will be compressed in the throat. Besides, due to the increase of the axial velocity in the throat, the effects of the turbulent velocity fluctuations will become smaller. This results in a very low turbulence intensity of 0.8% at the centerline. This is in reasonable agreement with the results of March [March, 1998]. Owing to the almost uniform local mean velocity and the compression of the streamlines, the turbulence intensity at the wall also has a relative low value. In the diffuser and at 0D downstream the velocity at the centerline is high compared to the velocity close to the wall ('plug'flow, fig. 7.4*b*), resulting in low turbulence intensities at the centerline, but high values close to the wall.

At 2D downstream, the turbulence intensity is high (about 3 times as high as at 1D upstream at the centerline). Only very close to the wall ($y/R < 0.02$), the profile equals the turbulent pipe flow profile. More downstream of this location, the turbulence intensity profiles slowly become more flat. Still, at 5D downstream, the turbulence intensity at the centerline is 4 times as high as the value of I 1D upstream, although the axial velocity profiles at these positions are much more consistent (fig. 7.4*c*). This is in agreement with the findings of Deshpande [Deshpande and Giddens, 1980].

The tangential turbulent velocity profiles follow the same trend as the axial profiles, though for each measuring location, the tangential profile is about 80% of the value of the axial profile. This is in agreement with the findings of Okwuobi [Okwuobi and Azad, 1973], see figure 3.12.

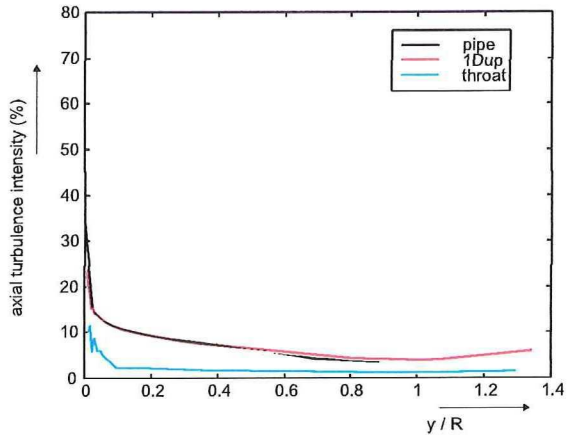

(a) Turbulence intensities of the pipe flow, at 1Dup and throat

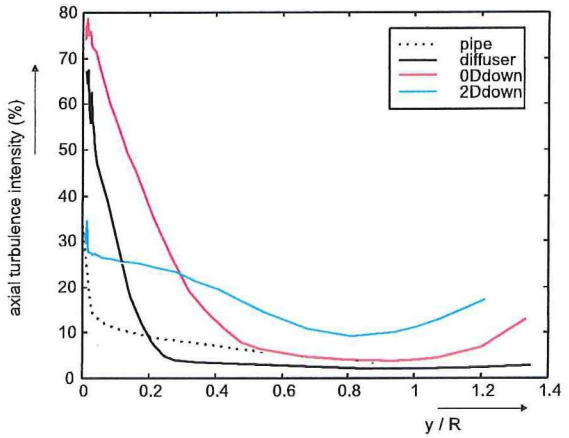

(b) Turbulence intensities in the diffuser, at 0D and 2D downstream

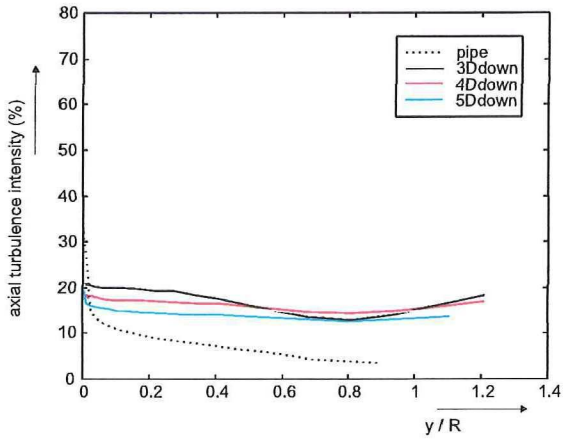

(c) Turbulence intensities at 3, 4 and 5D downstream

Figure 7.7: Noise corrected axial turbulence intensity profiles, with $I \equiv \frac{\sqrt{\sigma_u^2}}{\overline{u}} \cdot 100\%$

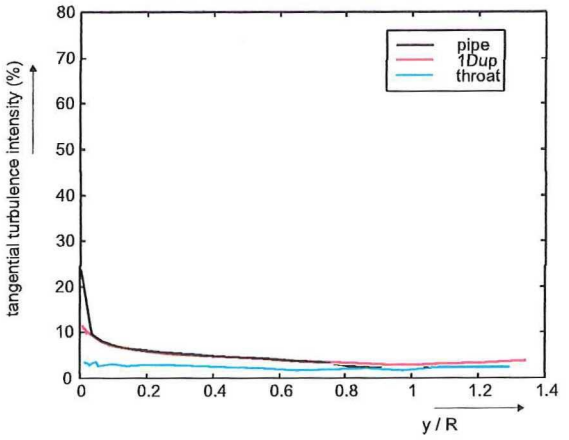

(a) Turbulence intensities of the pipe flow, at 1Dup and throat

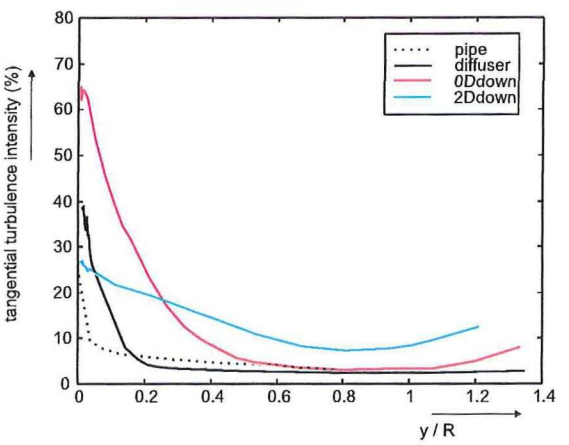

(b) Turbulence intensities in the diffuser, at 0D and 2D downstream

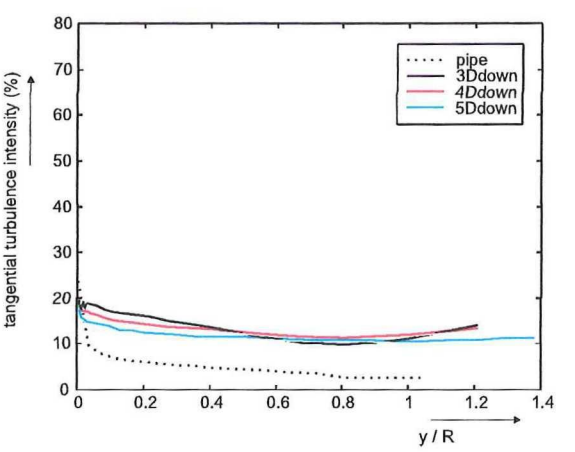

(c) Turbulence intensities at 3, 4 and 5 D downstream

Figure 7.8: Noise corrected tangential turbulence intensity profiles, with $I \equiv \frac{\sqrt{\sigma_u^2}}{\overline{u}} \cdot 100\%$

7.6 Auto correlation function

To give an indication of the development of the auto correlation function at three positions from the wall (y/R = 0.01, 0.1 and 1.0), the correlation functions of each measurement location have been drawn in the figures 7.9 to 7.11, using a slotwidth of 70 μs. The ACF of the pipe flow has been used as a reference measurement.

Furthermore, in appendix E the auto correlation functions at the three positions from the wall are depicted in one figure for each measuring location. In this appendix the turbulent fluctuations contributions of the given ACF's have been taken up as mentioned in the previous section. Finally, the signal to noise ratio is given.

The figures show the following properties (see also section 6.3). The ACF's of the turbulent pipe flow and 1D upstream are nearly identical, except for y/R = 0.01, because the measurement representing the pipe flow of this position is located at y/R = 0.03. In the throat, the ACF drops very quickly, resulting in a low Taylor time scale. This indicates a high dissipation and a low production rate. The dissipation at the centerline of the diffuser is less than in the throat, but still higher than for 1D upstream (this can be concluded from the way the ACF drops after τ = 0 s). Close to the wall, the production of turbulent kinetic energy increases, supposedly as a result of the flow reversals. This is reasonable, as in the flow reversal region at 0D downstream the production increases as well. Further downstream, at the centerline the production increases, while the dissipation rate at y/R = 0.1 is higher than for 1D upstream. At 5D downstream, the production at the centerline seems to start to decrease.

According to the macro time scale (eq. 2.22), which is the time it takes an eddy to break up, a lower value of T_m indicates a higher dissipation rate. The macro time scale in the throat and the diffuser are 22 and 51% of the 1D upstream value for T_m, respectively. This is in agreement with the results of the auto correlation functions.

While fitting the ACF to acquire a fitted power spectrum, the Taylor time scale can be found. This time scale is derived from three parabola fits through three points. This has been done in such a way, that the first 6 points of the ACF have been used in this calculation. However, this parabola fit still remains a rough estimation of the Taylor time scale. Equation 2.41 will give the Taylor length scale. This length scale is plotted in figure 7.12 for three positions from the wall for all measurement locations.

Although the Taylor time scale can not be derived very precisely, and as Townsend stated 'an unsuitable quantity to use as scale in theoretical discussion', this figure still gives a rough indication of the development of the Taylor length scale. L_λ in the turbulent pipe flow and 1D upstream are of the same order. In the throat, the length scale increases to twice the magnitude, though T_λ becomes very small in the throat. At the end of the diffuser, the length scale decreases to the initial length, but the influences of the venturi continue further downstream. The length scale slowly increases again up to 3D or 4D downstream. An increase in L_λ can be the result of two reasons: $\overline{u}$ increases more than T_λ decreases (throat) or $\overline{u}$ decreases less than T_λ increases (downstream).

The development of the Taylor length scale is in contrast with the development of the macro and Kolmogorov micro length scale (see equations 2.20 and 2.27), as these values decrease in the throat (to 60% and 41% compared to the values 1D upstream, respectively) and still are smaller than at 1D upstream in the diffuser (80% and 67%, respectively). The macro, Taylor and Kolmogorov time scales all decrease in the throat and diffuser, so the rapid increased axial velocity in the throat causes a large Taylor length scale. This scale is calculated with the axial velocity. Therefore, the

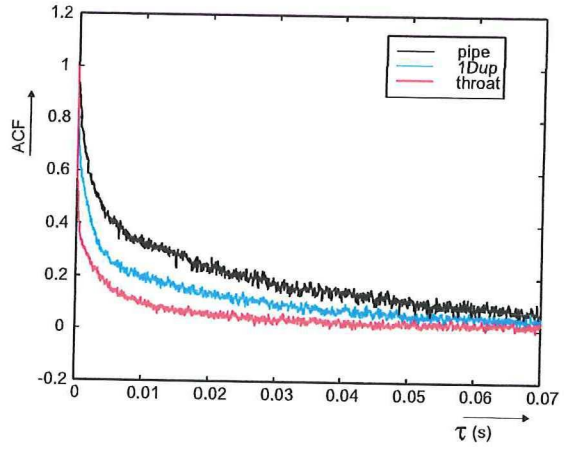

(a) ACF's of pipe flow, at 1D upstream and throat

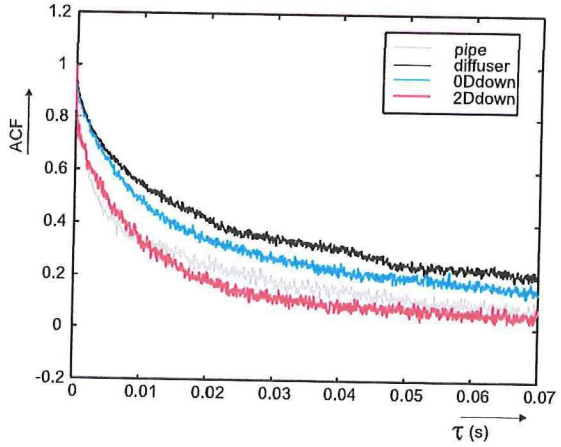

(b) ACF's at the diffuser, 0D and 2D downstream

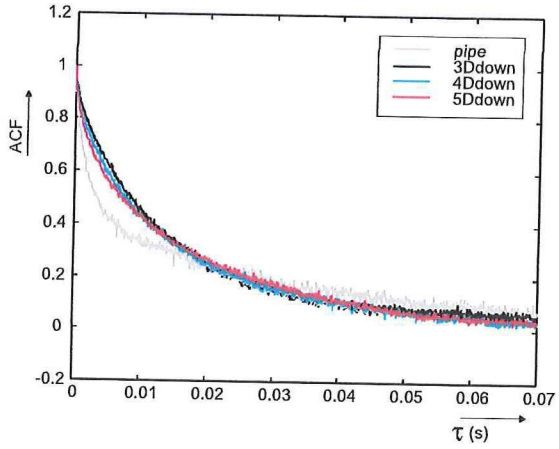

(c) ACF's at 3D, 4D and 5D downstream

Figure 7.9: Axial auto correlation functions at $y/R = 0.01$

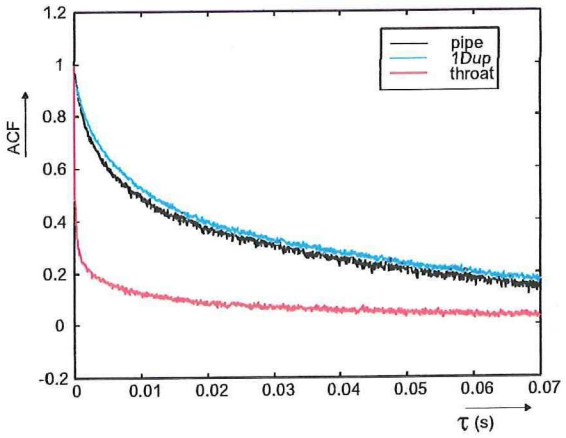

(a) ACF's of pipe flow, at 1D upstream and throat

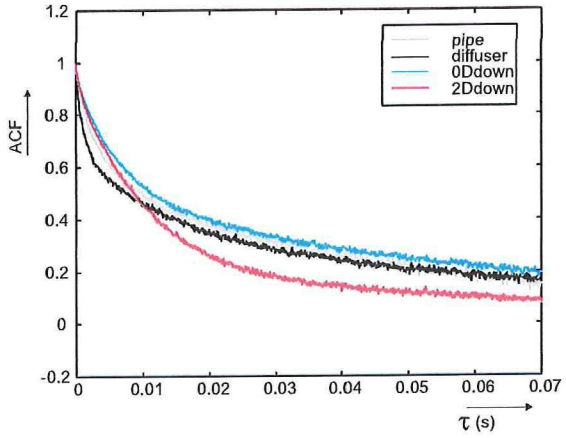

(b) ACF's at the diffuser, 0D and 2D downstream

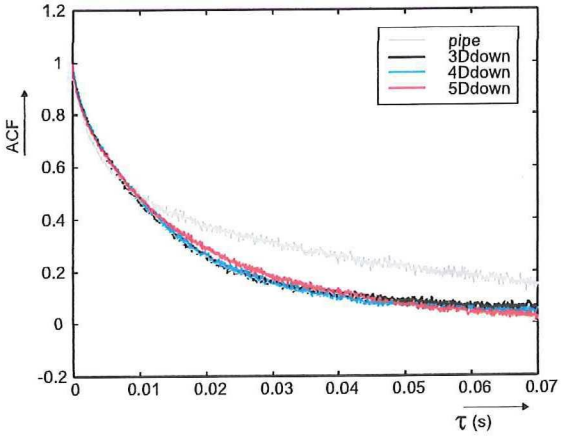

(c) ACF's at 3D, 4D and 5D downstream

Figure 7.10: Axial auto correlation functions at $y/R = 0.1$

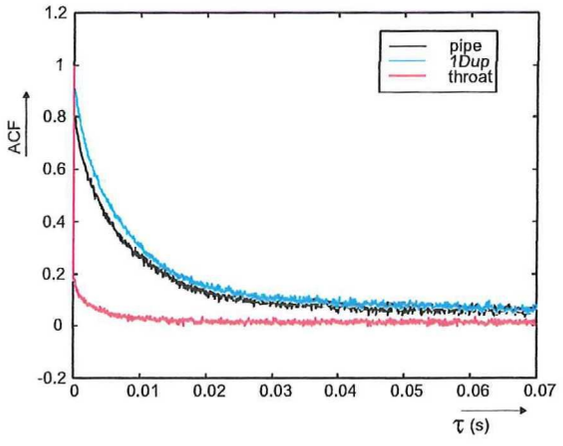

(a) ACF's of pipe flow, at 1D upstream and throat

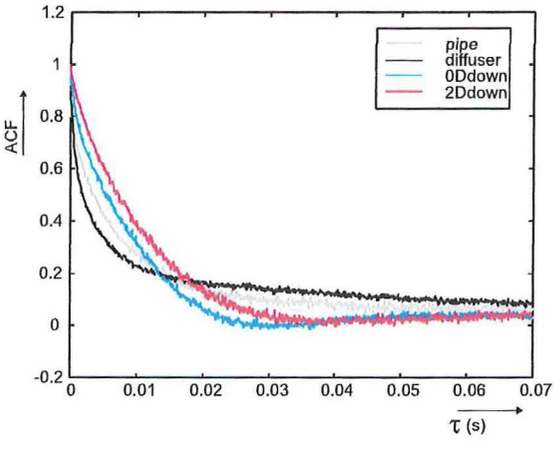

(b) ACF's at the diffuser, 0D and 2D downstream

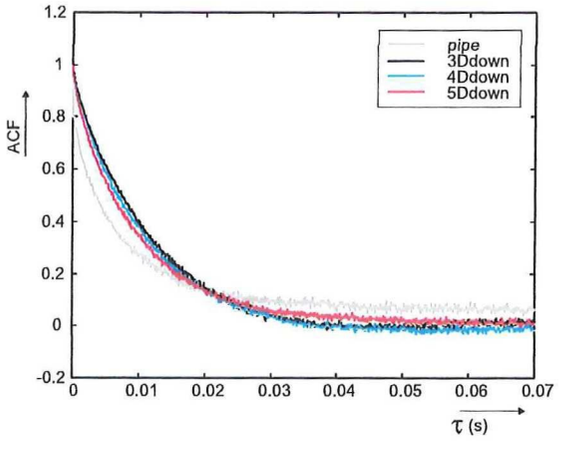

(c) ACF's at 3D, 4D and 5D downstream

Figure 7.11: Axial auto correlation functions at $y/R = 1.0$

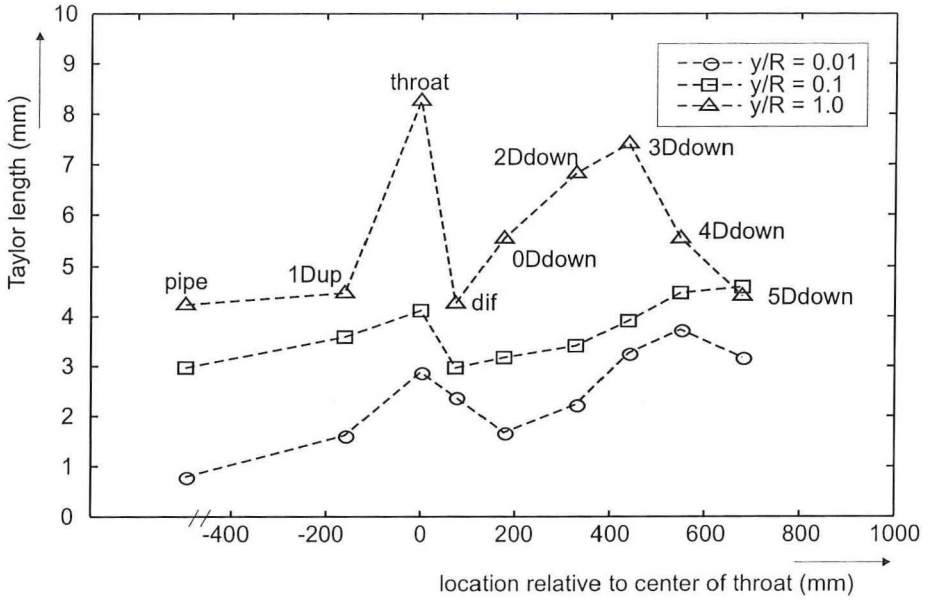

Figure 7.12: Taylor length scale for three positions from the wall for all locations, upstream $Re \approx 180 \cdot 10^3$. *Dashed lines for visual aid only.*

eddies probably only have these dimensions in the intermediate range in the axial direction, i.e. the eddies will stretch owing to the sudden contraction of the venturi.

The signal to noise ratio is lower than 5 in most cases, especially close to the wall, towards the centerline and in the throat (see appendix E). However, a low SNR does not always indicate a not so well performed measurement (e.g. close to the wall the measurements suffer from influences of the wall), but also low turbulence intensities, resulting in a relative large noise ratio, as is the case at the centerline in pipe flow and in the throat of the venturi.

7.7 Power spectrum

The same approach as in section 7.6 has been chosen to represent the power spectra. Again, at three positions from the wall the power spectra of all measurement locations will give an impression of the development of the power spectra. These spectra are given in figures 7.13 to 7.15.

All these power spectra are combinations of the directly calculated spectrum and a fit, as can been found in appendix F. In this appendix, the construction of three spectra per measurement location are depicted (at $y/R = 0.01$, 0.1 and 1.0). The directly calculated spectra have been scaled by determining the surface below the spectrum, as this should equal the MS value of the turbulent velocity fluctuations, $\overline{u'^2}$.

The higher the power spectrum, the more production occurs. Furthermore, comparison of the spectrum with equation 6.9 gives information about the production and dissipation rate. From this information and the given spectra, the following characteristics can be given. As with the ACF's, the power spectra of turbulent pipe flow and 1D upstream are identical for the three positions in the flow. The production at the centerline is in equilibrium with the dissipation and low, compared to the other measurements. Only at the throat the production all over the traverse

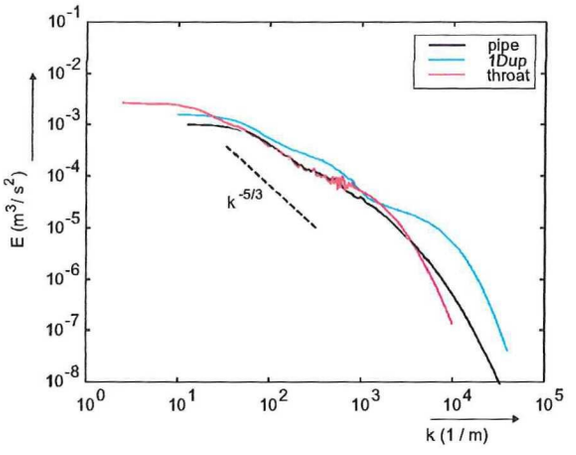

(a) Power spectra of pipe flow, at 1D upstream and throat

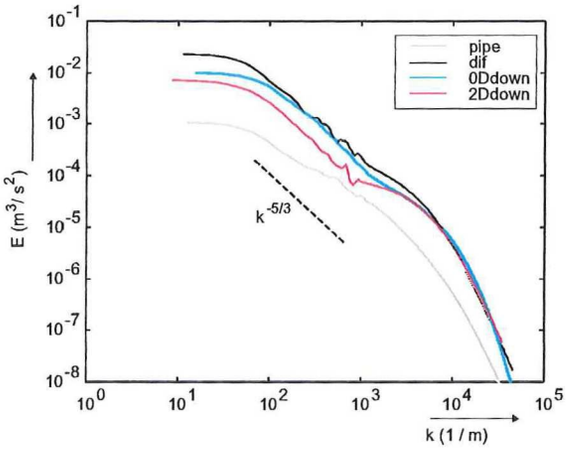

(b) Power spectra at the diffuser, 0D and 2D downstream

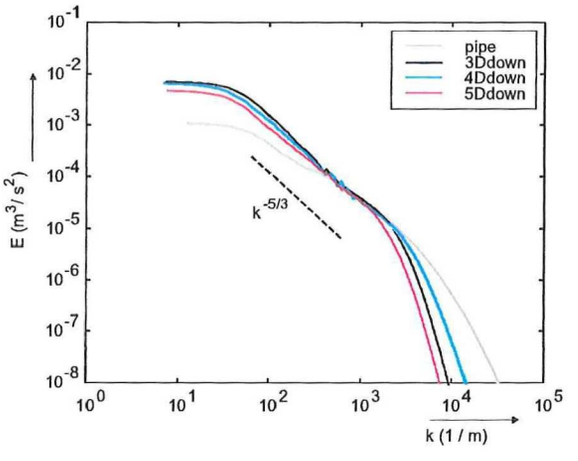

(c) Power spectra at 3D, 4D and 5D downstream

Figure 7.13: Power spectra at $y/R = 0.01$

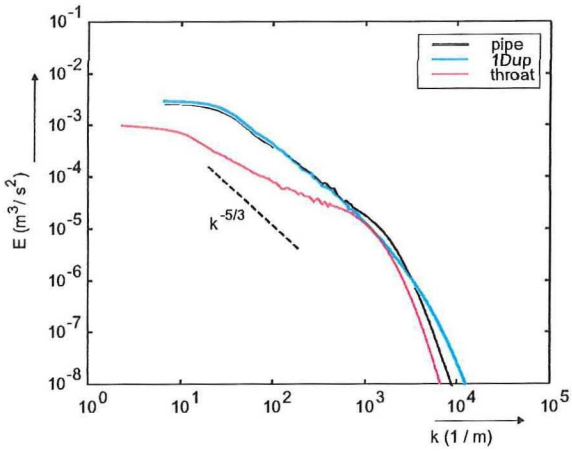

(a) Power spectra of pipe flow, at 1D upstream and throat

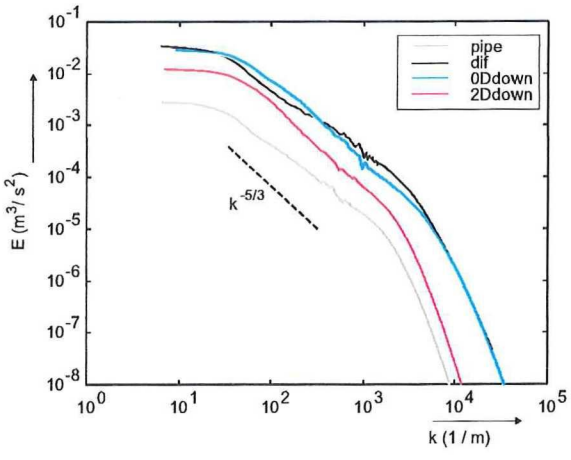

(b) Power spectra at the diffuser, 0D and 2D downstream

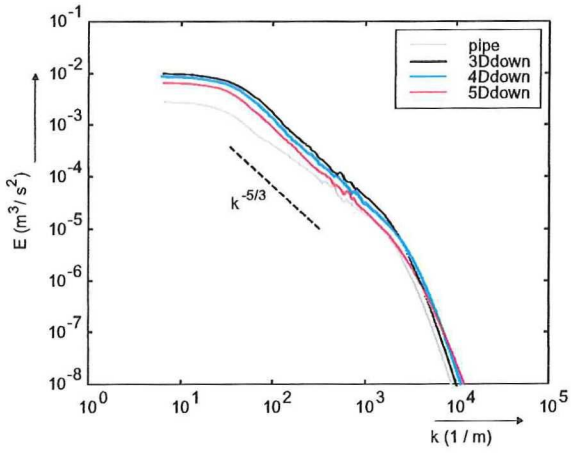

(c) Power spectra at 3D, 4D and 5D downstream

Figure 7.14: Power spectra at $y/R = 0.1$

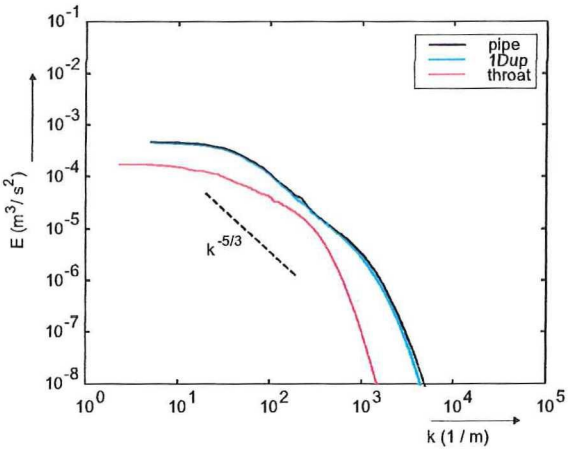

(a) Power spectra of pipe flow, at 1D upstream and throat

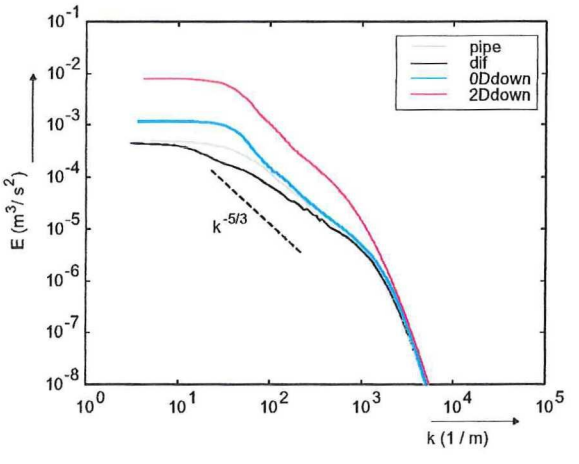

(b) Power spectra at the diffuser, 0D and 2D downstream

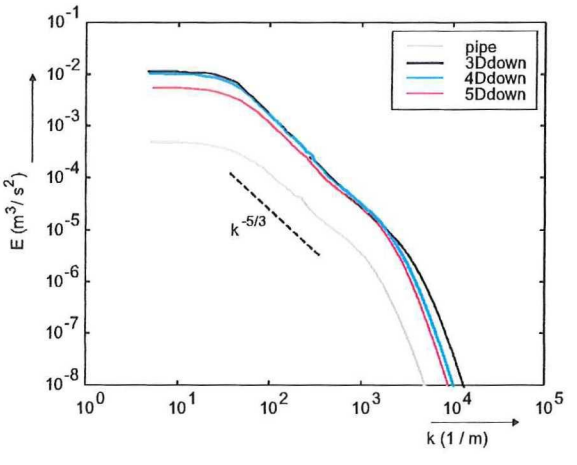

(c) Power spectra at 3D, 4D and 5D downstream

Figure 7.15: Power spectra at $y/R = 1.0$

is lower. At this location, dissipation plays an important role. In the diffuser, close to the wall the turbulence is isotropic. At this position the most production of the traverse takes place. In the flow reversal region at 0D downstream the turbulence is in equilibrium. The position with the highest production is $y/R = 0.1$. Further downstream, the flow is isotropic across the whole traverse, and the position with the maximum production rate has shifted towards the centerline. This is in contrast with the turbulent pipe flow, where the flow is only isotropic at the centerline and the maximum production is close to wall, but in a good agreement with the results of the ACF analysis.

Chapter 8

Conclusions

To investigate the properties of turbulent flow through a venturi, LDA measurements have been carried out on the flow field upstream, in the throat, in the diffuser and downstream of the venturi, as well as on turbulent pipe flow. On the basis of the work reported in this thesis, the following conclusions can be drawn.

8.1 Measurement techniques

In previous experiments, the thin sheet in the throat of the venturi caused a lot of trouble. Deepening of the chamber, where the sheet is in, took care that the sheet did not influences the flow anymore. After connecting a vacuum pump to the box around the throat of the venturi, to bring the pressure in the box below the pressure of the flow in the throat, the sheet did not swept away anymore. Furthermore, the sheet remained in the same shape. Therefore, less effects at measurements close to the wall occurred. This solution works fine, though the construction is very fragile.

The special construction in the diffuser part of the venturi, enables measurements in this part, even close to the wall.

The floats in the small vessel, together with a computer program controlled pump, took care of a constant flow rate during the measurements, as the water level in the large, upper vessel fluctuated 20 mm at maximum.

8.2 Signal processing

The Time Between Data correction method is the best of five checked methods to correct the velocity bias of the performed measurements.

8.3 Flow properties

The measurements in the pipe flow have been used to test if the flow field at the beginning of the measurement section of the set-up is correct. These measurements have been performed in a flow with an upstream Reynolds number of approximately $2.0 \cdot 10^5$. Fortunately, this is the case, as the measured velocity profile, in the bulk and close to the wall, equals the well known theoretical descriptions in these regions. This is the same case for the turbulence level. Therefore, the pipe flow measurements have been used to compare the results with those of the measurements 1D upstream of the venturi. As the flow at this position equals the turbulent pipe flow, the measurement position one diameter upstream is used as reference station for the other measurements.

The axial velocity profiles along the measurement section show an expected increase in average velocity in the throat. At this location, the velocity is almost uniform (the maximum velocity at the centerline is only 1% higher than the average velocity). The throat of the venturi causes a 'plug'flow behavior, which effect still can be measured 4 diameters downstream of the venturi.

Time-velocity diagrams, as well as the probability density functions, show flow reversals close to the wall in the diffuser, at 0D and 2D downstream.

As a result of the sudden contraction, the turbulence intensity in the throat of the venturi decreases to a quarter of the values of turbulent pipe flow: at the centerline, the turbulence intensity has a value of 0.8% only! This results in a very low signal to noise ratio in the throat as well. In the diffuser and 0D downstream, the turbulence intensity at the centerline goes back to the initial value, though close to the wall the intensity increases. At 2D downstream, the turbulence level at the centerline increases, while close to the wall the turbulence intensity decreases. Further downstream, the turbulence intensity profiles become more flat and decrease slowly toward the initial profile. At 5D downstream, the turbulence level along the traverse is still four times as high as the level 1D upstream, although the velocity profiles are almost equal. The axial and tangential turbulence intensity profiles have the same shape, though the magnitude of the tangential intensities is only 80% of the axial profiles.

From the auto correlation functions and power spectra the following characteristics about the production and dissipation level can be concluded. In turbulent pipe flow, and 1D upstream, the highest production takes place close to the wall (at least up to $y/R = 0.1$), while the turbulent energy will dissipate at positions towards the center of the flow, where the turbulence is in equilibrium according to the local power spectrum. Due to the contraction, almost no energy is produced in the throat of the venturi. At this location, dissipation dominates the flow. Therefore, the turbulence along the traverse is not in equilibrium anywhere. The flow reversals in the diffuser, 0D and 2D downstream make the production increase close to the wall, which lead to an equilibrium of the turbulent kinetic energy for $y/R = 0.01$ at the diffuser and 0D downstream. Still, dissipation dominates at the centerline of these two locations. At 2D and further downstream, the production at the centerline increases considerably. Meanwhile the production shifts from close to the wall (0D downstream) towards the center of the flow. Along the traverse, the turbulence is in equilibrium for these 4 locations. Only from 5D downstream, the production at the centerline starts to decrease.

Due to the (sudden) contraction of the venturi, the macro and Kolmogorov micro length scale decrease in the throat and are still small in the diffuser. This is in contrast with the Taylor length scale, which appears to increase at these locations. Supposedly, the eddies of the intermediate scale will stretch due to this contraction to a length twice the size of the eddies 1D upstream.

The effects of the venturi can still be easily measured at 5D downstream. Although the axial velocity profile looks quite the same as one of a turbulent pipe flow, the other measured properties differ a lot from that type of flow.

Chapter 9

Recommendations

The following recommendations are given to increase the quality of the measurements and to proceed the quest for measuring turbulent flow properties in single and multi phase flow, in and downstream of a venturi.

9.1 Measurement techniques

Although back scatter LDA is the less labor intensive measurement method, measurements performed in side scatter mode will increase the quality of the signal, as side scatter LDA gives a significant noise reduction and therefore, a higher signal to noise ratio. Hence, this measuring mode is mainly interesting for measurements in the throat. The side scatter method makes it also easier to measure the velocity components in two directions at the same position simultaneously (coincidence), which is necessary to calculate the Reynolds shear stress. This can be established with two probes, both emitting one color and receiving the other color laser beams. Measuring in side scatter mode at all measurement locations will cause a lot of adjustments to the set-up: at every measurement location, the pipe wall have to be replaced by a thin sheet. Around this part of the pipe, a box like the perspex box around the throat of the venturi, has to be installed.

The glass 'screws' mounted in the wall of the pipe at the measurement locations deserve special attention: some of the 'screws' scatter a lot of light, resulting in a low data rate and a high noise level. Besides this, the position of the flat side of the 'screws' relative to the axis of the pipe should be parallel. As the glass 'screws' are screwed in the wall, their position should be checked carefully, otherwise the traverse will not be measured perpendicular to the wall. Therefore, search for the best 'screw' for every traverse (i.e. fewest scattering of light by the glass and best fit compared to the axis of the pipe).

9.2 Signal processing

The velocity bias is still a topic of debate, as there is no consistency in literature. Therefore, when applying a velocity correction method, check for the best method.

9.3 Flow properties

As the influences of the venturi still can be easily measured at 5D downstream, some more traverse measurements in one phase flow can be carried out up to e.g. 10D downstream. At this location, it should be clear if the trends continue (like the decrease of production at the centerline at 5D downstream) and in which way they develop.

Downstream of the venturi, the maximum velocity of the axial velocity profile is not situated at the centerline of the pipe, resulting in a non-symmetric velocity profile. The reason for this behavior is not clear, neither the exact height of the position where the maximum velocity occurs. This phenomenon could be a result of some irregularities of the venturi. This can be easily checked: measurements performed at the downstream locations with a 180° rotated venturi should give the same velocity profile, though mirrored.

While measuring time-velocity signals with LDA in the flow, the pressure difference between an upstream location and the throat of the venturi could be monitored, in order to compare these results with literature. As the venturi will be used as a pressure difference flow metering device, it is useful to measure this property as well. Currently, the set-up is ready for pressure recovery measurements, as just upstream of the entrance and downstream of the outlet of the venturi the pressure difference can be measured. These measurements can be used for the third goal of the investigations of Shell, mentioned in chapter 1: investigation of the total pressure loss. Moreover, this loss is mainly caused in the divergent part of the venturi, as this is a very dissipative area.

Since the set-up is ready for two-phase flow measurements in the throat of the venturi, one can started carry out LDA measurements at this position in the flow. As in the two phase flow the volume fraction of the liquid part will be smaller than the gas part, the measurements have to be performed close to the wall (the flow will be stratified in this horizontal set-up). Therefore, for measuring velocity components at other locations, the adjustments mentioned in section 9.1 will be useful for this type of measurements as well, as a thin foil reduces the noise contribution from the wall (or glass 'screws') because the detector signal will be less affected by parasitic scattering at the wall [Nievaart, 2000].

Nowadays, it is known that in wet gas metering fluid properties influence the results. Several sources adduce that factors such as the surface tension could play a major role while measuring the flow rate of multi phase flows. This can be a point of attention for future multi phase flow measurements.

Bibliography

Absil, L. (1995). *Analysis of the Laser Doppler measurement technique for application in turbulent flows, PhD Thesis.* Delft University Press.

Azad, R. (1996). Turbulent flow in a conical diffuser: A review. *Experimental Thermal and Fluid Science*, **vol. 13**, pp. 318–337.

Batchelor, G. and Shaw, F. (March 1944). A consideration of the design of wind tunnel contractions. *Australian Council for Aeronautics.*

Bird, R., Stewart, W., and Lightfood, E. (1960). *Transport Phenomena.* Wiley New York.

Bradshaw, P. (1971). *An Introduction to Turbulence and its Measurements.* Pergamon Press Oxford.

Browne, L. and Dinkelacker, A. (1995). Turbulent pipe flow: pressures and velocities. *Fluid Dynamics Research*, **vol. 15**, pp. 177–204.

Deelder, B. (2001). *Measurements on the turbulent flow around and through monoliths for application in a monolith stirred reactor, MSc Thesis.* Kramers laboratorium voor Fysische Technologie, Delft University of Technology, Delft.

DeGraaff, D. (1999). *Reynolds number scaling of the turbulent boundary layer on a flat plate and on swept and unswept bumps, PhD Thesis.* Stanford University.

Deshpande, M. and Giddens, D. (1980). Turbulence measurements in a constricted tube. *Journal of Fluid Mechanics*, **vol. 97**, pp. 65–89.

Drain, L. (1980). *The Laser Doppler Technique.* John Wiley and Sons.

Durst, F., Whitelaw, J., and Melling, A. (1976). *Principles and practice of Laser Doppler Anemometry.* Academic Press, New York.

Fay, J. (1994). *Introduction to Fluid Mechanics.* MIT Press Cambridge.

Gersten, K. and Herwig, H. (1992). *Stroemungsmechanik.* Vieweg und Son Verlagsgesellschaft Braunschweig.

Hinze, J. (1975). *Turbulence, 2nd edition.* McGraw-Hill New York.

Janssen, L. and Warmoeskerken, M. (1987). *Data Phenomena data companion.* Delftse Universitaire Pers Delft.

Laufer, J. (1954). *The structure of turbulence in fully developed pipe flow, report 1174.* National Advisory Committee for Aeronautics.

Loseke, K. and Gould, R. (1991). A comparison of velocity bias correction techniques in laser doppler velocimetry. *ASME Fluid Measurement and Instrumentation Forum*, **FED-Vol. 108**, pp. 63–68.

March, J. (1998). The calibration of a turbine meter as a secondary flow-rate standard by a one-point relative method using laser doppler velocimetry. *Measurement Science and Technology*, **vol. 9**, pp. 129–132.

McLaughlin, D. and Tiederman, W. (1973). Biasing correction for individual realizations of laser anemometer measurements in turbulent flows. *The Physics of Fluids*, **vol. 16**, pp. 2082–2088.

Mehta, R. and Bradshaw, P. (November 1979). Design rules for small low speed wind tunnels. *Aeronautical Journal*.

Nieuwstadt, F. (1998). *Turbulentie*. Epsilon Uitgaven Utrecht.

Nievaart, V. (2000). *Improvement and tailoring for near-wall turbulence measurements in a venturi, MSc Thesis*. Kramers laboratorium voor Fysische Technologie, Delft University of Technology, Delft.

Nikuradse, J. (1932). Gesetzmaessigkeiten der turbulenten stroemung in glatten rohren. *Forschung auf dem Gebiete des Ingenieurswesens*, **Ausgabe B Band 3 Forschungsheft 356**.

Okwuobi, P. and Azad, R. (1973). Turbulence in a conical diffuser with fully developed flow at entry. *Journal of Fluid Mechanics, vol. 57, part 3, pp. 603-622.*

Pope, S. (2000). *Turbulent flows*. Cambridge University Press.

Portela, L. (1998). *Identification and Characterization of Vortices in the Turbulent Boudary Layer, PhD Thesis*. Stanford University Press.

Schlichting, H. (1965). *Grenzschicht Theorie*. Verlag G. Braun Karlsruhe.

Singh, R. and Azad, R. (1995). The structure of instantaneous reversals in highly turbulent flows. *Experiments in Fluids*, **vol.18**, pp. 409–420.

Spencer, E., Heitor, M., and Castro, I. (1995). Intercomparison of measurements and computations of flow through a contraction and a diffuser. *Flow Measurements Instruments*, **vol. 6, No.1**, pp. 3–14.

Tennekes, H. and Lumley, J. (1972). *A first course in turbulence*. The MIT Press Cambridge.

Townsend, A. (1956). *The structure of turbulent shear flows*. Cambridge University Press.

Trupp, A., Azad, R., and Kassab, S. (1986). Near-wall velocity distributions within a straight conical diffuser. *Experiments in Fluids*, **vol. 4**, pp. 319–331.

TSI (1990). *Optical Components*. TSI Inc., St. Paul.

TSI (1992). *IFA750, Instruction Manual, version 3.5*. TSI Inc., St. Paul.

Tummers, M., Passchier, D., and Henkes, R. (1997). Experimental investigation of an adverse pressure gradient wake and comparison with calculations. *Experimental Thermal and Fluid Science*, **vol. 14**, pp. 17–24.

Van Maanen, H. (1999). *Retrieval of Turbulence and Turbulence Properties from Randomly Sampled Laser-Doppler Anemometry Data with Noise, PhD Thesis*. Delft University of Technology, Delft, Hans R.E. van Maanen.

Van Maanen, H. (2000). *Doppler Signal Processors and Signal Processing for Laser Doppler Anemometry.* J.M. Burgerscentrum, Delft University.

Zhang, Z. (2002). Velocity bias in lda measurements and its depence in the flow turbulence. *Flow Measurement and Instrumentation*, **vol. 13**, pp. 63–68.

Appendix A

Measurement parameters

Performing measurements with a LDA set-up brings on a lot of work. First, the laser beams have to be aligned, but also the settings of the processor, filters et cetera should be chosen accurately. Therefore, for every single measurement all parameters have to be checked. In this appendix only one value of each parameter will be given per traverse, for individual measurements this value can slightly differ. All LDA measurements were performed in back scatter mode.

In general, the number of data points close to the wall ($y/R < 0.02$) are in the order of 250k, increasing to a total value of 450k data points for measurement locations at $y/R > 0.10$. The data rate varies between 300 very close to the wall to 900Hz for $y/R > 0.10$. The chosen number of half cycles (after this amount the burst is called a measurement) had the maximum value of 8. Some other 'general' properties for all traverse measurements about the settings of the LDA set-up are listed in table A.1.

Table A.1: General settings of the LDA equipment

	λ laser beam (nm)	f_{shift} (MHz)	range frequency filter
axial	514.5	2.0	300 kHz - 3.0 MHz
tangential	488.0	1.0	300 kHz - 3.0 MHz

In order to keep the thin sheet mounted in the throat of the venturi and diffuser, the box around the throat of the venturi should be brought to a lower pressure than the atmospherical pressure. Usually, a under pressure of $0.15 \cdot 10^5$ Pa is sufficient.

The next tables, A.2 and A.3, show the applied lenses, some characteristic velocities and scales.

The friction velocity is calculated with formula 2.13, where λ_{fr} has a value of 0.0156, which is the friction factor for a smooth pipe. The closer the value of U/u_{max} is to 1, the flatter is the axial velocity profile.

Table A.2: Measurement parameters of the flow and LDA set-up of every traverse

	pipe	1Dup	throat	diffuser	0Ddown
$F_{lens}(mm)$	250	250	122.2	122.2	250
Re, upstream (·100)	190	196	180	196	196
U(m/s)	1.91	1.97	4.99	3.09	1.97
u^* (mm/s)	84.3	87.0	220.3	136.5	87.0
$\overline{u}_{max}$ (m/s)	2.19	2.22	5.02	3.42	3.10
$U/\overline{u}_{max}$	0.87	0.89	0.99	0.90	0.64

Table A.3: Measurement parameters of the flow and LDA set-up of every traverse, continuation

	2Ddown	3Ddown	4Ddown	5Ddown
$F_{lens}(mm)$	250	250	250	250
Re, upstream (·100)	196	196	196	196
U(m/s)	1.97	1.97	1.97	1.97
u^* (mm/s)	87.0	87.0	87.0	87.0
$\overline{u}_{max}$ (m/s)	2.74	2.49	2.32	2.09
$U/\overline{u}_{max}$	0.72	0.79	0.85	0.94

Appendix B

Diagnostic tools

In this appendix, an example of the application of the six mentioned diagnostic tools of section 6.1 is given. These tools have been applied on a measurement at $y/R = 0.01$ and 1.0 at 4D downstream.

The time-velocity diagrams (figure B.1) both look well, the velocity does not make strange 'excursions'.

The probability density functions (figures B.2 and B.3) show a small trend towards lower velocities close to the wall (in contrast to the throat, see figure D.7) and higher velocities at the centerline.

Both measurements do not suffer from multiple validation or the dead time of the processor, considering the straight decreasing development of the time between data diagrams (figure B.4).

The slopes in the auto correlation functions is declining in figure B.5. Both have a small, though clear noise peak.

At last, the number of products in the slotted auto correlation function are shown in figure B.6. As the average number of products is directly proportional to the data rate and the total number of data points(eq. 6.1), it is clear that N_p has a higher value in figure B.6*b*.

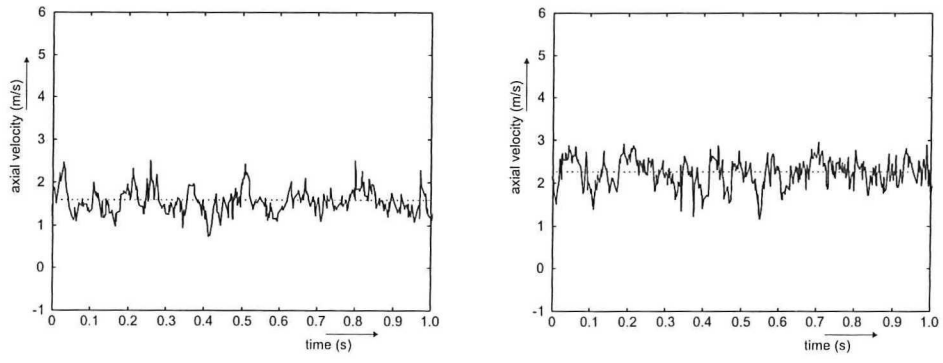

(a) wall, $y/R = 0.01$ (b) centerline, $y/R = 1.0$

Figure B.1: Time-velocity diagrams 4D downstream, upstream $Re = 196 \cdot 10^3$

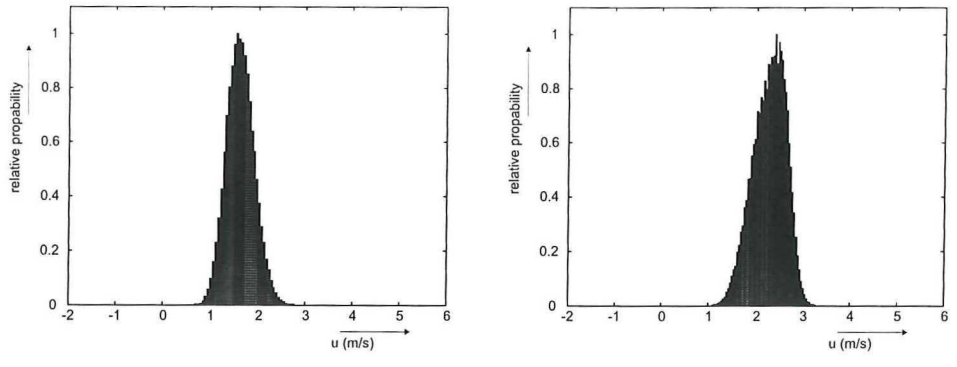

(a) wall, $y/R = 0.01$ (b) centerline, $y/R = 1.0$

Figure B.2: Linear probability density functions 4D downstream, upstream $Re = 196 \cdot 10^3$

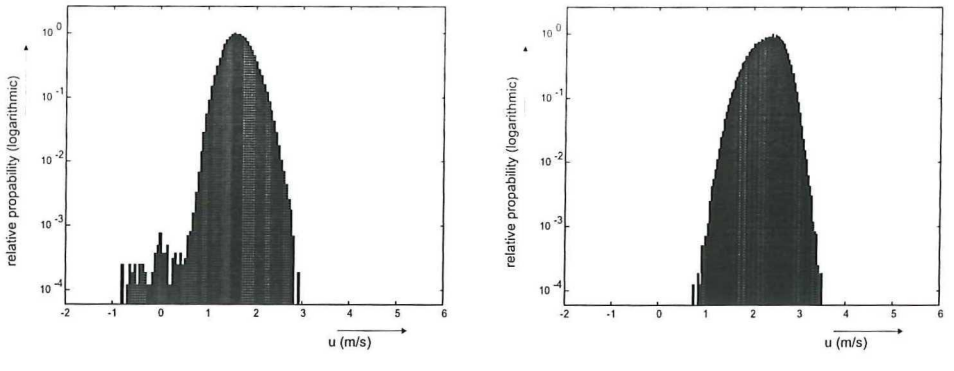

(a) wall, $y/R = 0.01$ (b) centerline, $y/R = 1.0$

Figure B.3: Logarithmic probability density functions 4D downstream, upstream $Re = 196 \cdot 10^3$

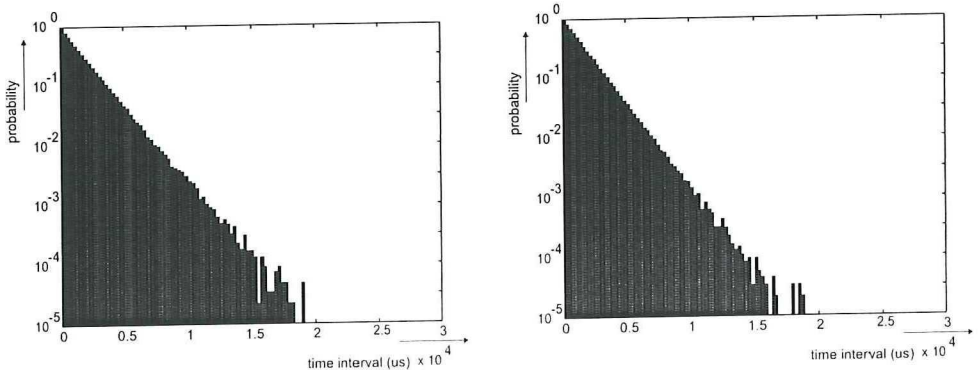

(a) wall, $y/R = 0.01$

(b) centerline, $y/R = 1.0$

Figure B.4: Time between data diagrams 4D downstream, upstream $Re = 196 \cdot 10^3$

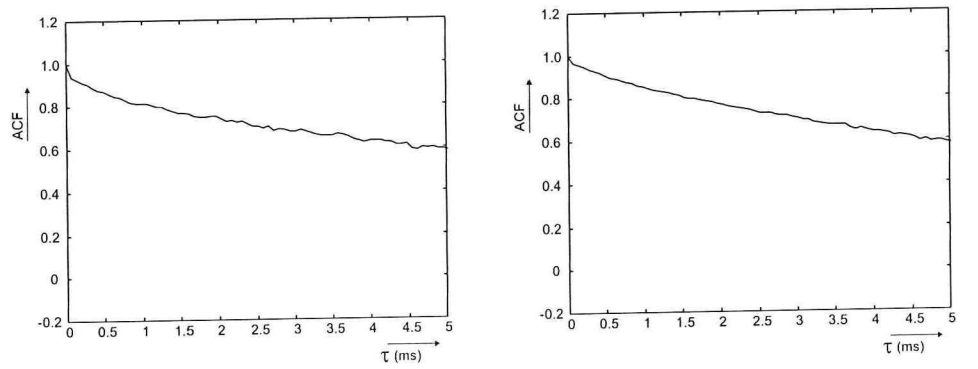

(a) wall, $y/R = 0.01$

(b) centerline, $y/R = 1.0$

Figure B.5: Auto correlation functions 4D downstream, upstream $Re = 196 \cdot 10^3$

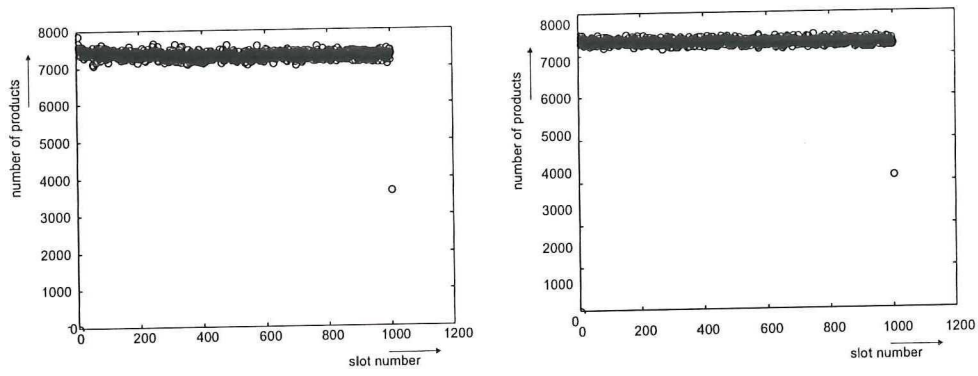

(a) wall, $y/R = 0.01$

(b) centerline, $y/R = 1.0$

Figure B.6: Number of products in the slotted ACF 4D downstream, upstream $Re = 196 \cdot 10^3$

Appendix C

Time-velocity diagrams

The following figures represent the time-velocity diagrams of each measurement location for three positions from the wall (y/R = 0.01, 0.1 and 1.0, respectively). The mean velocity, corrected for velocity bias, is indicated by a dashed line in every figure.

C.1: pipe flow
C.2: 1D upstream
C.3: throat venturi
C.4: diffuser
C.5: 0D downstream
C.6: 2D downstream
C.7: 3D downstream
C.8: 4D downstream
C.9: 5D downstream

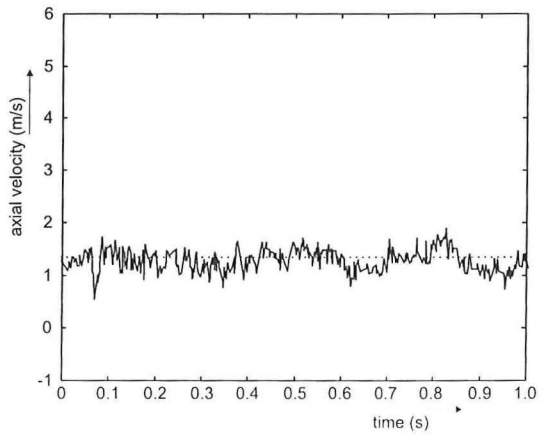

(a) y/R = 0.01

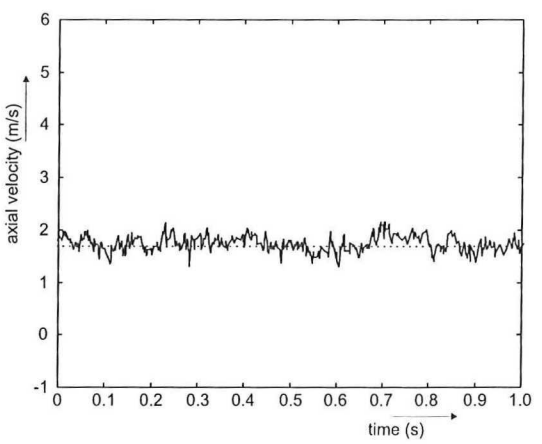

(b) y/R = 0.1

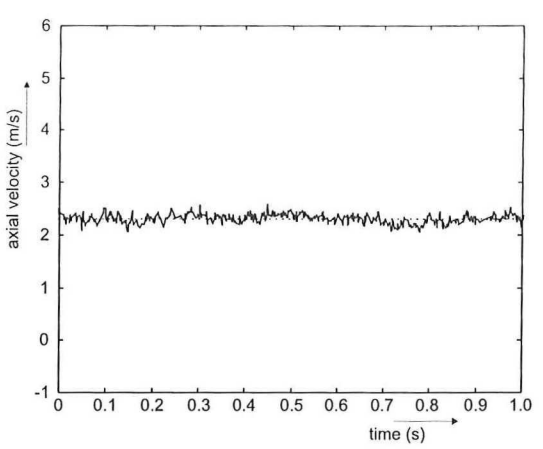

(c) y/R = 1.0

Figure C.1: Time velocity diagrams for pipe flow, $Re = 190 \cdot 10^3$

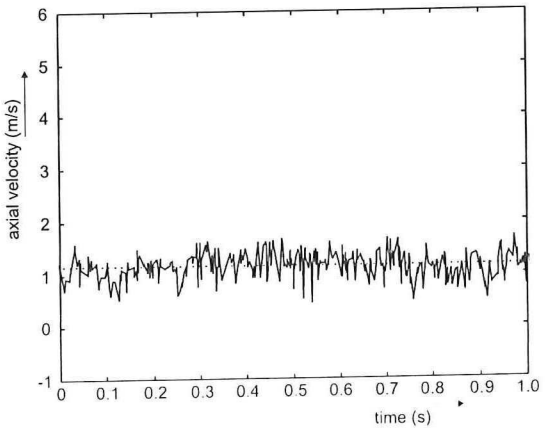

(a) y/R = 0.01

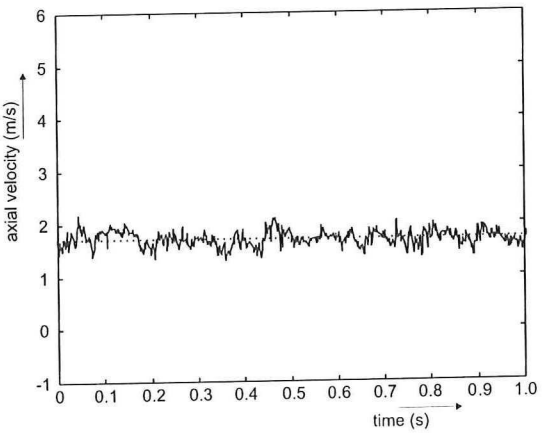

(b) y/R = 0.1

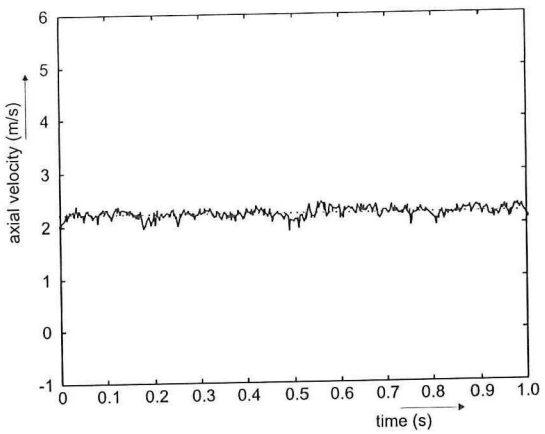

(c) y/R = 1.0

Figure C.2: Time velocity diagrams 1D upstream, $Re = 196 \cdot 10^3$

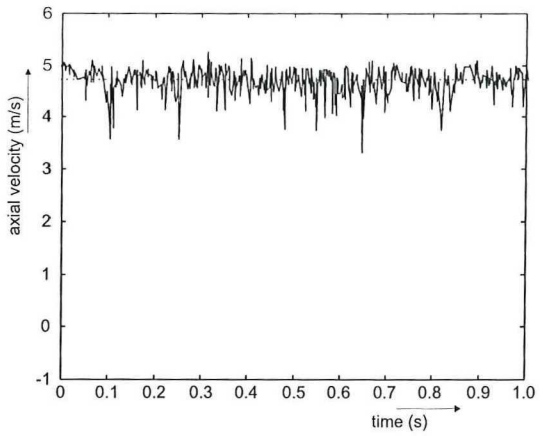

(a) y/R = 0.01

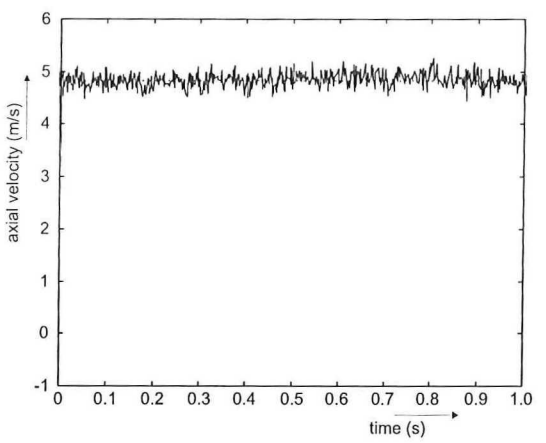

(b) y/R = 0.1

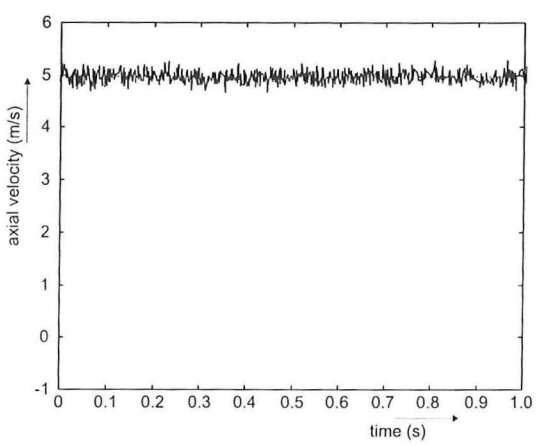

(c) y/R = 1.0

Figure C.3: Time velocity diagrams in the throat, $Re = 298 \cdot 10^3$

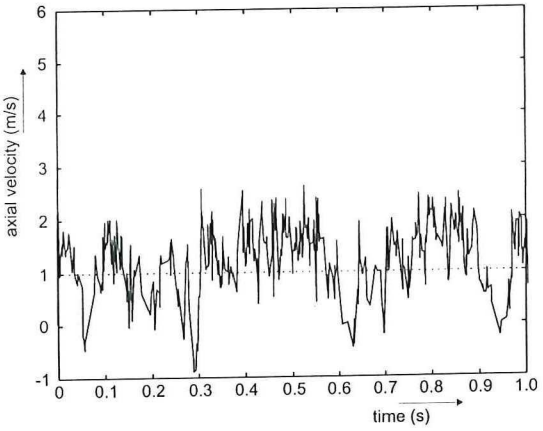

(a) y/R = 0.01

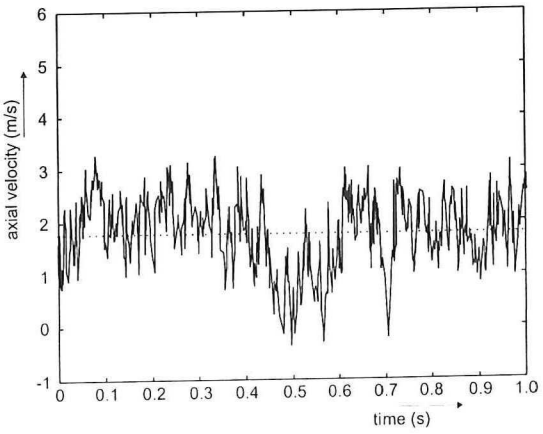

(b) y/R = 0.1

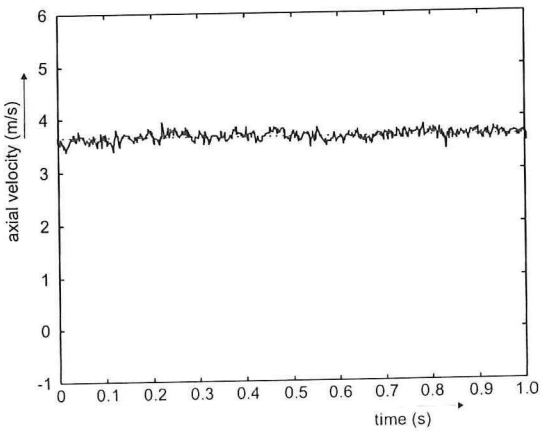

(c) y/R = 1.0

Figure C.4: Time velocity diagrams in the diffuser, $Re = 246 \cdot 10^3$

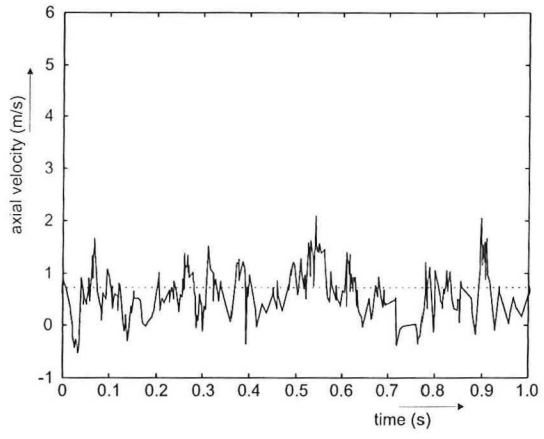

(a) y/R = 0.01

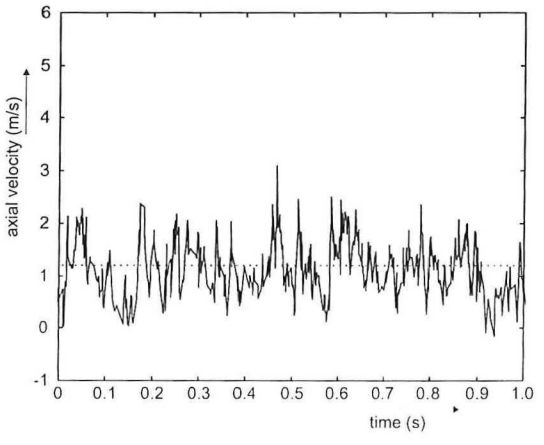

(b) y/R = 0.1

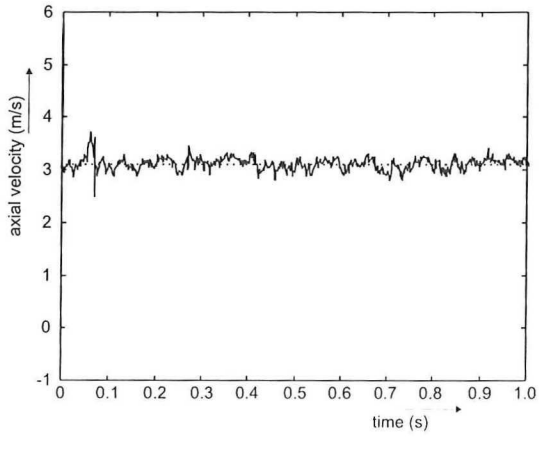

(c) y/R = 1.0

Figure C.5: Time velocity diagrams 0D downstream, $Re = 196 \cdot 10^3$

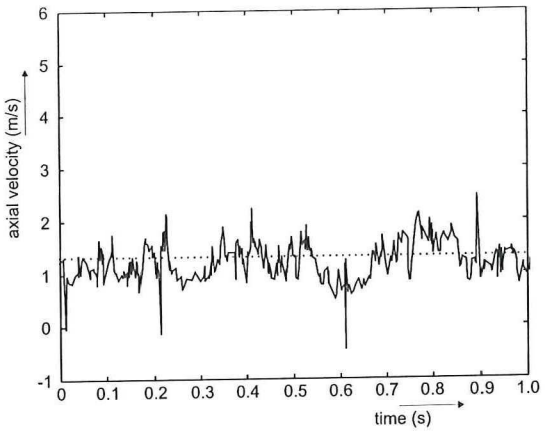

(a) y/R = 0.01

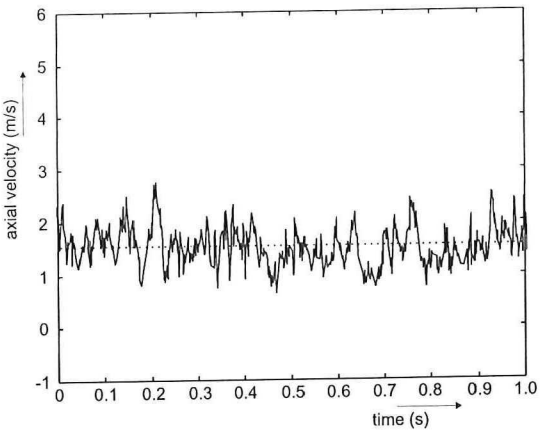

(b) y/R = 0.1

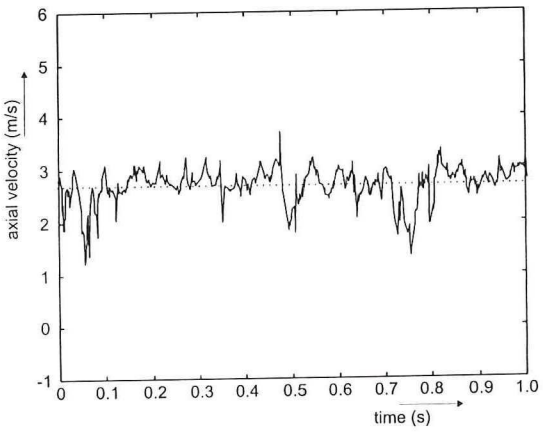

(c) y/R = 1.0

Figure C.6: Time velocity diagrams 2D downstream, $Re = 196 \cdot 10^3$

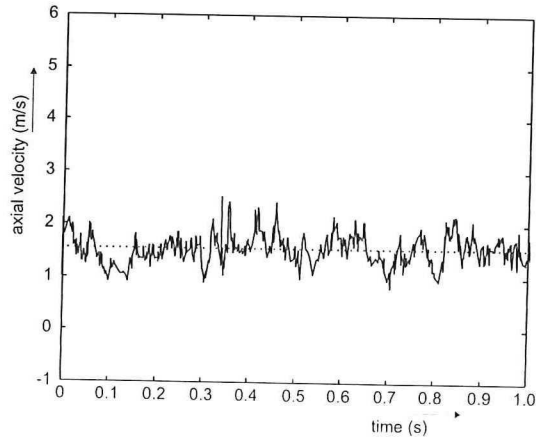

(a) y/R = 0.01

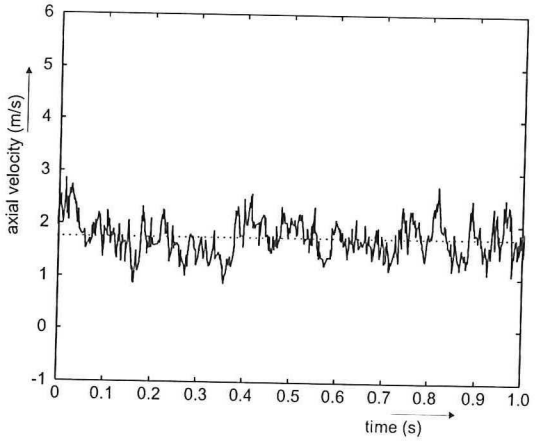

(b) y/R = 0.1

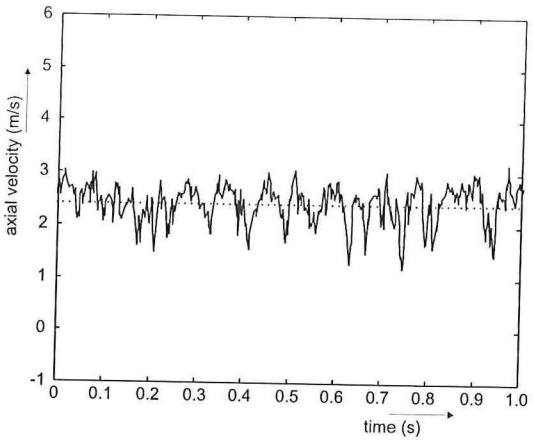

(c) y/R = 1.0

Figure C.7: Time velocity diagrams 3D downstream, $Re = 196 \cdot 10^3$

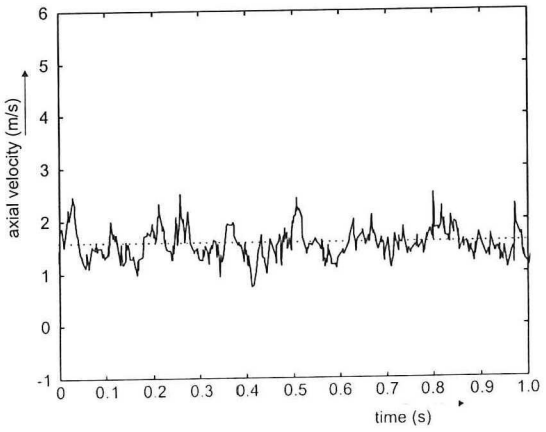

(a) y/R = 0.01

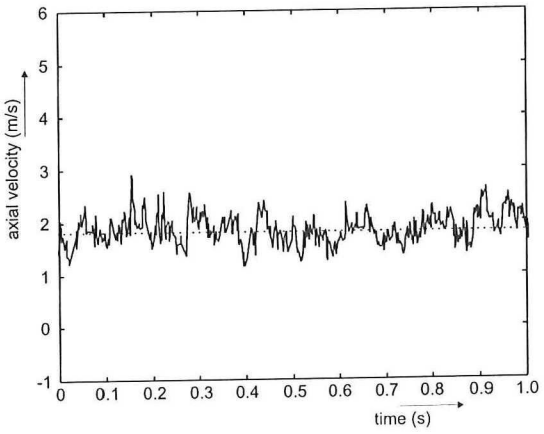

(b) y/R = 0.1

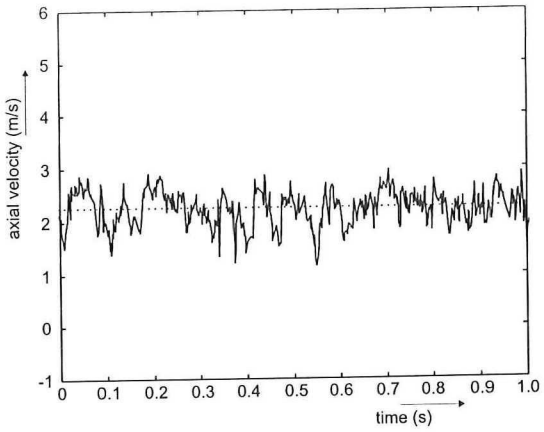

(c) y/R = 1.0

Figure C.8: Time velocity diagrams 4D downstream, $Re = 196 \cdot 10^3$

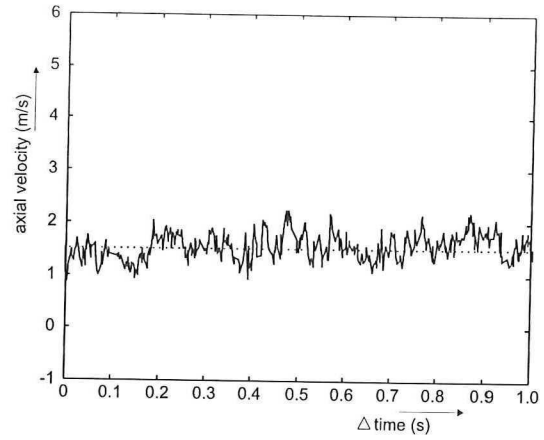

(a) y/R = 0.01

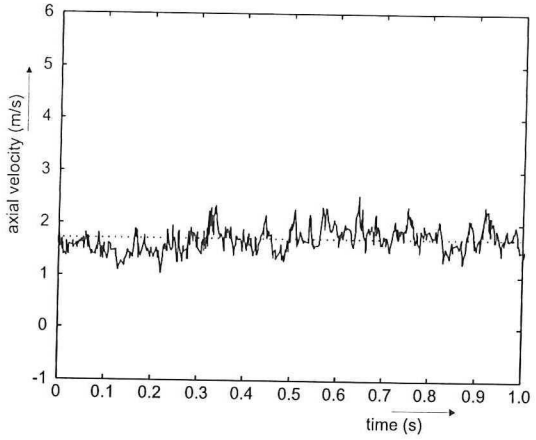

(b) y/R = 0.1

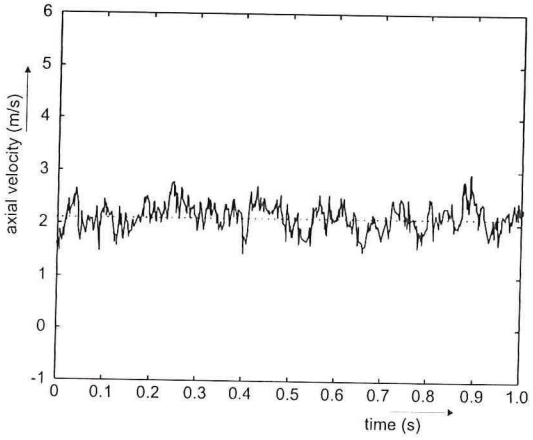

(c) y/R = 1.0

Figure C.9: Time velocity diagrams 5D downstream, $Re = 196 \cdot 10^3$

Appendix D

Probability density functions

The following figures represent the linear and logarithmic probability density functions of each measurement location for three positions from the wall ($y/R = 0.01$, 0.1 and 1.0, respectively).

D.1 to D.3	:	pipe flow
D.4 to D.6	:	1D upstream
D.7 to D.9	:	throat venturi
D.10 to D.12	:	diffuser
D.13 to D.15	:	0D downstream
D.16 to D.18	:	2D downstream
D.19 to D.21	:	3D downstream
D.22 to D.24	:	4D downstream
D.25 to D.27	:	5D downstream

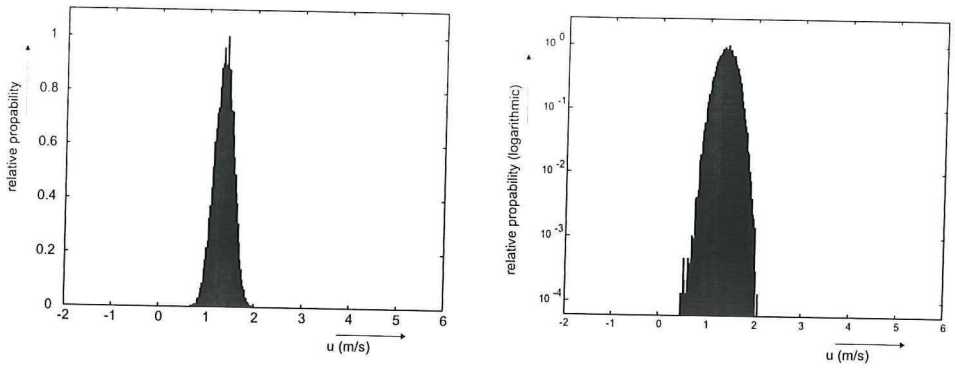

(a) Linear (b) Logarithmic

Figure D.1: Velocity PDF pipe flow at $y/R = 0.01$, $Re = 190 \cdot 10^3$

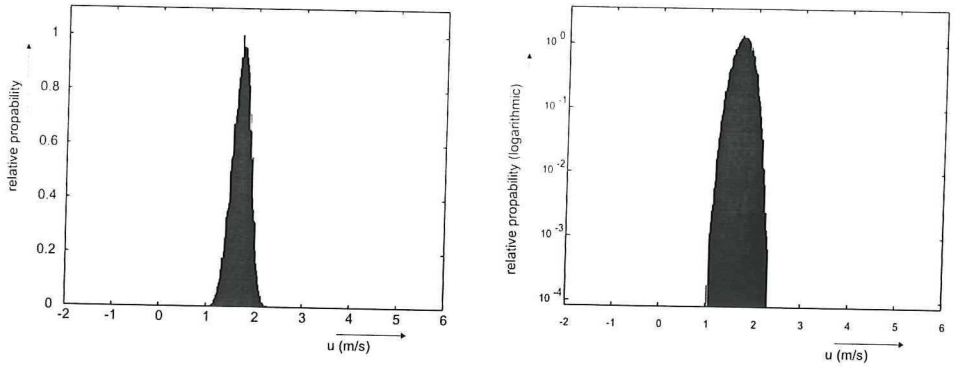

(a) Linear (b) Logarithmic

Figure D.2: Velocity PDF pipe flow at $y/R = 0.1$, $Re = 190 \cdot 10^3$

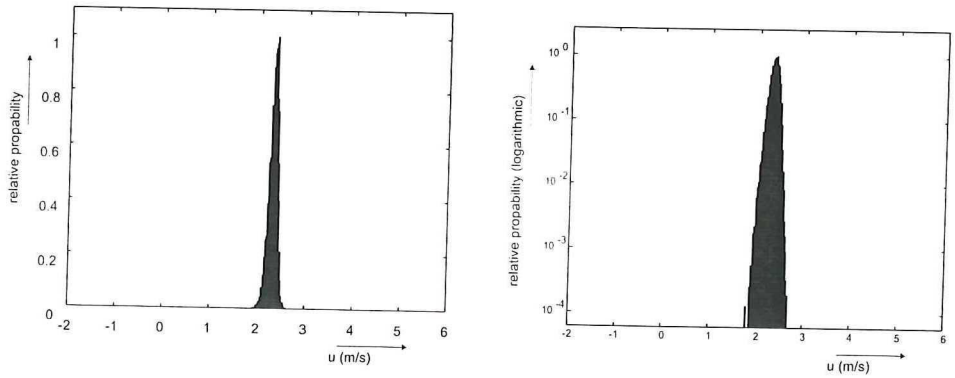

(a) Linear (b) Logarithmic

Figure D.3: Velocity PDF pipe flow at $y/R = 1.0$, $Re = 190 \cdot 10^3$

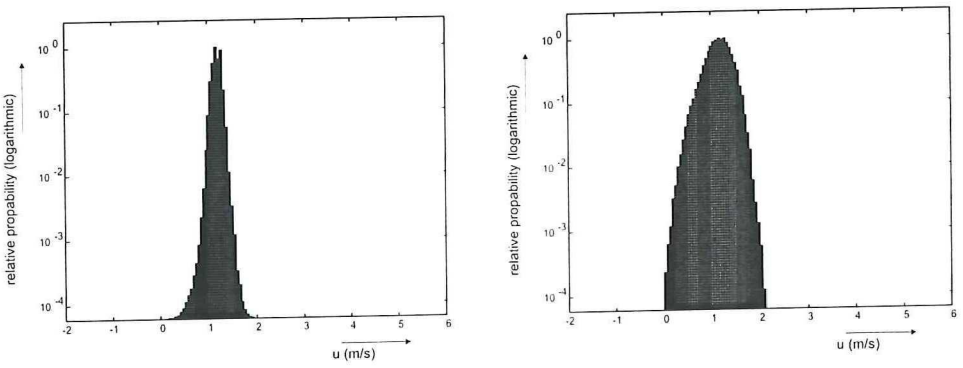

(a) Linear (b) Logarithmic

Figure D.4: Velocity PDF 1D upstream at $y/R = 0.01$, $Re = 196 \cdot 10^3$

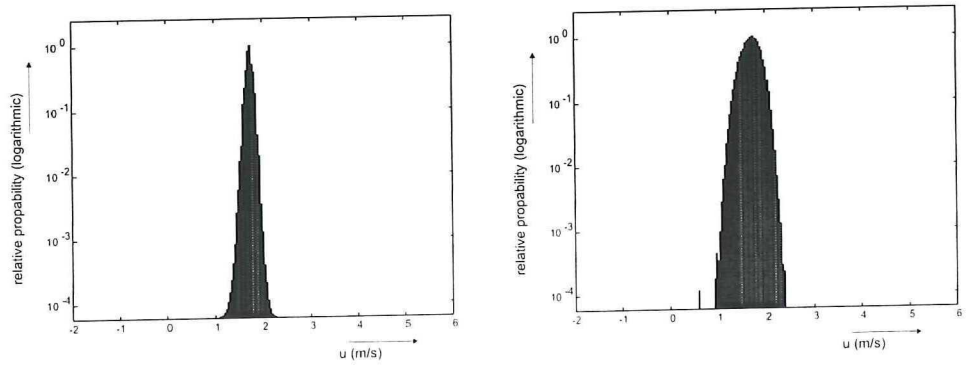

(a) Linear (b) Logarithmic

Figure D.5: Velocity PDF 1D upstream at $y/R = 0.1$, $Re = 196 \cdot 10^3$

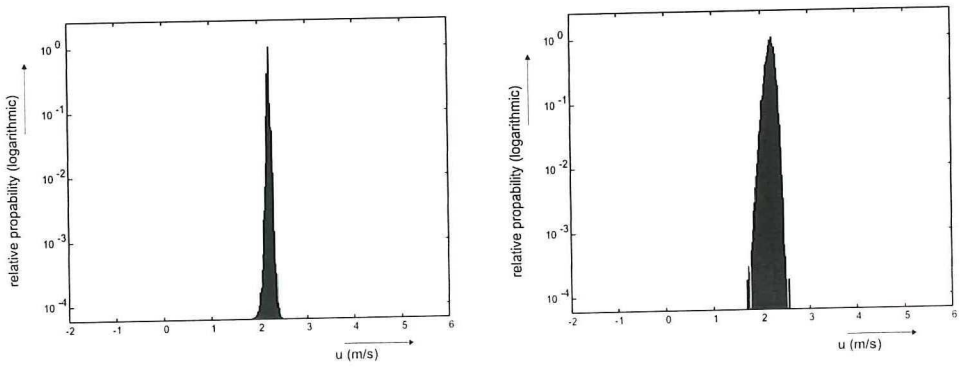

(a) Linear (b) Logarithmic

Figure D.6: Velocity PDF 1D upstream at $y/R = 1.0$, $Re = 196 \cdot 10^3$

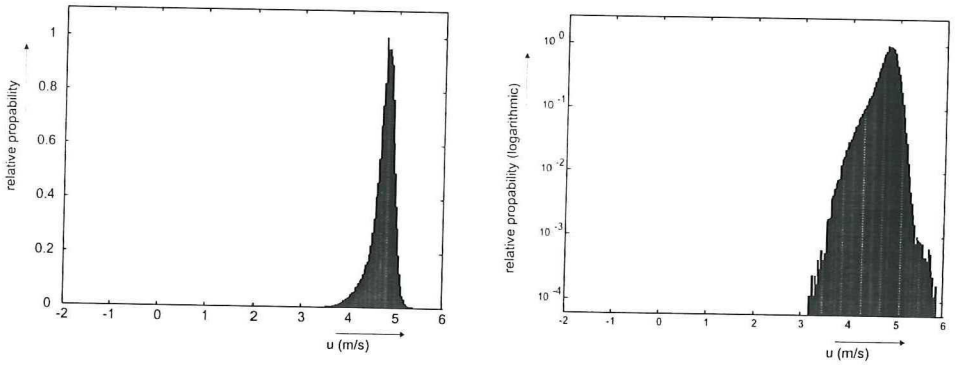

(a) Linear (b) Logarithmic

Figure D.7: Velocity PDF in the throat at $y/R = 0.01$, $Re = 298 \cdot 10^3$

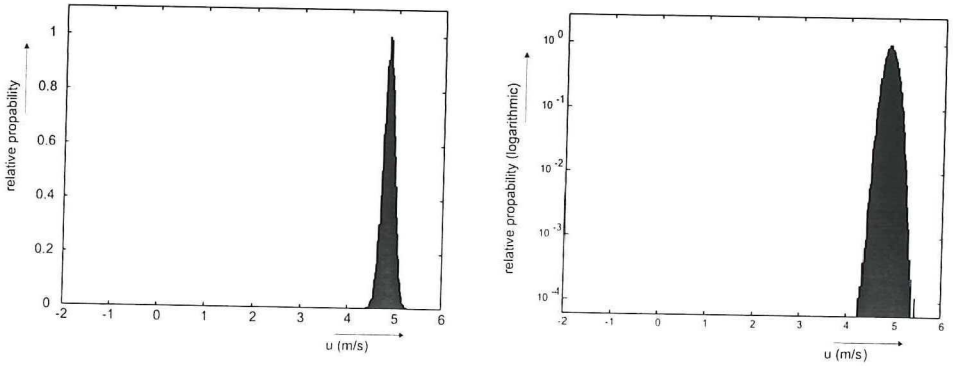

(a) Linear (b) Logarithmic

Figure D.8: Velocity PDF in the throat at $y/R = 0.1$, $Re = 298 \cdot 10^3$

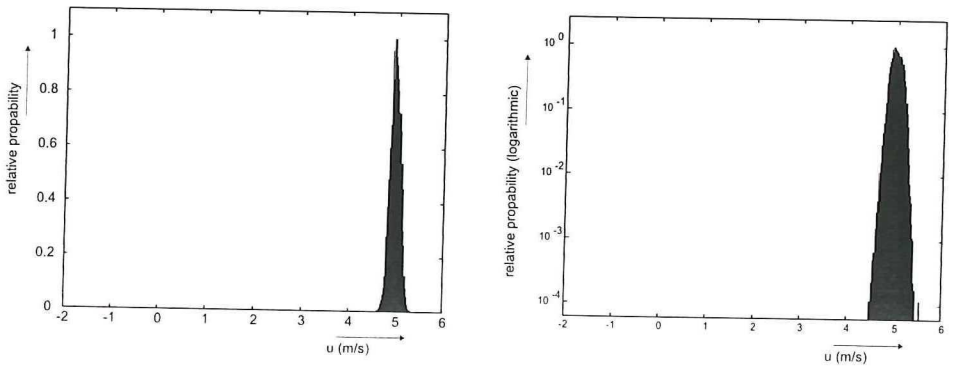

(a) Linear (b) Logarithmic

Figure D.9: Velocity PDF in the throat at $y/R = 1.0$, $Re = 298 \cdot 10^3$

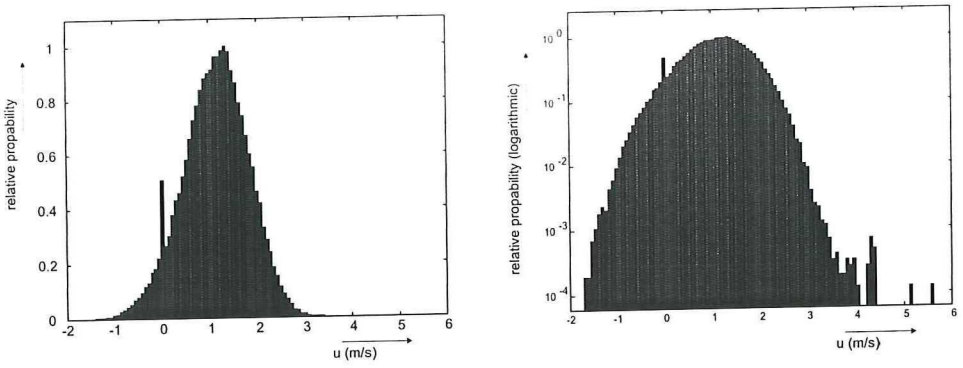

(a) Linear (b) Logarithmic

Figure D.10: Velocity PDF in the diffuser at $y/R = 0.01$, $Re = 246 \cdot 10^3$

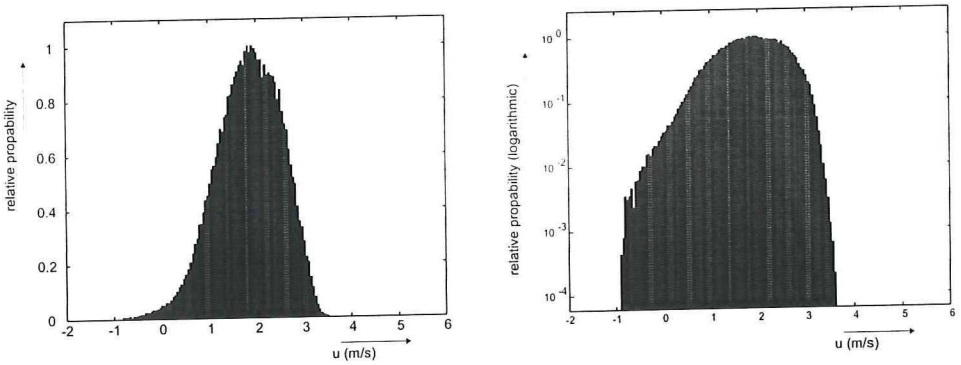

(a) Linear (b) Logarithmic

Figure D.11: Velocity PDF in the diffuser at $y/R = 0.1$, $Re = 246 \cdot 10^3$

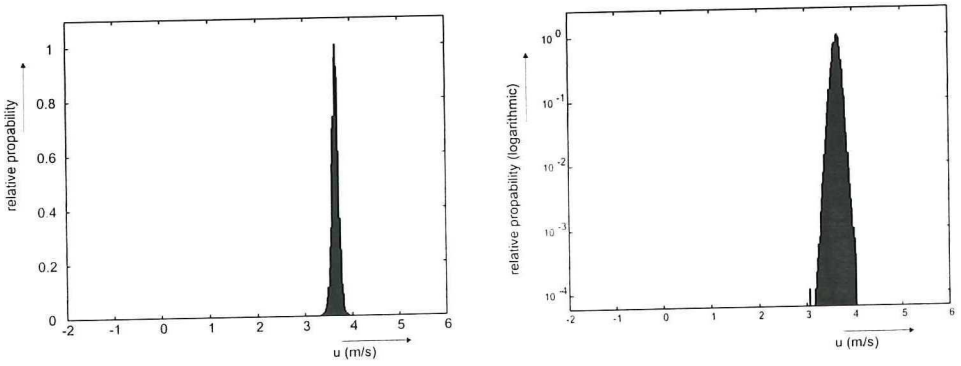

(a) Linear (b) Logarithmic

Figure D.12: Velocity PDF in the diffuser at $y/R = 1.0$, $Re = 246 \cdot 10^3$

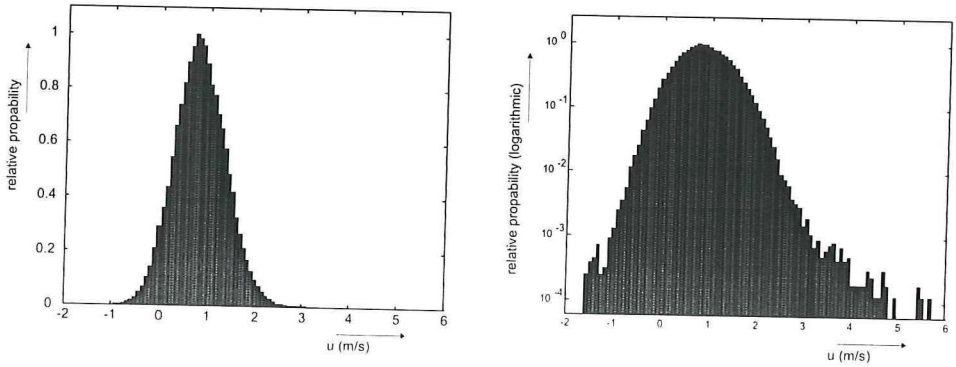

(a) Linear (b) Logarithmic

Figure D.13: Velocity PDF 0D downstream at $y/R = 0.01$, $Re = 196 \cdot 10^3$

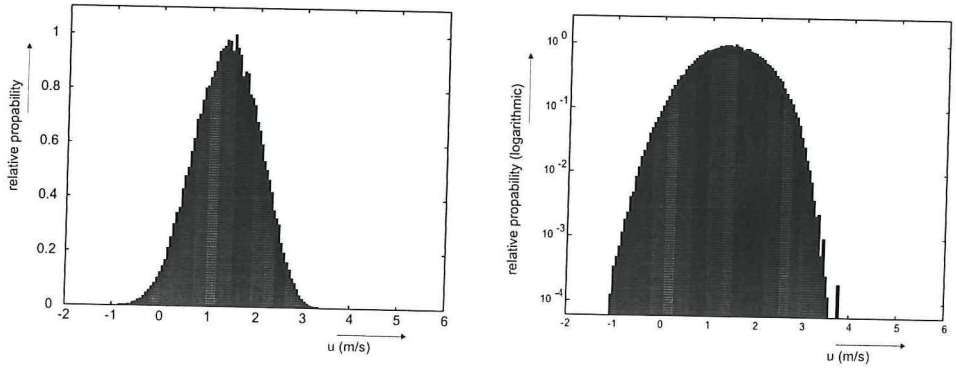

(a) Linear (b) Logarithmic

Figure D.14: Velocity PDF 0D downstream at $y/R = 0.1$, $Re = 196 \cdot 10^3$

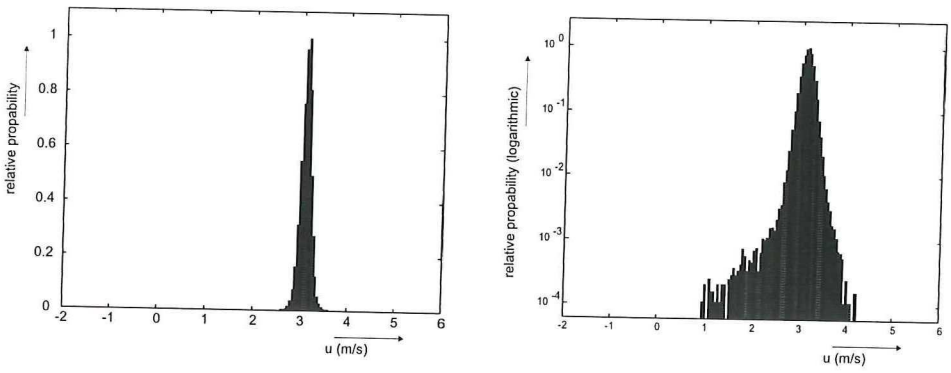

(a) Linear (b) Logarithmic

Figure D.15: Velocity PDF 0D downstream at $y/R = 1.0$, $Re = 196 \cdot 10^3$

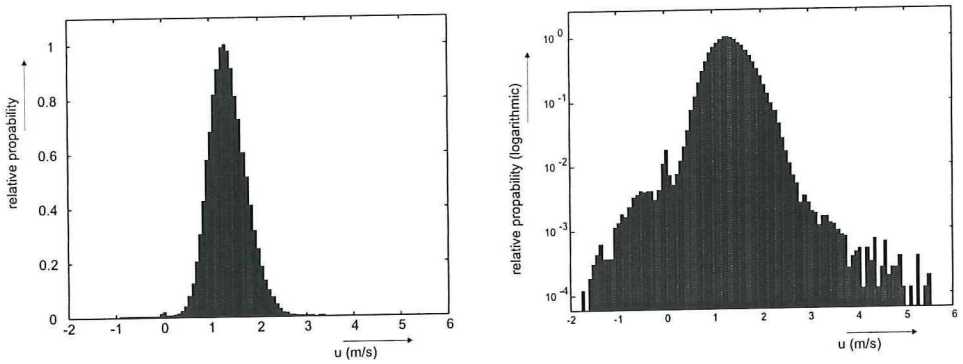

(a) Linear (b) Logarithmic

Figure D.16: Velocity PDF 2D downstream at $y/R = 0.01$, $Re = 196 \cdot 10^3$

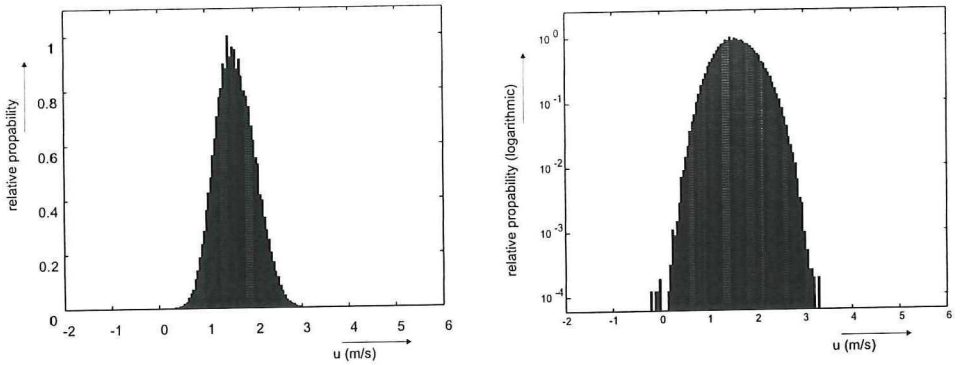

(a) Linear (b) Logarithmic

Figure D.17: Velocity PDF 2D downstream at $y/R = 0.1$, $Re = 196 \cdot 10^3$

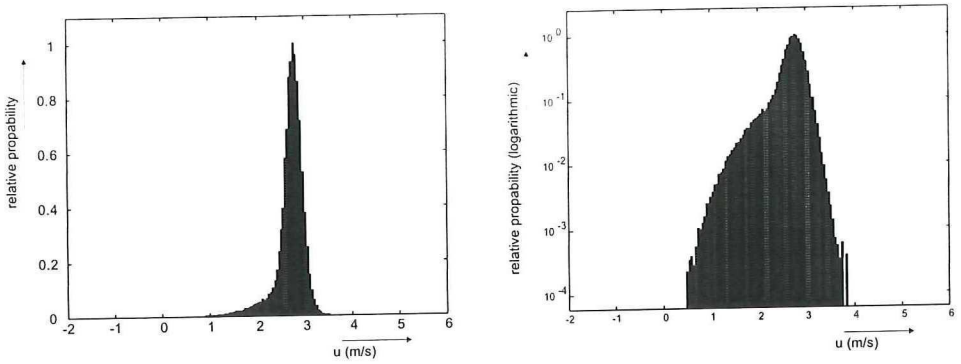

(a) Linear (b) Logarithmic

Figure D.18: Velocity PDF 2D downstream at $y/R = 1.0$, $Re = 196 \cdot 10^3$

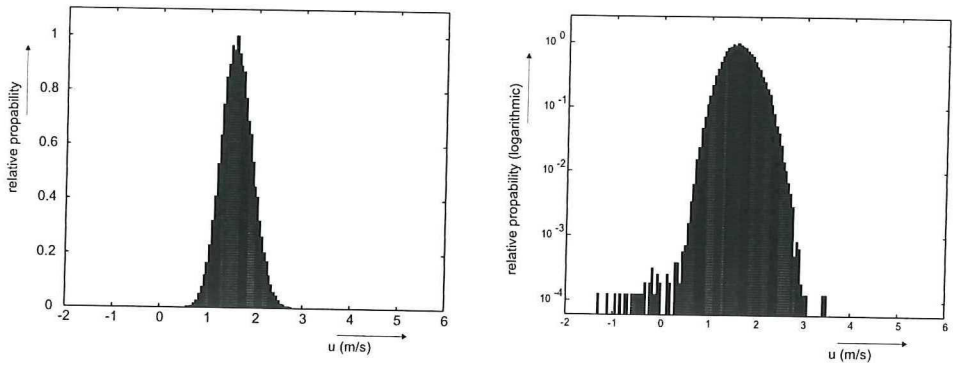

(a) Linear (b) Logarithmic

Figure D.19: Velocity PDF 3D downstream at $y/R = 0.01$, $Re = 196 \cdot 10^3$

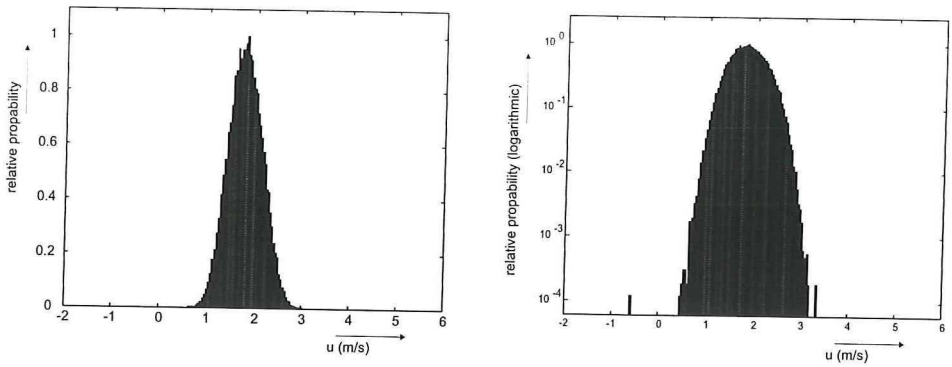

(a) Linear (b) Logarithmic

Figure D.20: Velocity PDF 3D downstream at $y/R = 0.1$, $Re = 196 \cdot 10^3$

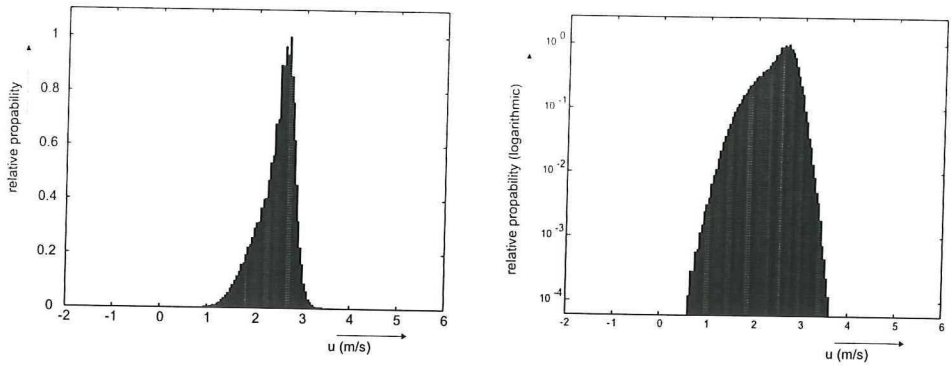

(a) Linear (b) Logarithmic

Figure D.21: Velocity PDF 3D downstream at $y/R = 1.0$, $Re = 196 \cdot 10^3$

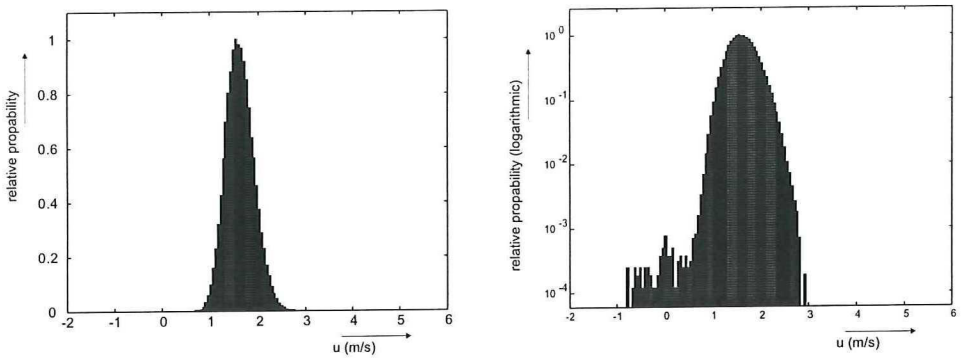

(a) Linear (b) Logarithmic

Figure D.22: Velocity PDF 4D downstream at $y/R = 0.01$, $Re = 196 \cdot 10^3$

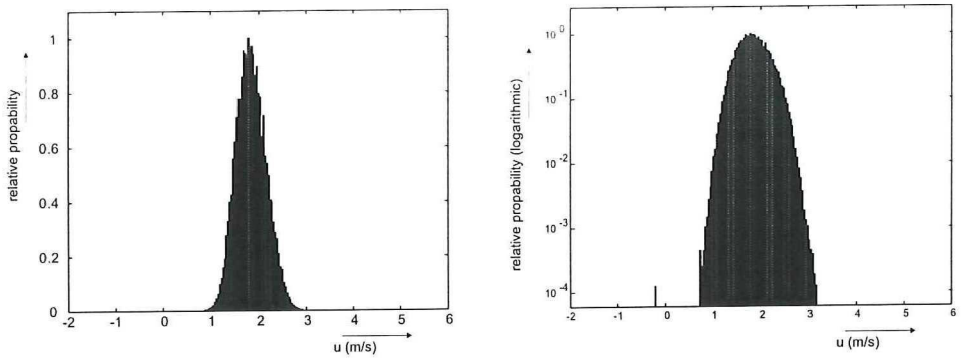

(a) Linear (b) Logarithmic

Figure D.23: Velocity PDF 4D downstream at $y/R = 0.1$, $Re = 196 \cdot 10^3$

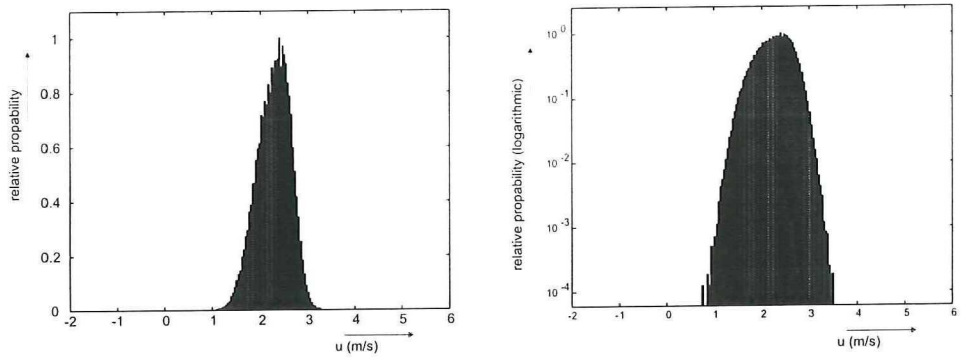

(a) Linear (b) Logarithmic

Figure D.24: Velocity PDF 4D downstream at $y/R = 1.0$, $Re = 196 \cdot 10^3$

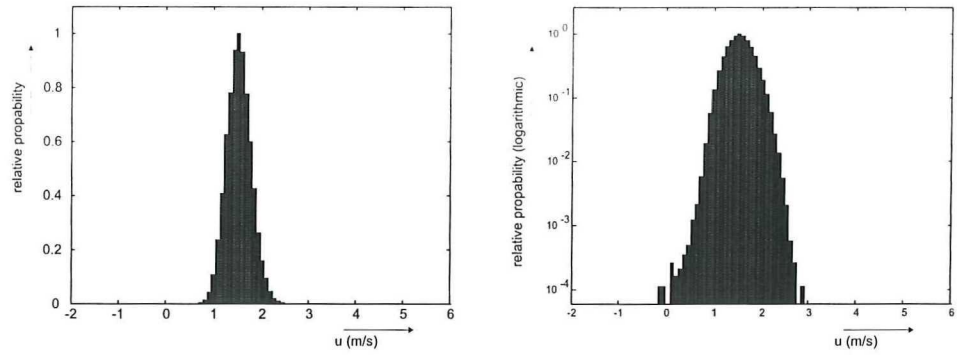

(a) Linear (b) Logarithmic

Figure D.25: Velocity PDF 5D downstream at $y/R = 0.01$, $Re = 196 \cdot 10^3$

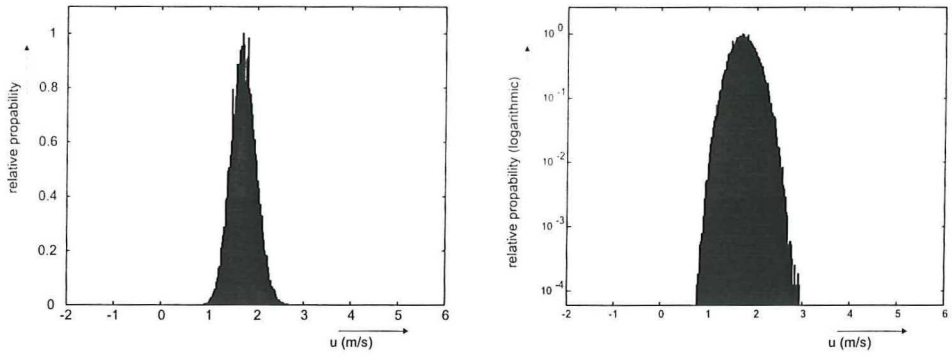

(a) Linear (b) Logarithmic

Figure D.26: Velocity PDF 5D downstream at $y/R = 0.1$, $Re = 196 \cdot 10^3$

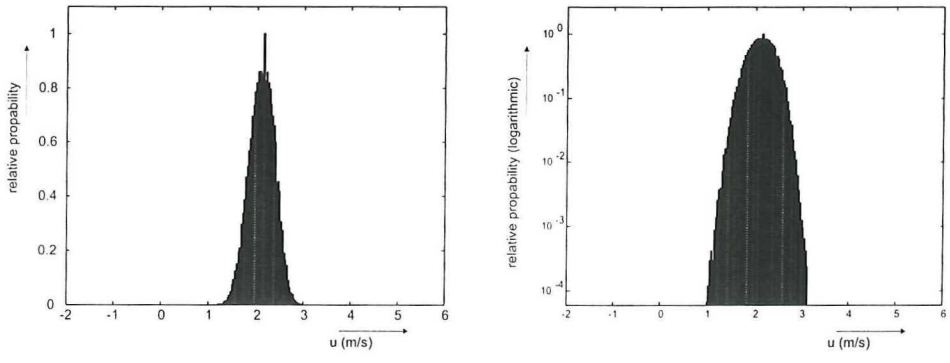

(a) Linear (b) Logarithmic

Figure D.27: Velocity PDF 5D downstream at $y/R = 1.0$, $Re = 196 \cdot 10^3$

Appendix E

Auto correlation functions

The following figures represent the auto correlation functions of each measurement location for three positions from the wall ($y/R = 0.01$, 0.1 and 1.0, respectively).

E.1: pipe flow
E.2: 1D upstream
E.3: throat venturi
E.4: diffuser
E.5: 0D downstream
E.6: 2D downstream
E.7: 3D downstream
E.8: 4D downstream
E.9: 5D downstream

Besides this figures, a table with the values of the (relative) turbulent fluctuations contributions and the signal to noise ratio of all given ACF's is included.

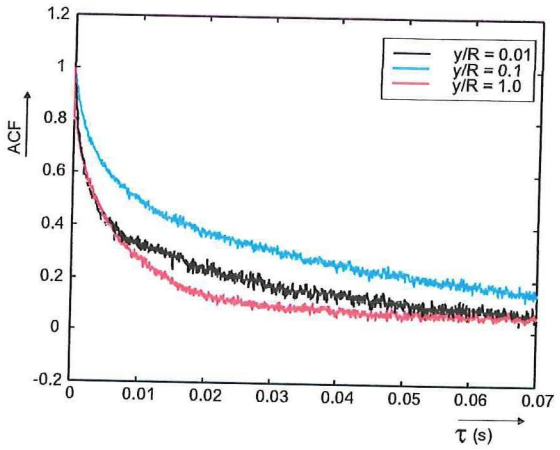

Figure E.1: ACF of a pipe flow for 3 positions from the wall, $Re = 190 \cdot 10^3$

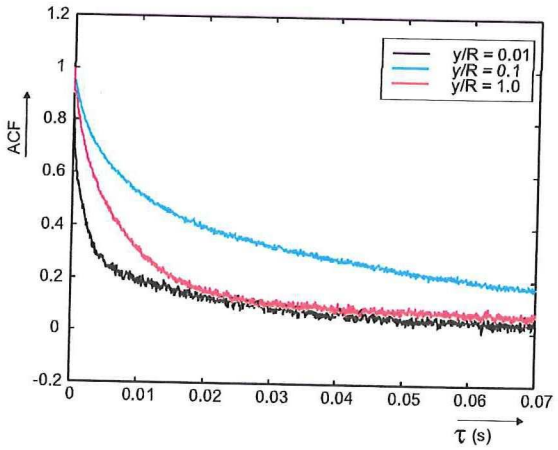

Figure E.2: ACF at 1D upstream for 3 positions from the wall, $Re = 196 \cdot 10^3$

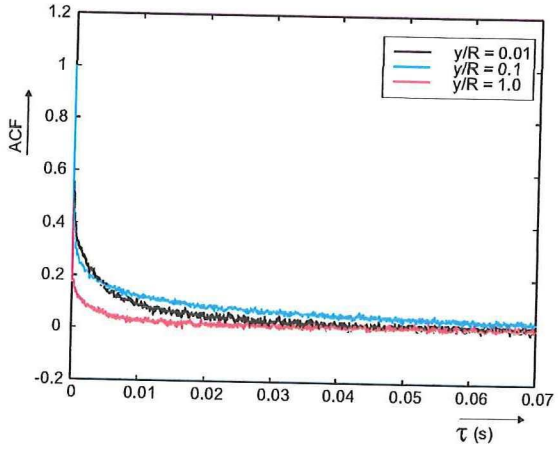

Figure E.3: ACF in the throat for 3 positions from the wall, $Re = 298 \cdot 10^3$

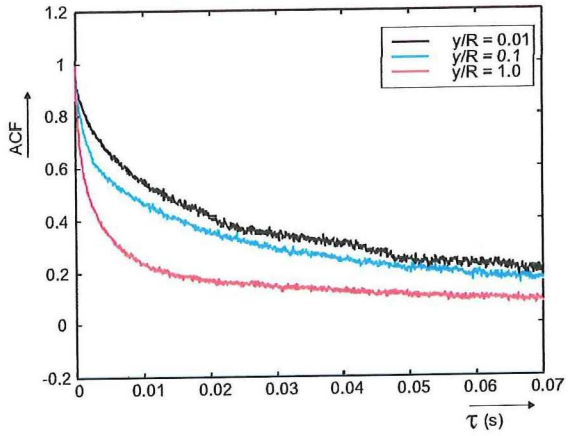

Figure E.4: ACF in the diffuser for 3 positions from the wall, $Re = 246 \cdot 10^3$

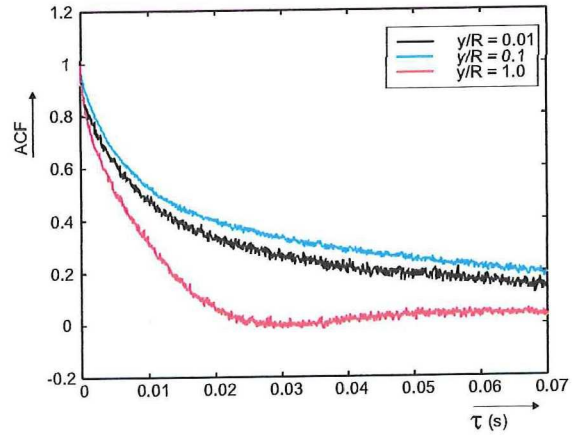

Figure E.5: ACF at 0D downstream for 3 positions from the wall, $Re = 196 \cdot 10^3$

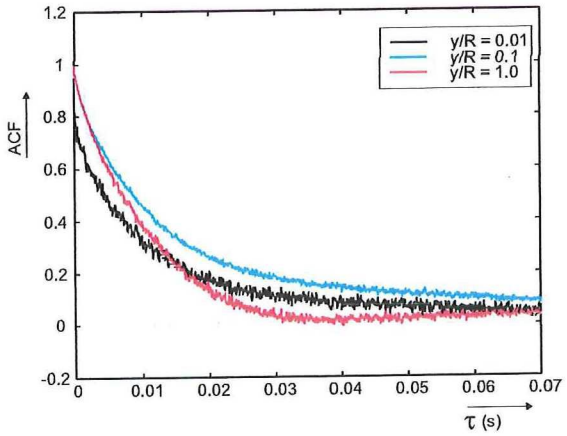

Figure E.6: ACF at 2D downstream for 3 positions from the wall, $Re = 196 \cdot 10^3$

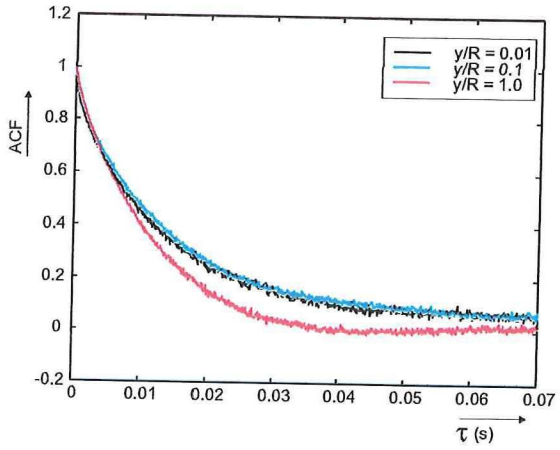

Figure E.7: ACF at 3D downstream for 3 positions from the wall, $Re = 196 \cdot 10^3$

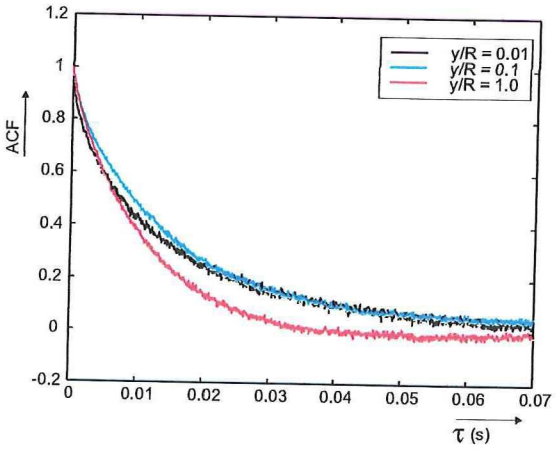

Figure E.8: ACF at 4D downstream for 3 positions from the wall, $Re = 196 \cdot 10^3$

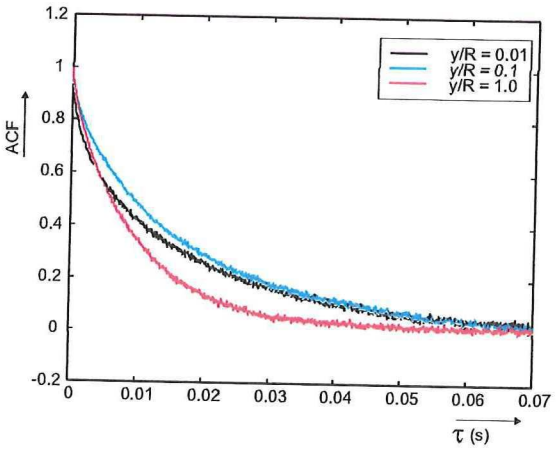

Figure E.9: ACF at 5D downstream for 3 positions from the wall, $Re = 196 \cdot 10^3$

In table E.1 the turbulent fluctuations contributions, B in figure 6.9, and the signal to noise ratio (SNR) are represented for all positions of the given ACF's.

Table E.1: Turbulent fluctuations contributions and SNR-values derived from the ACF

location	position	B axial	SNR axial	B tangential	SNR tangential
pipe	$y/R = 0.01$	0.942	4.01	0.882	2.73
	$y/R = 0.1$	0.968	5.53	0.961	4.96
	$y/R = 1.0$	0.803	2.02	0.726	1.63
1Dup	$y/R = 0.01$	0.828	2.20	0.927	3.58
	$y/R = 0.1$	0.947	4.22	0.908	3.15
	$y/R = 1.0$	0.905	3.08	0.761	1.78
throat	$y/R = 0.01$	0.572	1.16	0.603	1.23
	$y/R = 0.1$	0.480	0.961	0.727	1.63
	$y/R = 1.0$	0.174	0.459	0.496	0.992
diffuser	$y/R = 0.01$	0.937	3.87	0.983	7.51
	$y/R = 0.1$	0.952	4.44	0.928	3.60
	$y/R = 1.0$	0.863	2.51	0.800	2.00
0Ddown	$y/R = 0.01$	0.935	3.78	0.992	11.00
	$y/R = 0.1$	0.963	5.12	0.984	7.73
	$y/R = 1.0$	0.923	3.47	0.818	2.12
2Ddown	$y/R = 0.01$	0.827	2.19	0.989	9.38
	$y/R = 0.1$	0.960	4.91	0.985	8.19
	$y/R = 1.0$	0.952	4.45	0.956	4.68
3Ddown	$y/R = 0.01$	0.937	3.85	0.959	4.85
	$y/R = 0.1$	0.964	5.19	0.978	6.70
	$y/R = 1.0$	0.972	5.92	0.979	6.79
4Ddown	$y/R = 0.01$	0.937	3.84	0.980	7.03
	$y/R = 0.1$	0.965	5.28	0.985	7.97
	$y/R = 1.0$	0.966	5.34	0.975	6.26
5Ddown	$y/R = 0.01$	0.899	2.99	0.981	7.20
	$y/R = 0.1$	0.939	3.91	0.983	7.71
	$y/R = 1.0$	0.948	4.26	0.974	6.15

Appendix F

Power spectra

The following figures represent the power spectra of all measurement locations for three positions from the wall (y/R = 0.01, 0.1 and 1.0, respectively). In the subscript by each subfigure, the chosen value of k^* is given.

F.1: pipe flow
F.2: 1D upstream
F.3: throat venturi
F.4: diffuser
F.5: 0D downstream
F.6: 2D downstream
F.7: 3D downstream
F.8: 4D downstream
F.9: 5D downstream

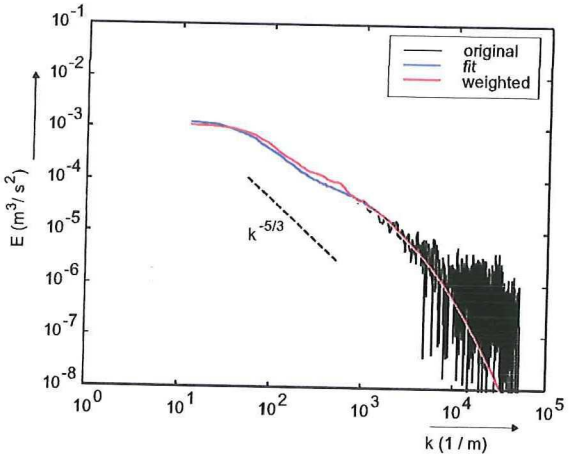

(a) y/R = 0.01, $k^* = 1300$

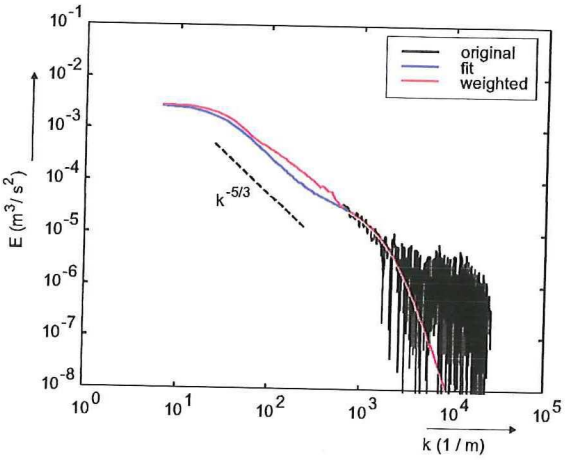

(b) y/R = 0.1, $k^* = 800$

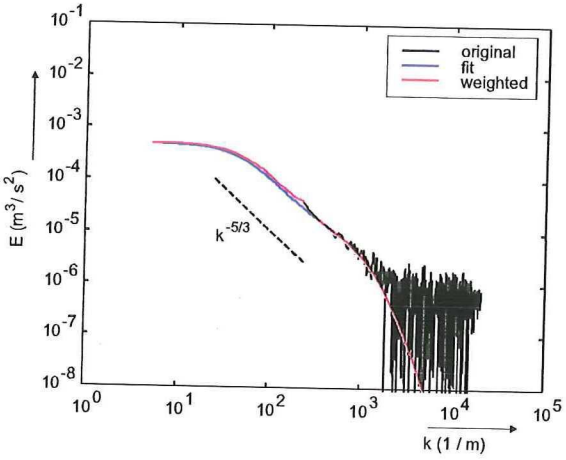

(c) y/R = 1.0, $k^* = 320$

Figure F.1: Power spectra for pipe flow, $Re = 190 \cdot 10^3$

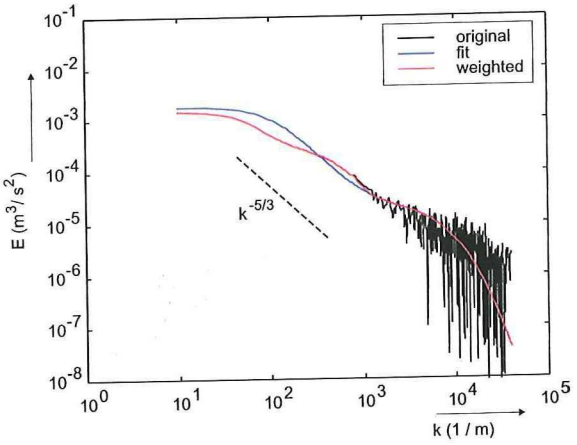

(a) y/R = 0.01, $k^* = 1150$

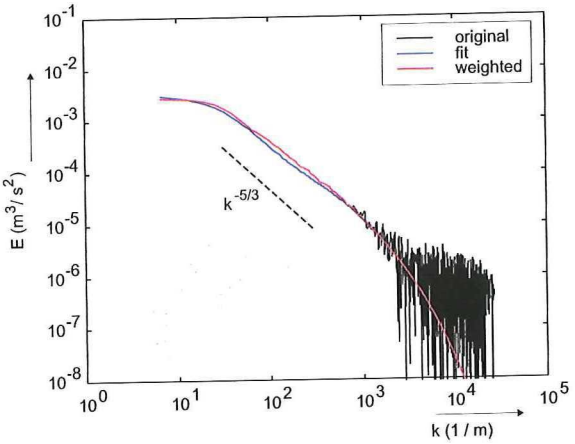

(b) y/R = 0.1, $k^* = 1000$

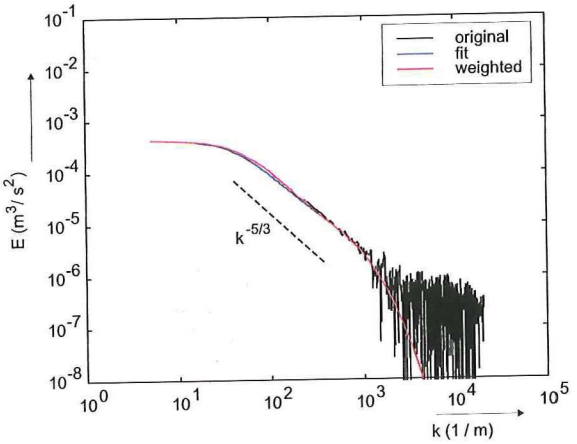

(c) y/R = 1.0, $k^* = 330$

Figure F.2: Power spectra 1D upstream, $Re = 196 \cdot 10^3$

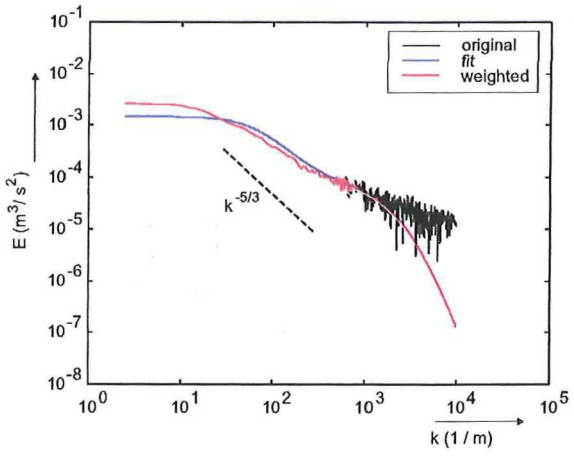

(a) y/R = 0.01, $k^* = 900$

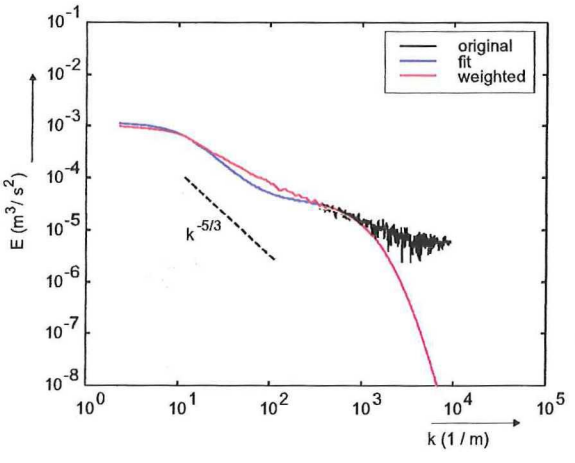

(b) y/R = 0.1, $k^* = 500$

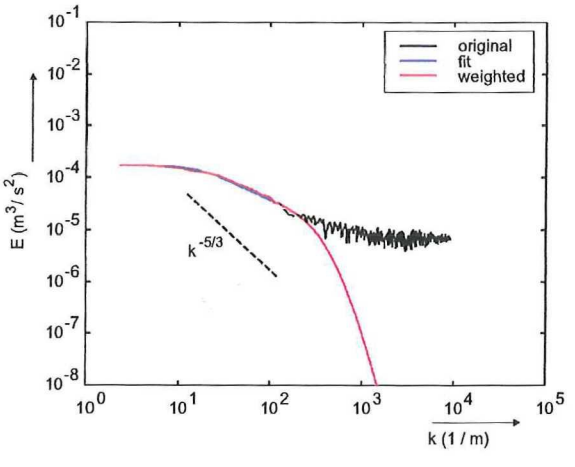

(c) y/R = 1.0, $k^* = 150$

Figure F.3: Power spectra in the throat, $Re = 298 \cdot 10^3$

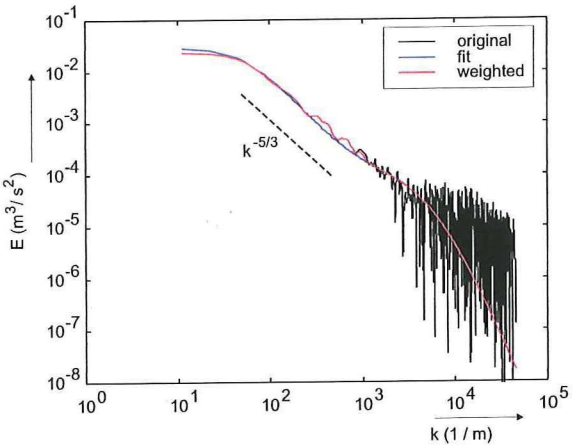

(a) y/R = 0.01, $k^* = 1200$

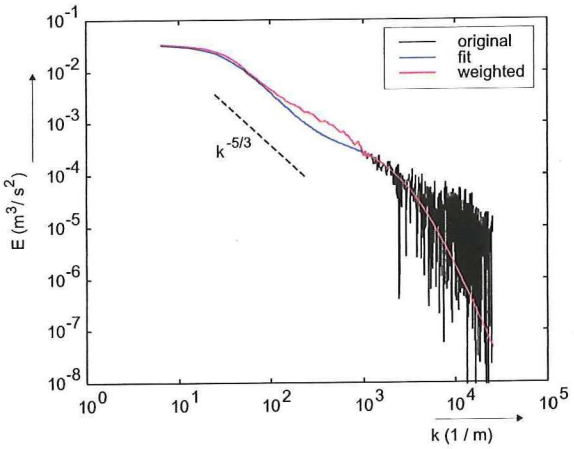

(b) y/R = 0.1, $k^* = 1500$

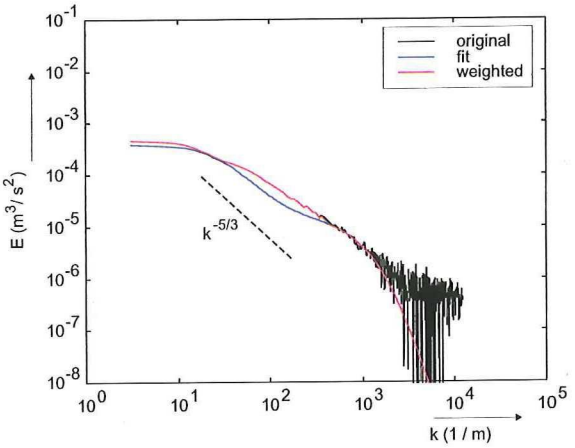

(c) y/R = 1.0, $k^* = 500$

Figure F.4: Power spectra in the diffuser, $Re = 246 \cdot 10^3$

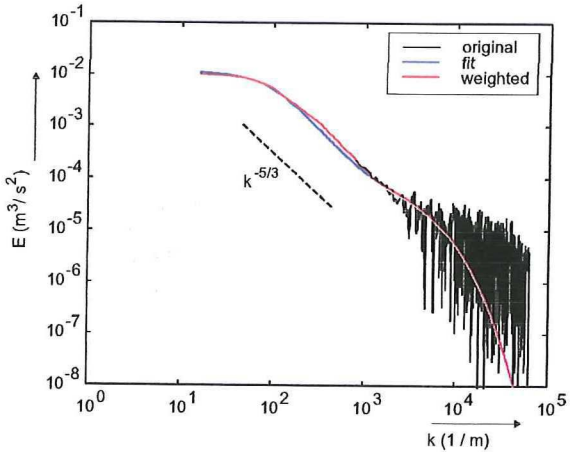

(a) y/R = 0.01, $k^* = 1180$

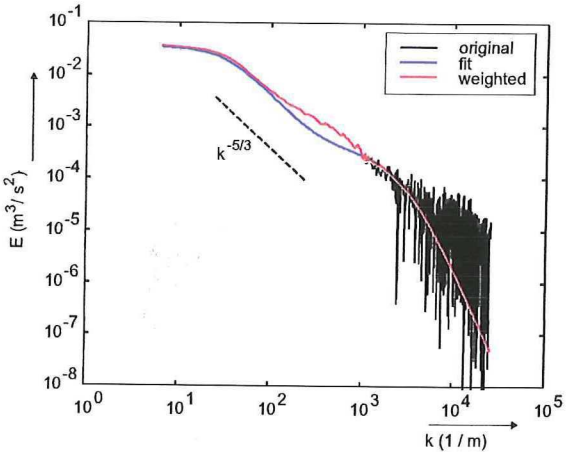

(b) y/R = 0.1, $k^* = 1300$

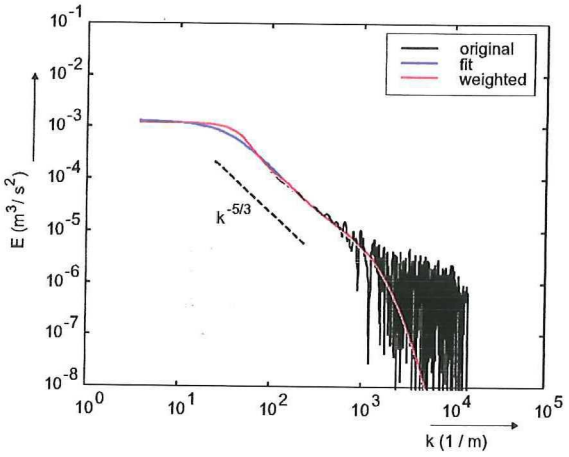

(c) y/R = 1.0, $k^* = 150$

Figure F.5: Power spectra 0D downstream, $Re = 196 \cdot 10^3$

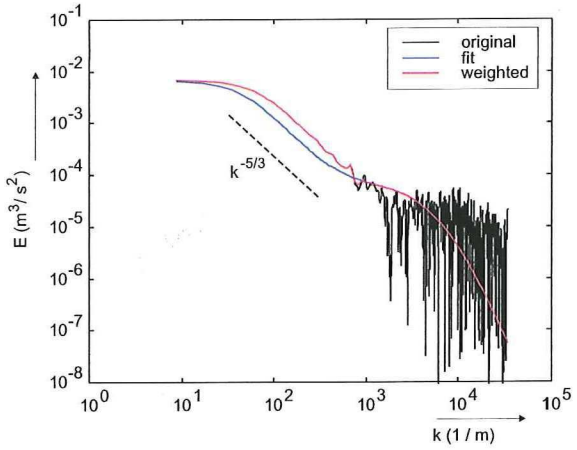

(a) y/R = 0.01, $k^* = 1010$

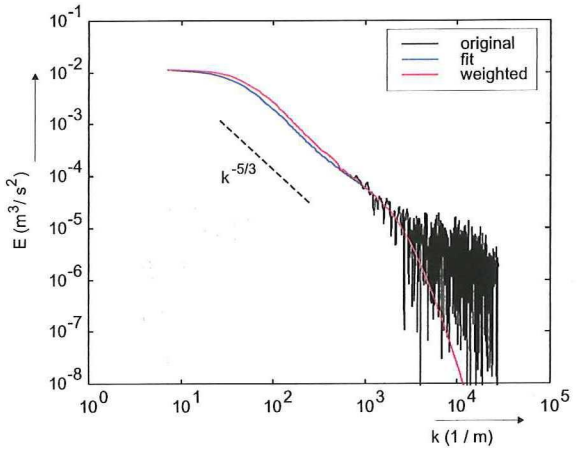

(b) y/R = 0.1, $k^* = 1000$

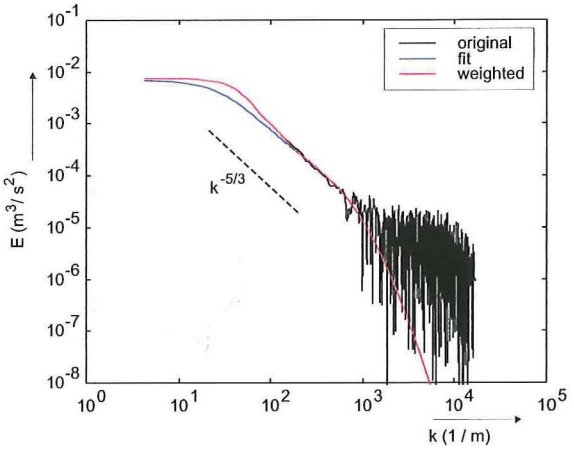

(c) y/R = 1.0, $k^* = 200$

Figure F.6: Power spectra 2D downstream, $Re = 196 \cdot 10^3$

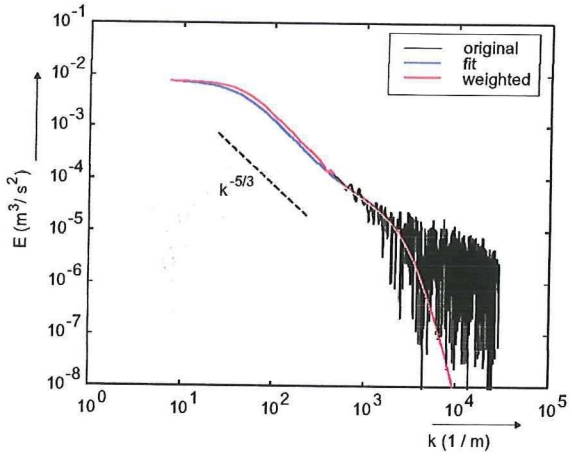

(a) y/R = 0.01, $k^* = 600$

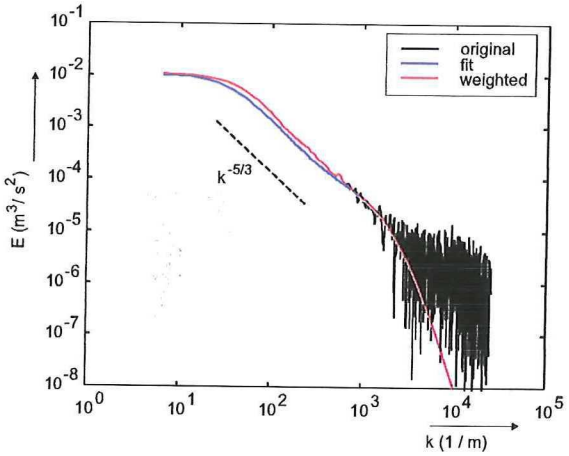

(b) y/R = 0.1, $k^* = 900$

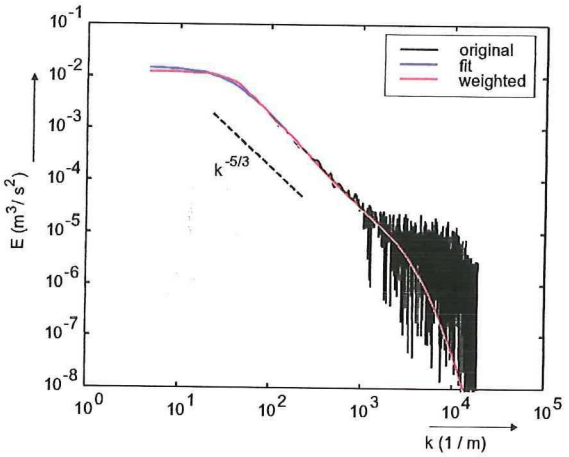

(c) y/R = 1.0, $k^* = 170$

Figure F.7: Power spectra 3D downstream, $Re = 196 \cdot 10^3$

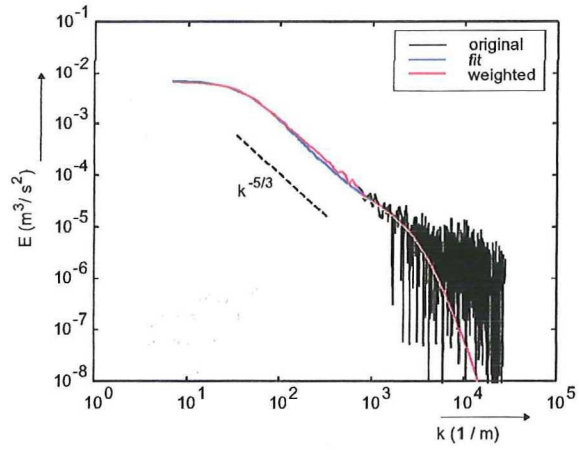

(a) y/R = 0.01, $k^* = 1000$

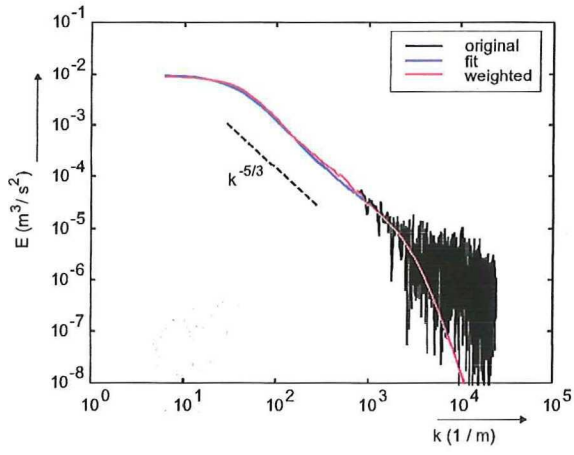

(b) y/R = 0.1, $k^* = 1020$

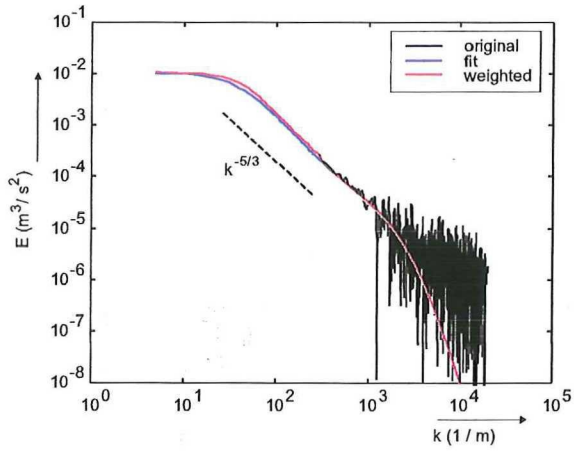

(c) y/R = 1.0, $k^* = 400$

Figure F.8: Power spectra 4D downstream, $Re = 196 \cdot 10^3$

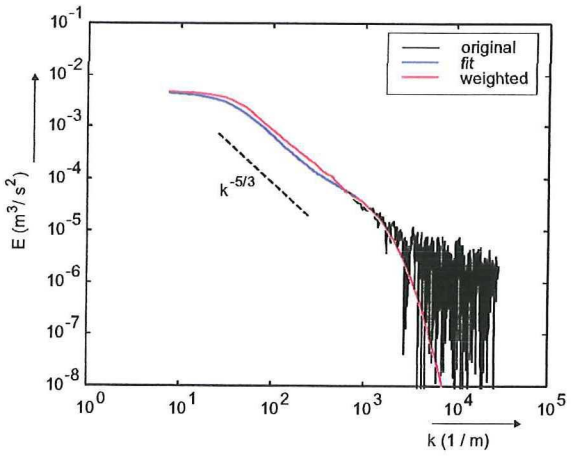

(a) y/R = 0.01, $k^* = 900$

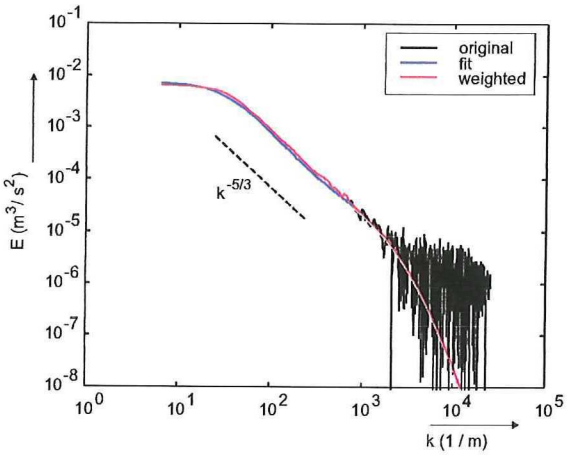

(b) y/R = 0.1, $k^* = 950$

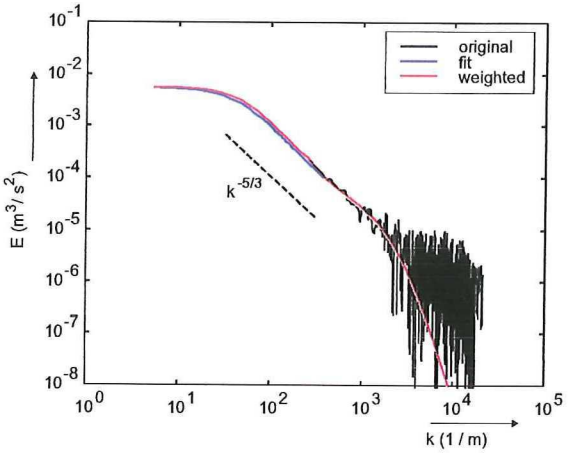

(c) y/R = 1.0, $k^* = 375$

Figure F.9: Power spectra 5D downstream, $Re = 196 \cdot 10^3$